Circuits and Systems for Low-Power Miniaturized Wireless Sensors

Manohar Nagaraju

A dissertation submitted in partial fulfillment of the
requirements for the degree of

Doctor of Philosophy

University of Washington

2015

Reading Committee:

Brian P. Otis, Chair

Richard C. Ruby

Jacques C. Rudell

Program Authorized to Offer Degree:
Department of Electrical Engineering

University of Washington

Abstract

Circuits and Systems for Low-Power Miniaturized Wireless Sensors

Manohar Nagaraju

Chair of the Supervisory Committee:
Associate Professor Brian P. Otis
Department of Electrical Engineering

The field of electronic sensors has witnessed a tremendous growth over the last decade particularly with the proliferation of mobile devices. New applications in Internet of Things (IoT), wearable technology, are further expected to fuel the demand for sensors from current numbers in the range of billions to trillions in the next decade. The main challenges for a trillion sensors are continued miniaturization, low-cost and large-scale manufacturing process, and low power consumption. Traditional integration and circuit design techniques in sensor systems are not suitable for applications in smart dust, IoT etc.

The first part of this thesis demonstrates an example sensor system for biosignal recording and illustrates the tradeoffs in the design of low-power miniaturized sensors. The different components of the sensor system are integrated at the board level. The second part of the thesis demonstrates fully integrated sensors that enable extreme miniaturization of a sensing system with the sensor element, processing circuitry, a frequency reference for communication and the communication circuitry in a single hermetically sealed die. Design techniques to reduce the power consumption of the sensor interface circuitry at the architecture and circuit level are demonstrated. The principles are used to design sensors for two of the most common physical variables, mass and pressure. A low-power wireless mass and pressure sensor suitable for a wide variety of biological/chemical sensing applications and Tire Pressure Monitoring Systems (TPMS) respectively are demonstrated. Further, the idea of using high-Q resonators for a Voltage Controlled Oscillator (VCO) is proposed

and a low-noise, wide bandwidth FBAR-based VCO is presented.

TABLE OF CONTENTS

Page

LIST OF FIGURES

LIST OF TABLES

GLOSSARY

IOT: Internet of Things.

MEMS: Micro Electro-Mechanical Systems.

FBAR: Thin-Film Bulk Acoustic Resonator.

VCO: Voltage Controlled Oscillator

ADC: Analog-to-Digital Converter

SNR: Signal-to-Noise Ratio.

DRIE: Deep Reactive-Ion Etching.

SEM: Scanning Electron Microscope.

TPMS: Tire Pressure Monitoring System.

CRF: Coupled FBAR Filter

NHTSA: National Highway Traffic Safety Administration

MBVD: modified Butterworth Van-Dyke model

ZDR: Zero Drift Resonator

ACKNOWLEDGMENTS

It has been a great experience studying in the Electrical Engineering department at the University of Washington, Seattle. The environment and the opportunities presented here have made me a better person over the years and I thank the Electrical Engineering department and the University of Washington for this. I would also like to thank everyone who has interacted with me over the years and making my graduate school days memorable.

First, I would like to acknowledge my adviser Prof. Brian Otis. He has taught me so many things from circuit design, to approaching a problem, finding the best solution and the attitude to stick it through. He literally held my hand in testing some of the first circuits in the initial years and having his expertise was really helpful. Brian's vision for impactful and relevant research direction helped shape this thesis. There were also periods during my PhD when I was totally clueless about the direction I was heading and doubting myself. We had a long chat and I still remember his encouragement, particularly the words "You can do it". I would like to thank him for believing in me more than myself during the rough periods of my graduate study.

His belief in aiming for the best has been inspirational. I remember after my first two ISSCC submissions were rejected, I did not think I should submit again at ISSCC. However, he always believed in our work. He also been an adviser on non-research related matters as a friend. He has left an indelible mark on me over the years and his ideals will continue to guide and inspire me for a long time.

I would also to thank Dr. Richard Ruby at Avago Technologies for providing valuable guidance, time, resources and the opportunity to collaborate with his team. His zeal to innovate and solve problems are unparalleled. I have learned a lot about the device side interacting with him over the years.

Many thanks to Prof. Chris Rudell for his guidance and advice during the past few

years. I would also like to thank Prof. David Allstot for his suggestions during the initial years when I was still finding my feet in the program. It was always great to talk to him and his advice was really helpful.

I am also thankful to my labmates at WSL. Thanks to Tim and Jingren for leading the in-vivo studies and patiently testing numerous chips in the sensor project respectively. Helen has been inspirational and have I learned a lot interacting with her. Discussions with Kannan have always been thought provoking and provided new ideas. Many thanks to Jagdish Pandey for guiding me in the initial years in WSL. Also, I would like to thank Julie Hu, Jason Silver, Jianlei Shi, Ethan, Yu-Te Liao, Apurva Mishra, Anthony, Luis Perez and Spencer for their help and suggestions in my research. I will always remember the days when we worked together on research projects, chip tape-outs and testing. I am also thankful to Karthik Natarajan from SOC lab and Venumadhav from the FAST lab for their suggestions.

I am also indebted to the WSD team at Avago. John Larson has been an inspirational figure with his enthusiasm and passion. I was privileged to interact with him. I want to thank Steve Gilbert for advice and help in the CRF project. Suresh Sridaran for guidance in the sensor project. Reed Parker and Lori Callaghan for helpful suggestions always. Dorie for wirebonding numerous chips and making complex and almost impossible assemblies possible.

Many thanks to the University of Washington Nanofab, particularly Andy Lingley for the processing support and making the sensor project successful.

I would also like to acknowledge Cameron Charles and Ken Stevens from the University of Utah for their advice over the years.

On the personal side, big thanks to my parents for supporting me over the years. They have been supportive of me and nurtured my ambitions right from my childhood. Thanks to Manju and Sunitha for helping me keep a stress-free mind. I would also like to thank my wife, Vaishali for providing me the strength and support over the years and also for patiently listening to all my problems.

Special thanks to all my friends; Vidyasagar, Rajendra, Santosh, Vikas, Ankit, Rahul, DJ, Dilip, Tejas, Shilpa, Bijetri, Vivek, Soumya, Raghava, Avanish, Shreyas Subramanya and Shayan

Last but not the least, I would like to thank my grandfather, Ram Rao whose principles and philosophy will always guide me.

DEDICATION

to my parents, R. Nagaraju and P. R. Sumithra

Chapter 1

INTRODUCTION TO SENSOR SYSTEMS

The quest to make human life safer and comfortable by studying the environment around us has led to rapid advances in technology. Electronic sensors have empowered us in this quest to study the environment. A sensor is a device that detects changes in a physical variable, such as pressure, temperature and provides a detectable electrical/optical signal. For example, a thermocouple converts a temperature difference at two points to an output voltage.

The advancement in the sensing and processing technology has enabled new areas of study in medical research, automotive engineering, agriculture, consumer applications to name a few. For example, modern medical care routinely involves monitoring vital physiological signals, like the electrical activity along the scalp (EEG) to diagnose brain disorders. Automobiles of today are equipped with hundreds of sensors to enhance the safety and comfort of our journey. Cellphones today have numerous sensors embedded inside to enable ease of use and improve the quality of life. In the past decade, both industrial and academic interest in the development of fully autonomous sensor nodes has seen rapid growth. The number of sensors, in just the mobile market consisting of cell phones, tablets, cameras etc, increased from 10 million units in 2007 to about 3.5 billion units in 2012. They mainly consist of four sensors: microphones, gyroscope, accelerometer and compass. Moving forward, sensors will be deployed in a diverse array of fields and point to a market of trillion sensors by 2022 [48].

The primary enabler for the popularity of sensors has been the miniaturization in the sensing technology possible due to the advancement in the field of electronics. Future emerging applications of sensors demand further miniaturization along with a near complete energy autonomy and low cost processing. In this work, we present innovation in processing technology to enable miniaturization, and reduce manufacturing cost of the sen-

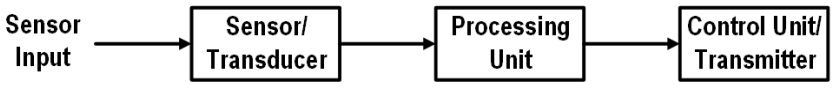

Figure 1.1: Sensor Actuator Interface

sor, architecture and circuit innovations to enable low energy consumption of the sensor interface readout circuitry.

1.1 Sensor Fundamentals

A sensor is a device that detects changes in a physical variable, such as pressure, temperature and provides a detectable electrical/optical signal. The detected electrical signal is then stored and processed in a sensor readout/interface circuitry to extract the useful information. This information could then be used to control an actuator or transmitted to an off-shelf control unit. Figure 1.1 shows a block diagram of a sensor actuator interface.

1.2 Requirement of Sensor Systems

We first outline the requirements of a sensor system in this section.

1.2.1 Measurement properties:

A sensor should satisfy certain measurement properties for its usefulness in everyday applications. Listed below are the typical specifications of a sensor system

- Resolution (R): Resolution of a sensor is defined as the smallest change in the input variable that can be detected by the sensor. A high resolution sensor is able to detect very small changes in the input variable. The resolution of a sensor is limited by the noise in the sensor and the interface circuitry. Noise is undesirable fluctuations in a device that affects the output signal not caused by the input variable. Sensor noise is typically caused by internal thermal and electrical vibrations and is a completely random process.

- Sensitivity (S): Sensitivity is defined as the ratio of the change in output variable per unit of the input variable. It is given by the slope of the calibration curve at a given value of the input.

- Accuracy (A): Accuracy characterizes the sensor measurement in an absolute sense. It is equal to the maximum difference that will exist between the actual value (measured by a primary standard) and the indicated value at the output of the sensor. Ideally, this value should be zero.

- Drift (D): Drift is the low-frequency change in a sensor with time. It is often associated with electronic aging of components or reference standards in the sensor. Drift generally decreases with the age of a sensor as the component parts mature. Ideally, this value should be zero.

- Hysteresis (H): A transducer should be capable of following the changes in the input parameter regardless of which direction the change is made; hysteresis is the measure of this property.

- Response Time (T): Response time is a simple estimate of the frequency response of a sensor assuming an exponential behavior. It characterizes the ability of a sensor to respond to fast changing inputs.

- Dynamic Range (Ra): The range of the sensor is the maximum and minimum values of applied parameter that can be measured. For example, a given pressure sensor may have a range of 0 psi to 100 psi.

1.2.2 Size/Form Factor

Miniaturized sensor systems enable new applications and allow us to deploy a large number of sensors in a small area. Emerging applications in healthcare, for example, DNA-sequencing demand extreme miniaturization and an array of sensors in a small footprint. Sensor systems typically contain a transducer, interface circuity, and a control or a transmit

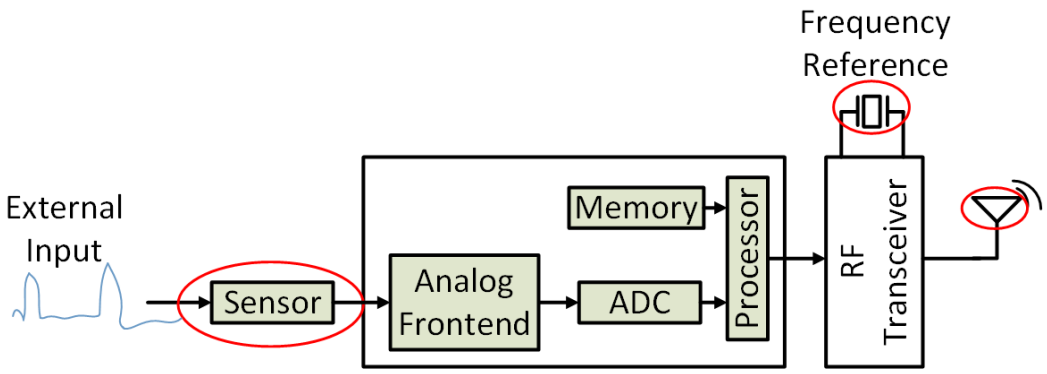

Figure 1.2: Architecture of a Typical Sensor System

unit. Figure 1.2 shows a typical modern sensor system. The sensor/transducer provides an electrical signal processed by an Integrated Circuit (IC) consisting of an Analog front-end to amplify the signal of interest, Analog-to-Digital Converter (ADC) to digitize the analog signal, and a processor to extract the information. This information is then transmitted wirelessly to an external control unit to provide the necessary actuation. Sensor systems also integrate a receiver to receive command signals in order to be able to deploy the sensor in remote environments.

Advancements in processing technology have reduced the size of the interface circuitry drastically. Current research has also focused on integrating the sensor interface circuitry and the wireless transceiver on a single die. However, the sensor, frequency reference and the antenna for wireless transmission are off-chip components which limit the miniaturization of sensors.

1.2.3 Operating Life

Sensing systems are typically deployed in remote environments without a constant energy source. Energy harvesting from solar, wind etc can provide a limited amount of energy considering the small footprint of a sensor system. Sensing systems demand a low power consumption to enable continuous operation for a long time with limited battery power. Advancements in energy harvesting and low power electronics will go hand-in-hand to solve

the problem of complete energy autonomy. This allows us to deploy the sensors in remote areas and also in battery constrained applications like cellphones.

1.2.4 Cost and Manufacturability

The growth of the sensor market is primarily determined by the cost or the selling price. According to the trillion sensor roadmap, the selling price of each sensor needs to be under \$0.13 [48]. The sensor system itself should have a low cost of manufacturability, thus enabling large scale adaption in the consumer market. Advancements in the Complementary Metal-Oxide Semiconductor (CMOS) processing technology has reduced the cost of the integrated circuits and hence the processing unit in a sensor system. However, a sensor system has other off-chip components (sensor, battery, frequency reference etc) which are integrated at the board level. Methods leveraging the capabilities of the existing fabs to integrate the different components greatly reduces the system cost. This requires close co-operation between the MEMS processing and the existing CMOS fabs.

1.2.5 Wireless Capability

The sensor system should also provide means of transmitting the sensed information to an external control unit or an actuator. A wireless transmission provides mobility and enables the sensor to be deployed in hard-to-reach areas. A wireless transmitter requires a stable frequency reference, such as quartz, to be incorporated in the sensor system. Suitable security protocols also need to be established between the sensor and the actuator to prevent false actuation.

1.3 Contributions of this work

The following chapters generally explore two main areas:

1. **Integration:** Techniques for achieving a monolithic integration of news MEMS technology with the CMOS circuitry are explored. This work demonstrates fully integrated sensor systems, with the sensor, interface circuitry, a frequency reference and a wireless

transmitter in a single die. The process flow uses standard micromachining process throughout, making it commercially viable in mass production.

2. **Low Power Consumption:** Techniques to reduce the power consumption of the interface circuitry of the sensor are proposed. Designs exploring high data rate transmitters required for the integration of multiple sensors while maintaining a low power consumption are demonstrated.

The rest of the thesis is organized as follows. Chapter 2 demonstrates an example sensor system useful for biosignal recording. The sensor system is suitable for EEG/ECG or neural signal recording for mainstream healthcare applications. The various factors influencing the overall form factor, ease of usability, power consumption and hence the operating life are analyzed. The limitations with respect to integrating the different components of the sensor system are outlined.

Chapter 3 presents the design of a fully integrated mass sensor suitable for a wide variety of chemical and biological sensing applications. Initially, we introduce the Thin Film Bulk Acoustic Wave Resonator (FBAR) and propose the use of an FBAR as the mass sensor. We also demonstrate a wafer-scale fabrication process to integrate the sensor, processing unit and a frequency reference in a single die.

In Chapter 4 we demonstrate the idea of a differential pressure sensor using a piezoelectric device like FBAR as the sensing element. We explore the processing methodology for the fabrication of a pressure sensor and demonstrate a fully integrated sub-mm^3 pressure sensor suitable for TPMS applications.

Chapter 5 presents the design of a low power digital interface IC suitable for FBAR-based sensors. The instantaneous power consumption of the sensor interface presented in earlier chapters is prohibitively high to be used with standard coin-cell batteries, considering that a Tire Pressure Monitoring System (TPMS) would include an additional accelerometer, memory and an on-chip controller. In this work, we propose to reduce the instantaneous power consumption by processing the sensor information in the digital domain.

Chapter 6 demonstrates a wide band VCO suitable for high data rate transmitters. Future sensor applications in 'smart dust', multichannel biosignal recording etc. require

the integration of numerous sensors (> 1000) in close proximity. This requires a high data rate transmitter while also maintaining a low power consumption. We propose a coupled-FBAR VCO which provides a high-Q (> 700) wideband resonator characteristic, enabling the design of high data rate transmitters.

Chapter 7 draws the conclusion of the research with a summary and a discussion of directions for future work.

Chapter 2

BIOSIGNAL SENSOR SYSTEM

In this chapter, a typical sensor system mirroring the architecture outlined in Figure 1.2 for biosignal recording is proposed. The tradeoffs in the design of sensor system are analyzed. Factors relating to miniaturization, ease of use, application scenarios, operating life are considered.

There is a tremendous emerging need for small, wireless, high-performance biosignal (EEG, ECG and neural) monitoring devices. There are existing devices that are currently deployed in relatively small numbers in animal research laboratories and serving as chronic implants. Researchers are also working on devices for clinical use and specialty athletic purposes. However, there are still barriers preventing widespread deployment of wireless devices in mainstream medical monitoring. Each application has specific challenges unique to its implementation as outlined in Chapter 1. The challenges can be addressed with a hardware approach on the device, but such a device becomes more application specific with these additions. The goal of this design is to propose a generic device that is useful in a wide swath of applications, dealing with many of these application specific problems with either device programmability or digital signal conditioning off-chip to demonstrate a typical wireless sensor node.

2.1 Specification of a Generic Biosignal Sensor

The specification of the sensor was guided to have a device that worked over ECG, EMG, and spike-based neural recording paradigms, while also meeting the requirements outlined in chapter 1. To define the needed technical requirements, two distinctly different applications were chosen that bookend the envisioned range of uses this device will be well suited for: human ECG and small animal (such as a mouse) extracellular single unit neuron recording.

2.1.1 Measurement properties:

Human ECG exhibits fairly large voltage amplitudes (mVs) and low frequency content (150Hz minimum). Single unit neuron recording voltage amplitudes can vary widely, from 10 s of μVs to mVs depending on electrode placement and low frequency potentials (LFP). Frequency content here is much higher (over 1kHz). Additionally, the signal chain in the system should have low input referred noise (a few μVrms) and sufficient dynamic range to accommodate the recording of different signal modalities (single unit recording, electrocardiography (ECG), electromyography (EMG)).

2.1.2 Size:

Device weight is not a realistic limiting factor for a human, the device should be small enough and have a long enough wireless range to allow the subject freedom of movement. Conversely, weight and size are key constraints for applications on small animals such as a mouse. The device must be small enough for the animal to comfortably carry without affecting its normal behavior.

2.1.3 Operating Life:

Both human ECG and small animal extracellular single unit recording would benefit from a long lifetime running from a single battery; while in the ECG case its reasonable to extend the lifetime with a larger battery the small animal case requires a low-power design to maximize lifetime from a small battery due to the size constraint. The main challenge lies in integrating the entire system in a small form factor of $< 1\text{cm}^3$, with a weight of <1g and low-power consumption (<10mW) making them suitable for mass deployment.

2.1.4 Wireless Link:

The device needs to have a reliable, low-power communication interface to transmit the digitized biosignal to an external receiver. This necessitates the integration of a low-power transmitter that is capable of communicating reliably within an existing wireless infrastructure. The requirements of a wireless transmitter for a biosignal monitoring device include

low power consumption, stable frequency generation, fast start-up time and compatibility with relevant frequency bands. The telemetry link could be established using an inductive link [19] or through RF communication. The range of inductive links is limited. Ultra-wideband (UWB) is an attractive option, particularly for massively parallel multichannel systems where the data rate requirements are high [5]. However, this requires complex synchronization [15] and is susceptible to jamming due to the wide-open receiver RF front-end. Low power open-loop transmitters [11] experience drift as they are not locked to any reference signal using a crystal and hence their use in mainstream healthcare devices that require manufacturability and high yield/reliability is difficult. Therefore, a narrowband transmitter with a stable frequency generation scheme and low power consumption is a prudent choice for a wireless biosignal monitoring device.

2.1.5 Device Programmability:

Depending on the recording site location and condition the biosignal amplitude can vary widely, thus the gain and bandwidth of the amplifier front-end should be programmable on-the-fly to compensate. The monitoring device should also suppress motion artifacts to achieve long term portable biosignal monitoring.

2.2 Biosignal Sensor System Description

The overall architecture of a four channel biosignal monitor is shown in Figure 2.1. The analog front-end comprises of four low noise, fully differential amplifiers designed to interface directly with electrodes connected to tissue, followed by a variable gain amplifier to accommodate different signal modalities. One amplified channel is selected and digitized using an on-chip 8-bit successive approximation register (SAR) ADC. The digitized data is buffered, appended with a programmable header, and tagged with cyclical redundancy check (CRC) information to detect communication errors. Finally, the digital bits are transmitted using a sub-mW frequency-multiplying transmitter. A programmable system clock is derived from the radios 48 MHz crystal reference. To enable on-the-fly programming of the chip, an infrared (IR) phototransistor interface is integrated into the system. The IR interface, tuned to 935nm, allows wireless programming of the gain/bandwidth settings of

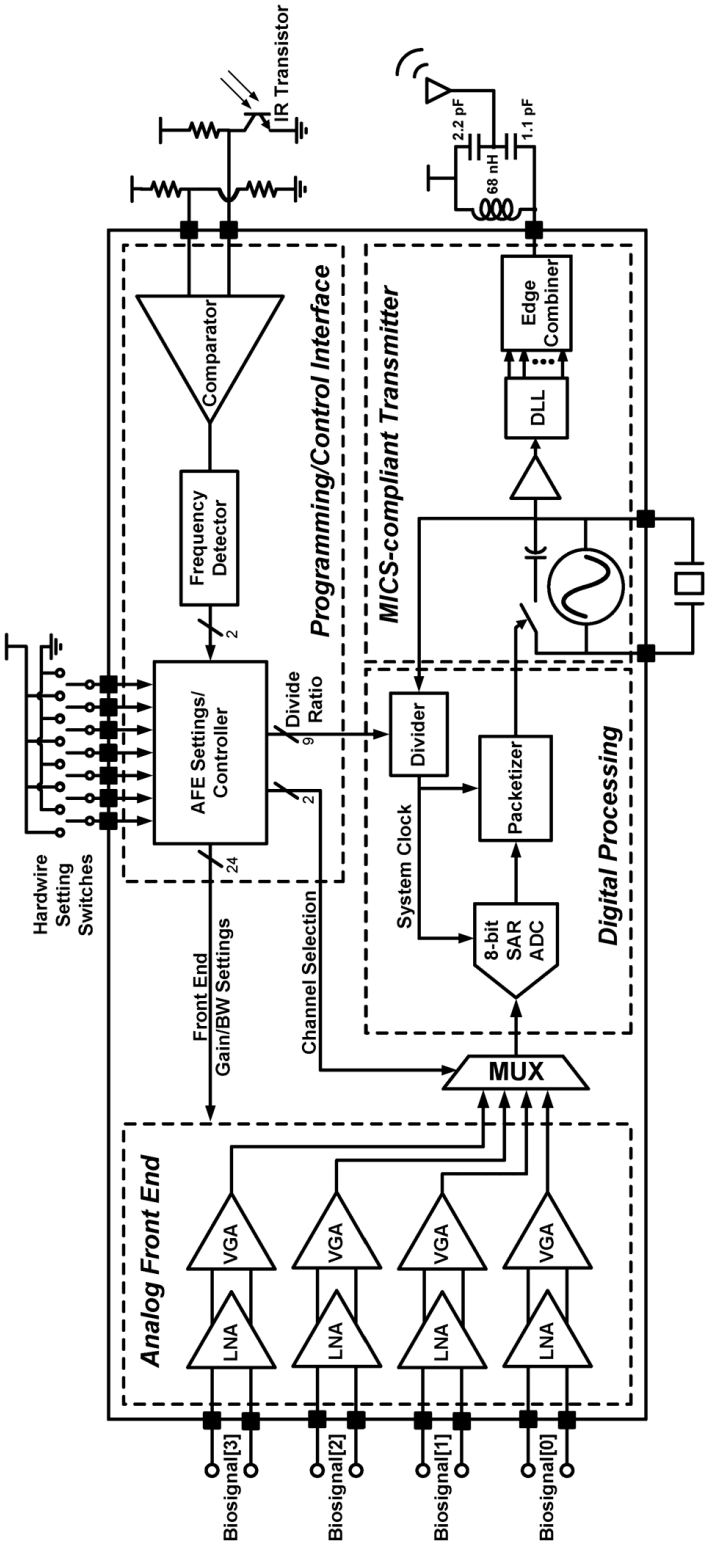

Figure 2.1: Block diagram of the wireless biosignal interface IC

each variable gain amplifier (VGA) independently and selects the active channel for transmission. All of these settings changes can be made on-the-fly using an infrared programmer to fine-tune the device for optimal recording during use.

2.2.1 Analog Front End

The analog front end (Figure 2.2) consists of four low-noise amplifiers whose inputs are AC coupled using on-chip 20 pF capacitors. High-resistance MOS-bipolar pseudo resistors enable a sub-Hz high pass cut-off frequency [10]. A complementary input stage in which both the n- and pFETs of the input stage contribute to the effective transconductance [11] reduces the input-referred noise voltage by a factor of two for the same bias current [12]. A fully differential closed-loop architecture provides sufficient linearity and supply rejection. Thick oxide MOS transistors are used at the input to minimize the 1/f noise and reduce gate leakage. The VGA consists of a complementary rail-to-rail folded-cascode core with programmable capacitive feedback. Six-level variable gain is set by selecting the feedback capacitors while the seven variable high pass corners are set by programming the feedback transconductor bias current. Each of the four channels is individually configurable for different gain and bandwidth settings. This is useful in single channel deployments to select the best channel and then optimizing the AFE for the recording site characteristics. Table 2.1 illustrates the available gains and their high pass cut-off frequency range covered by the seven filter settings. Four complete analog front ends were included to allow fast switching between channels, not possible by muxing four inputs to a single AFE due to the long settling time of the amplifiers compared to the sampling rate of the device.

2.2.2 ADC and Packetizer

An analog mux selects the amplified signal from one of the four input channels, which is digitized using a low power 8-bit SAR ADC, designed to operate at sample rates from 10 to 100 kS/s. The SAR topology was chosen for the ADC to minimize power consumption [35]. Since the AFE settings are wirelessly programmable during operation the user can adjust the gain/bandwidth to provide a close to full swing signal to the ADC, allowing an

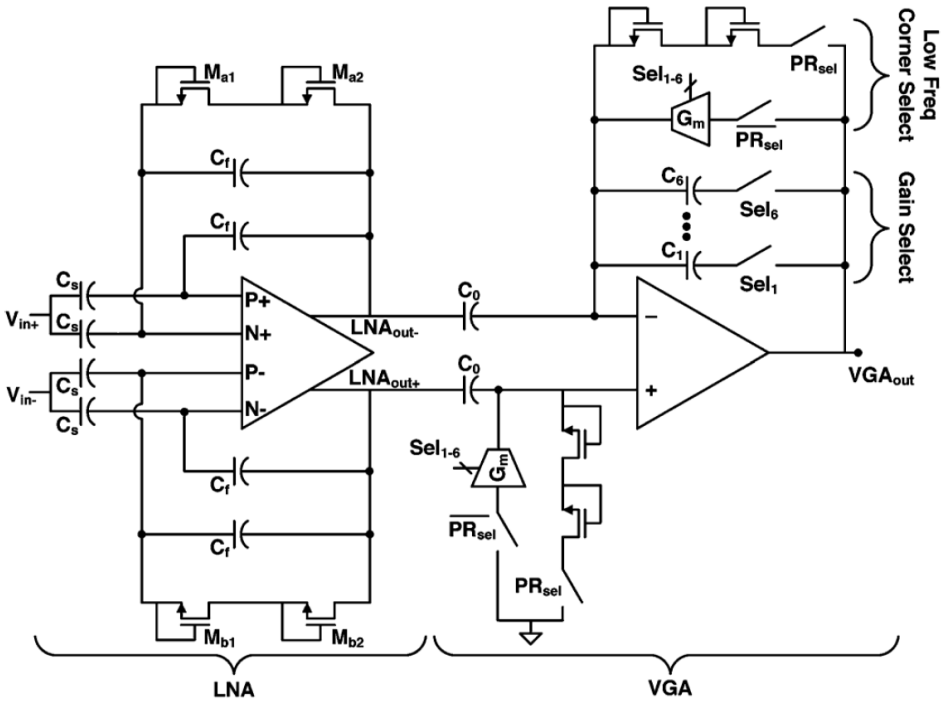

Figure 2.2: Architecture of the fully differential analog front end

8-bit ADC to provide suitable dynamic range for various recording scenarios. The digital ADC output is read serially from the comparator output. A synchronization signal, which is used internally to purge the DAC capacitor array and SAR logic after each conversion, also synchronizes the serial output. A divider provides the baseband clock for the system from the 48 MHz clock generated in the local oscillator of the transmitter. The divide ratio is programmable to enable different sampling rates depending on the application. A packet generator block (Figure 2.3) samples the output of this ADC and prepares the data for transmission. The serial output data from the ADC is buffered in a first-in, first-out (FIFO) memory structure. Data is pulled out of the FIFO by the packetizer block, which inserts this data into a standard packet structure and delivers this packet to the transmitter. The packet header consists of 32 bits of alternating $1-0$ s, then 32 bits of a constant sync code to identify the beginning of a packet, followed by 16 bits of system state data (current active channel number, gain and bandwidth setting), 256 bits of sample data and finally a

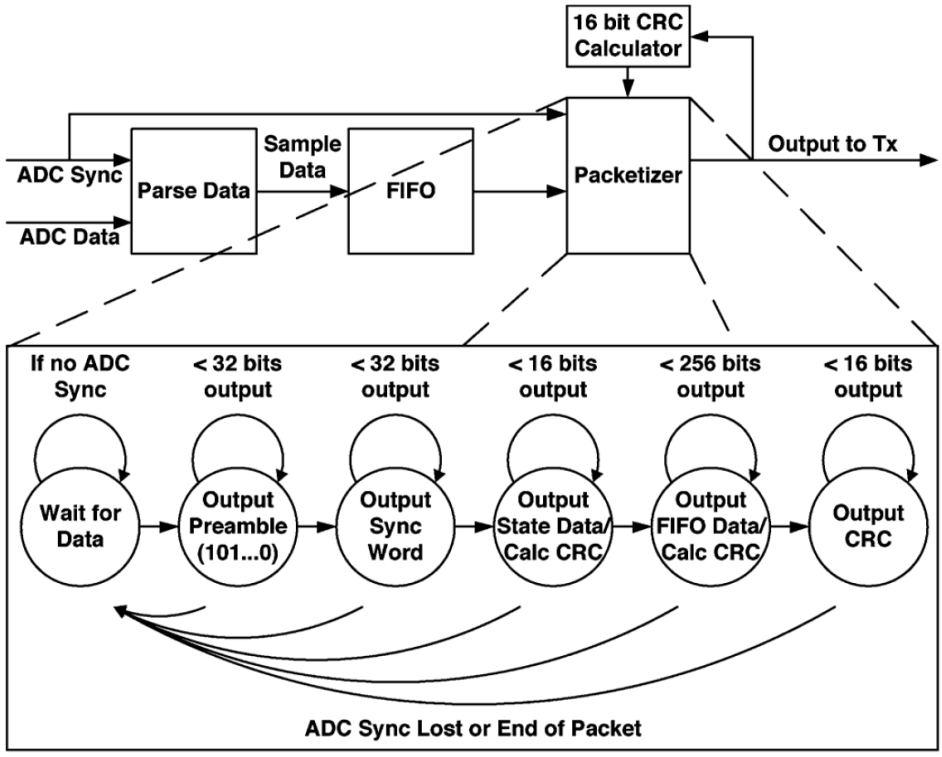

Figure 2.3: Block diagram of packet synthesizer with state diagram of the packetizer blocks for the biosignal interface IC

16 bit CRC. This packet structure was designed to be compatible with standard commercial ISM band receivers. The state data and sample data is run through a 16 bit CRC generator concurrently as the packetizer is outputting these bits. This synthesized digital logic block uses 2848 gates and takes approximately 0.018mm^2 of area.

2.2.3 MICS/ISM-Compliant Transmitter

The RF transmitter is typically the most power hungry block in wireless bio-interface systems [42]. We address this by employing a low-power synthesizer architecture that operates entirely at the crystal reference of 48 MHz and drives a 9 frequency multiplying power amplifier, eliminating the need for a PLL/DLL at the carrier frequency [35]. The baseband FSK data directly modulates the reference oscillator using capacitor pulling, allowing a 22

kHz frequency deviation. The reference clock drives a 9-stage DLL, thus the frequency deviation at the carrier frequency of 432 MHz is 198 kHz. This technique can be generalized to other multiplication factors, determined by the number of stages in the DLL and switching legs in the edge-combiner. Matching between the delay stages is ensured by balancing the delay-stage loads, symmetric layout and dual-edge locking to minimize reference spurs. The edge-combiner behaves like a high-efficiency, non-linear power amplifier, and produces pulses of current based on overlap of separate delay cells in the DLL. This current is absorbed by a tapped capacitor LC matching network, which transforms the TX source impedance to match a 50Ω antenna and attenuates out-of-band spurs. A return loss of less than 10 dB is achieved over the required bandwidth.

2.2.4 Programming/Control Interface

A biosignal monitor often requires on-the-fly changes in gain and bandwidth to accommodate different recording site conditions and provide the ability to switch channels to target specific electrodes. A continuously running RF receiver would dissipate a significant amount of power, we instead propose a low power wireless infrared interface using an off-chip IR phototransistor sensitive to 935 nm wavelength light. The incident IR signal is detected, amplified and limited rail-to-rail using an integrated comparator. A synthesized frequency detector block then measures the modulated frequency of the received IR signal. An IR remote control transmits the IR signal of a particular frequency for a fixed duration of 1 second. The digital frequency detector uses a divided version of the system clock and continuously counts the number of clock edges in a pre-programmed 333 ms time window to estimate the received signal frequency. If the determined frequencies of two successive time windows correspond to the same instruction then the signal is considered a valid instruction.

Once a valid instruction is detected the control block takes a corresponding action to change the state of the biosignal monitoring device as illustrated in Table 2.1. A frequency-based encoding scheme was used to avoid the need for complex clock and data recovery to save power. Thus, this technique is limited to a relatively small number of commands; to mitigate this fact the number of programming commands was greatly reduced by imple-

Table 2.1: Gain and high pass cut-off frequency options of the AFE

Gain (dB)	Filter Corner Range (Hz)
43	$< 0.1 - 230$
47	$< 0.1 - 506$
55	$< 0.1 - 1100$
64	$< 0.1 - 1370$
72	$< 0.1 - 1600$
80	$< 0.1 - 2000$

menting a control scheme where commands instruct the device to cycle between different settings as opposed to having many different commands that instruct the device to change to a particular setting. A frequency of 36 kHz increments the mux to select the next recording channel front end for digitization and transmission. Similarly, frequencies of 38 kHz and 40 kHz are used to cycle through the available gain and bandwidth settings. The sensor initially defaults into a reset state (with default gain and bandwidth settings hardwired through external switches) to suit the type of recording desired (neural, ECG, EMG, etc.). Current gain, filter and active channel settings are transmitted with each packet of sample data from the biosignal monitoring device so the user can confirm the device has been programmed as desired.

2.3 System Characterization and Measurement Results

This IC was implemented in a 0.13μm CMOS process, measuring $(2 * 2)$ mm^2 . Initial testing was performed on a large printed circuit board (PCB) to verify functionality. The die bonded to this test PCB can be seen in Figure 2.4. The system is intended to accommodate two different battery chemistries: one with a nominal voltage around 1.2 V and another around 1.45 V. With this in mind, the chip was tested with both supplies. Running on a 1.2 V supply, 1.07 mW of power is dissipated by the chip, of which -15.1 dBm (30.9μW)

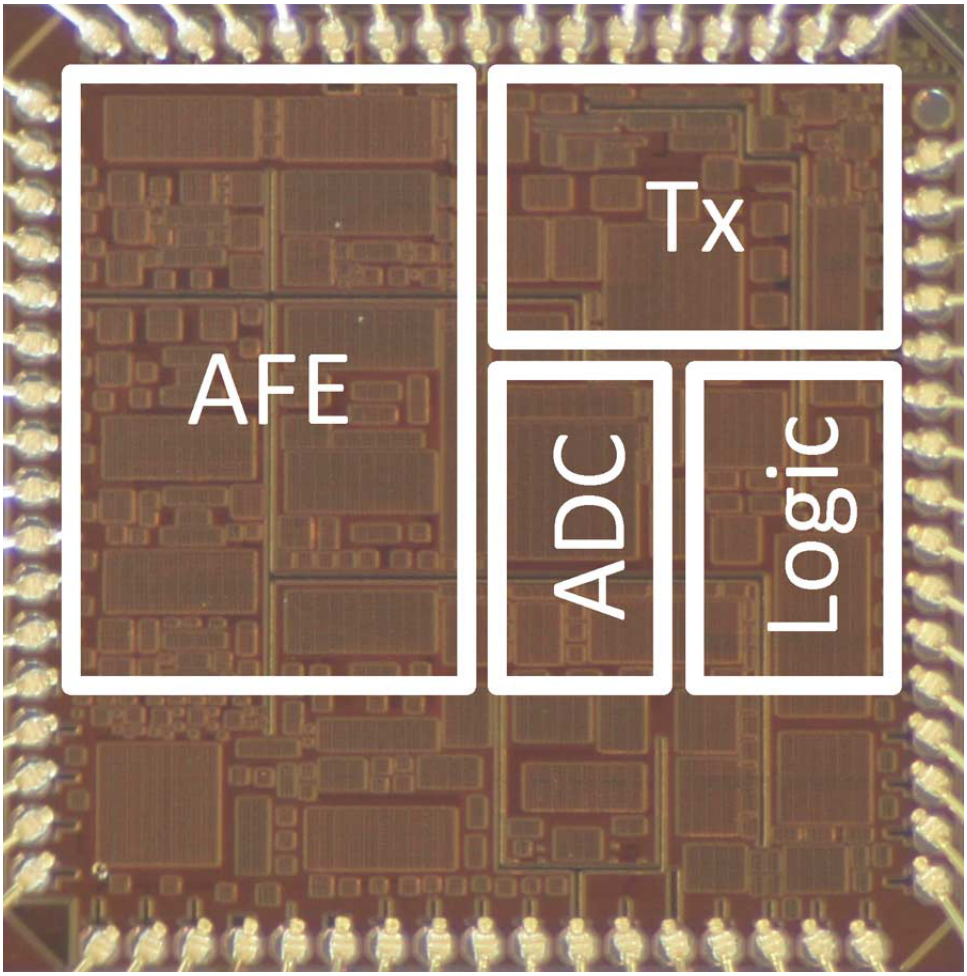

Figure 2.4: Die photo of $(2 * 2)$ mm^2 IC fabricated in $0.13\mu m$ CMOS noting the analog front end (AFE), ADC, transmitter and digital logic blocks.

is transmitted as RF power. With a 1.45 V supply, 1.73 mW of power is dissipated (RF output power of -11 dBm).

2.3.1 CMOS SOC

Rebooting into a relevant default state is key to this system's ease of use. The IC restarts into a default running state; seven binary inputs are used to set the chips default AFE gain, bandwidth, and ADC sample rate. These settings are selected through a switch matrix of small SMT pull-up/down resistors on board allowing the same IC to default into appropriate

AFE and sample rate states for different recording uses simply by changing these binary inputs. Of course, the chip parameters can be subsequently adjusted using the IR interface described in Section 2.2.4. All settings function as expected.

2.3.2 Deployable System

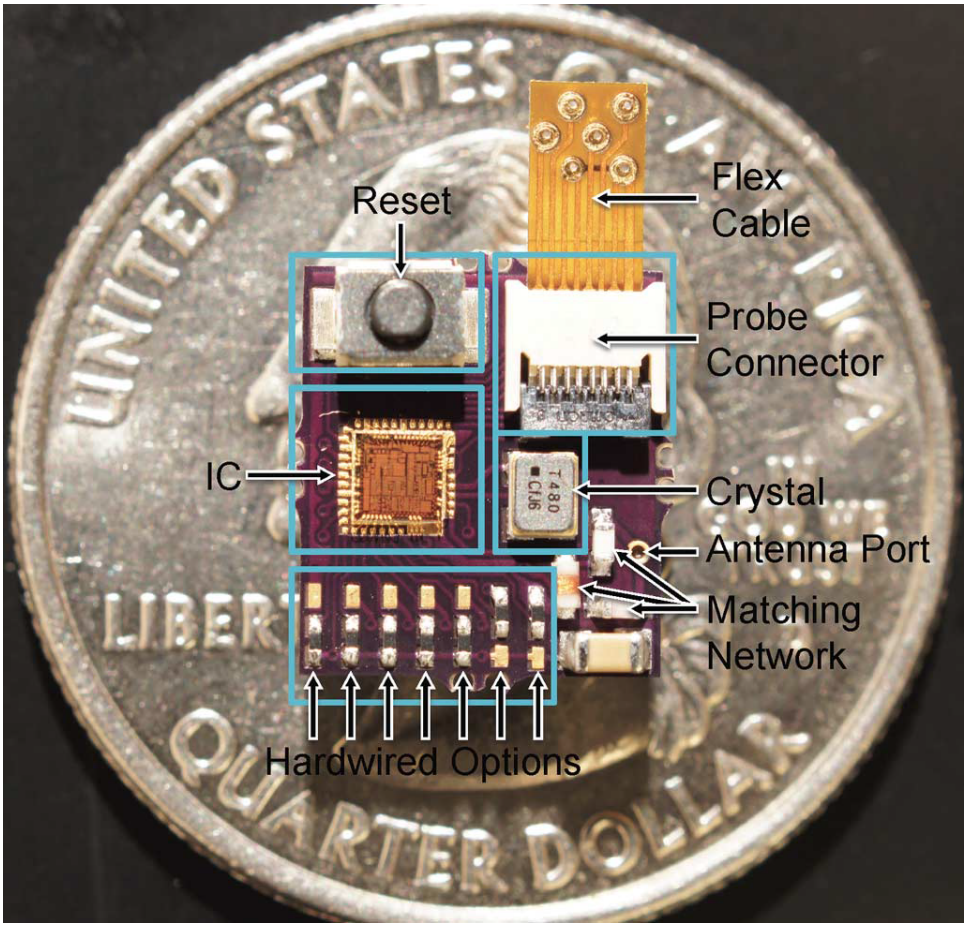

Figure 2.5: Deployable 0.8 cm^2 system and flexible PCB configured for four single ended analog inputs.

After benchtop verification, a small, lightweight PCB was designed to facilitate in vivo deployment of the system. The biosignal monitor was implemented on a four layer, 500μm thick FR4 PCB measuring $(8.6 * 9.7)$ mm^2, seen in Figure 2.5. The top side of the PCB

integrates the custom IC, seven 0201 pull-up/down resistor footprints to set different gain, bandwidth and clock speed options for the default state, a reset button, a 48 MHz quartz crystal, an RF matching network, a 17.4 cm long, No. 32 AWG insulated wire serving as a monopole antenna and an eight pin connector to mate external probes to the inputs of the device. Probes connect to this connector via a small flexible PCB that can be custom designed for the given experiments needs (i.e., single ended or fully differential, extra attenuation for large amplitude signals, integrated RC filter, etc.), allowing greater flexibility without requiring a re-spin of the biosignal monitor PCB. On the reverse side are either a 4.8 or 5.8 mm diameter battery holder and an infrared phototransistor. The total mass of the device is dependent on which battery is used; loaded with the silver-oxide 337 battery the total system weighs 522 mg including battery and antenna, with the zinc-air size 5 battery and a slightly larger battery holder the system weighs 612 mg.

The seven pull-up/down resistors could be removed to save area at the expense of fixing the default state of the device to only one option. Future versions could integrate non-volatile memory (NVM) to allow for different default states in the single design by programming the desired state into memory without requiring a reprogramming after every power-on. Likewise, future versions of this device could integrate a power-on reset block within the IC, eliminating the need for the external reset switch and reducing total deployable size and weight. The board area of the device is truly limited by the size of the battery and its holder; measuring for the zinc-air size 5 battery holder. Reducing the size any further would require the use of a different battery or an innovative mounting technique requiring a smaller footprint.

2.3.3 System Characterization

For system deployment, battery choice represents a critical tradeoff between size/weight and energy storage. The IC is capable of operating from a battery voltage anywhere between 0.9 V to 1.55 V. A variety of small coin cell type batteries are commercially available that could power this device, a selection of which can be seen in Table 2.2. Of these, two batteries were chosen that best meet our needs of high energy storage density and a small form factor/low

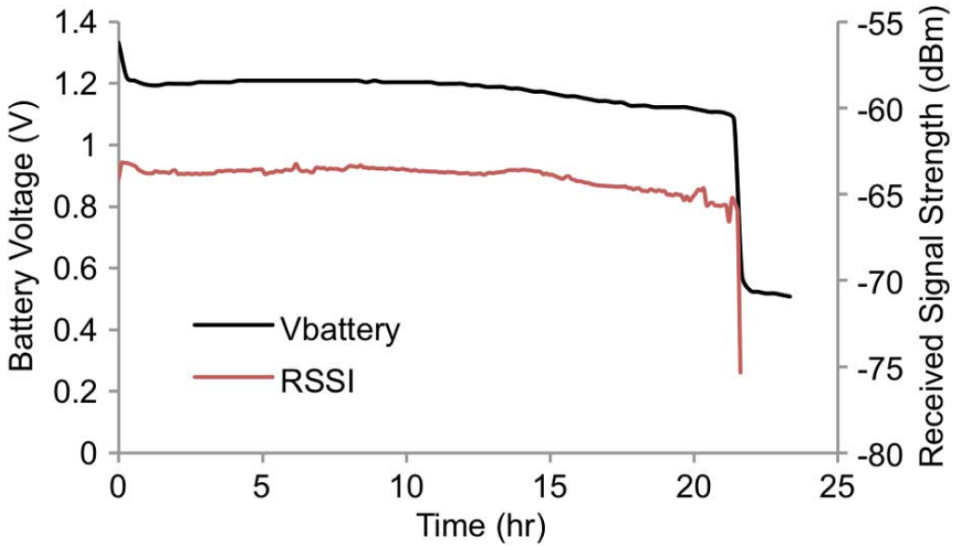

Figure 2.6: Power discharge curve of the biosignal monitoring system for the zinc-air size 5 battery.

Table 2.2: Small Coin Cell Battery Comparison

Battery Size	Chemistry	Voltage (V)	Diameter (mm)	Weight (gm)	Capacity (mAh)
337	Silver Oxide	1.55	4.8	0.13	8.3
10	Zinc Air	1.4	4.8	0.32	91
5	Zinc Air	1.4	5.8	0.17	33
CR1025	Lithium	3	5.8	0.7	30
191	Manganese dioxide	1.5	10	0.8	49
164	Mercuric oxide	1.4	11.6	0.36	24

weight, the Zinc-Air Size 5 and the Silver-Oxide Size 337. In both cases the wireless sensor draws more current than these batteries were intended to supply, which limits the amount of energy the system can actually extract from either battery and slightly reduces the nominal voltages from their rated values. Figure 2.6 shows the battery discharge curve for the Zinc-

Air Size 5 battery as well as the received signal strength (RSSI) measured at our receiver board. This battery will power the device for over 22 hours with a fairly consistent voltage of approximately 1.2 V. Over the entire 22 hours of transmission there were 0 packet errors until the final few minutes of operation when the battery was almost completely exhausted.

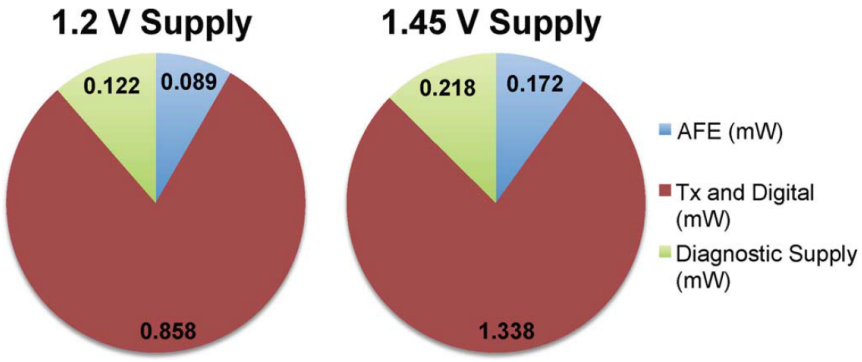

Figure 2.7: Power consumption breakdown of the biosignal monitor using 1.2 V and 1.45 V supplies.

The total power consumed by the sensor device is 1.07 mW using a 1.2 V supply (nominal voltage for Zinc-Air 5 battery) and 1.73mW using a 1.45 V battery (nominal voltage for Silver-Oxide 337 battery). A key digital buffer on the IC was mistakenly powered from a diagnostic supply intended only for debug purposes. It was thus necessary to power this auxiliary supply continuously. This easily fixable design error contributes approximately 12% to the total power consumed by the device. Figure 2.7 shows a breakdown of power consumption from the different blocks of the IC, including the auxiliary supply pin.

While it is possible to reduce the sampling rate of this device, the transmitter is in a fixed on-state, meaning a reduction in sampling rate will also reduce the baud rate of the transmitter to ensure a 100% duty cycle. Future versions could reduce the sampling rate while keeping the transmitter data rate at a maximum (200 kbps in this implementation), duty-cycling the transmitter as needed, which would greatly reduce power consumption for low sample rate applications. In this version, however, power consumption is fairly independent of sampling rate. Reducing the sampling rate in the current device mainly serves to reduce the total amount of data the receiver/PC would need to process.

Another important metric of any wireless system is the maximum acceptable range for data recovery. Commonly, this distance is defined as the point where the Bit Error Rate (BER, P_b) is 10^{-3}. Packet Error Rate (PER, P_p) can be defined in terms of BER since the PER is simply the sum of probabilities of every possible packet error permutation for a given BER. This is shown in equations 2.1 & 2.2, where n is the number of bits in a packet.

$$P_p(P_b) = \sum_{k=1}^{n} \left[\binom{n}{k} P_b^k (1 - P_b)^{n-k} \right] \tag{2.1}$$

$$P_p(P_b) = 1 - (1 - P_b)^n \tag{2.2}$$

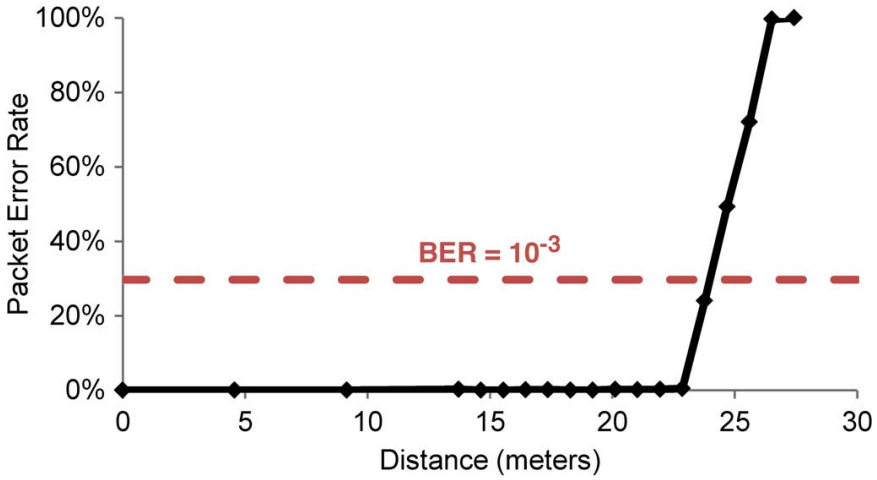

Figure 2.8: Packet error rate of the system versus distance between transmitter and receiver.

Our packets are 352 bits long; using equation 2.1 we see a PER of 29.7% represents a BER of 10^{-3}. Figure 2.8 shows the recorded PER of the system powered by the 337 Silver-Oxide battery at different distances from the receiver compared to the 29.7% PER point, giving a range of 24 m for this experiment. In a practical situation the acceptable amount of packet/data loss can be quite application dependent. Error detection is done solely by checking the CRC code so one cannot determine which bit(s) is/are in error in this system and thus must throw out the entire packet which makes the data loss in the received data 'blocky'. Figure 2.8 can be used to decide the acceptable operating range of the system for

a given application where practical range is decided by how many gaps in the recorded data is acceptable (likely over 20 m). The total input referred noise of the chip was measured through the entire system shorting the analog inputs to ground and setting the AFE at the maximum gain (78 dB) and widest bandwidth (9.2 kHz) setting (Table 2.1). The received data was then analyzed in Matlab to calculate input-referred noise. The wireless receiver recovered a signal with an RMS value of 1.73μV and no packet errors. This RMS noise value was computed at the receiver and includes all noise sources, including amplifier noise, VGA noise, ADC quantization noise, aliasing, supply noise, substrate coupling, etc.

2.4 In Vivo Testing

2.4.1 Human ECG Recording

A key attribute of this system is its long lifetime (22 hours at 100% duty cycle) and ease of use. Operation requires only inserting a battery and pressing the reset button. This allows it to be easily deployed in a home setting that lacks any support equipment or technical staff commonly available in a laboratory setting that a less refined device might require.

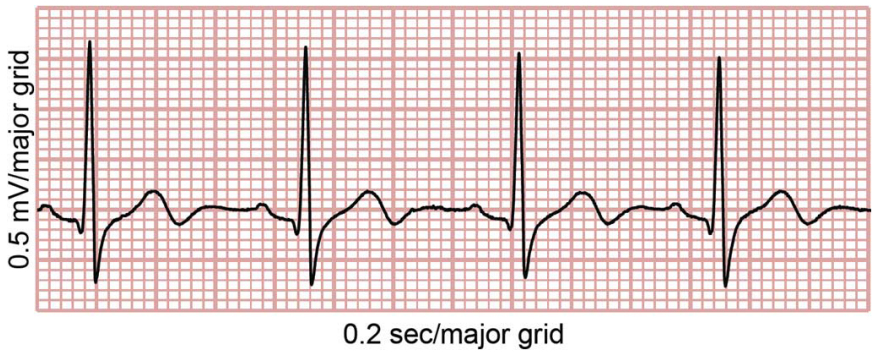

Figure 2.9: Human ECG recording over a short interval.

To demonstrate this functionality, the sensor was attached to a freely moving human subject at home over the course of a day, recording the electrical activity of the heart (ECG). Two Ag/AgCl conductive adhesive electrodes were connected in a single-ended configuration to the wireless sensor and attached to the subject's chest who was then left to go about his

day while staying within range of the receiver. Figure 2.9 presents a short length of this ECG data presented on a standard clinical ECG grid showing the expected healthy sinus rhythm. The signal was post-processed with a high order digital 1 Hz high pass filter to eliminate a wandering baseline, a changing dc level common in ECG monitoring likely due to patient movement.

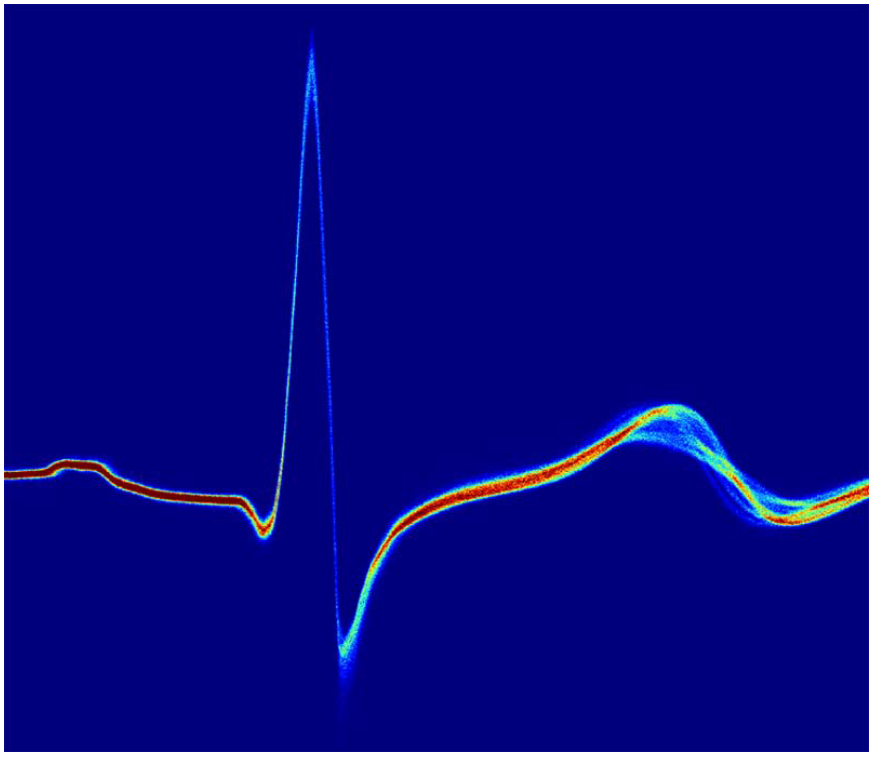

Figure 2.10: Human ECG recording over one hour overlaid.

An hour section of this recorded data was further processed, lining up each detected heartbeat with its central spike, known as the QRS complex. 4110 heartbeats were recorded in this hour, which can be seen overlaid in Figure 2.10. The figure is in a heat-map format, allowing easy visualization of artifacts and heartbeat waveform morphology. The ECG data recorded from a freely moving subject is quite consistent over the length of the experiment, showing only modest changes in the t-wave, the later part of the ECG waveform, which is due to changing heart rhythm as opposed to corrupted recordings.

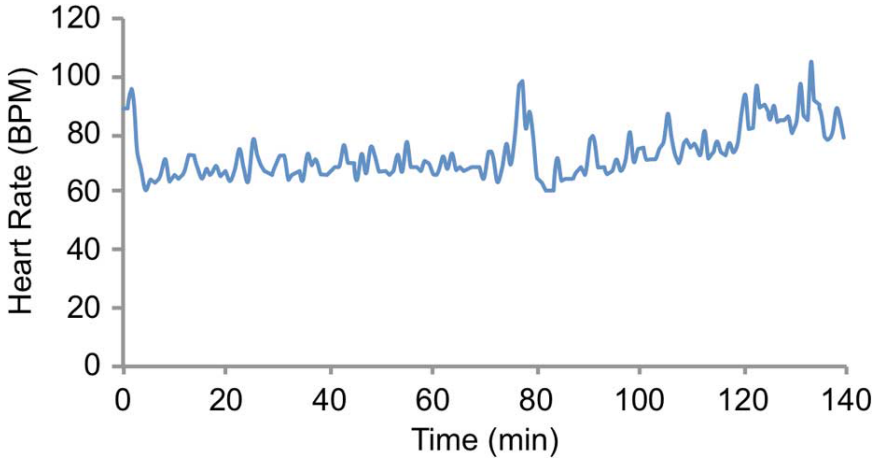

Figure 2.11: Recorded heart rate of human subject over 2 hours of normal activity.

Lastly, the recorded ECG data was used to determine the subjects heart rate over two hours of normal activity, as seen in Figure 2.11. There are minor variations in heart rate from beat to beat and over the two hour recording period. Here, 60 heartbeats were averaged together to calculate a mean heart rate for the subject and displayed in a more readable format.

2.4.2 Mouse Single Unit Recording

To demonstrate wireless neural recording from freely moving small animals, extracellular neural recordings from an awake, ambulatory mouse were performed. All surgical procedures were carried out in accordance with the Allen Institute for Brain Sciences Institutional Animal Care and Use Committee regulations using sterile techniques. Briefly, the cerebral cortex of anesthetized adult mice ($C57/Bl6, 25g$) was implanted with a microwire electrode array, consisting of (4) 50μm diameter polyimide-coated tungsten wires, [38], [39] coupled to the monitor via a custom flex board (Figure 2.5). Electrical reference was attached using uninsulated tungsten wire connected to a bone screw in the left hemisphere. Electrodes were implanted into vibrissal somatosensory cortex, which can provide immediate spiking information to researchers via manual whisker deflection [22]. The mouse was allowed to recover from anesthetization before recording response from whisker stimulation, examples

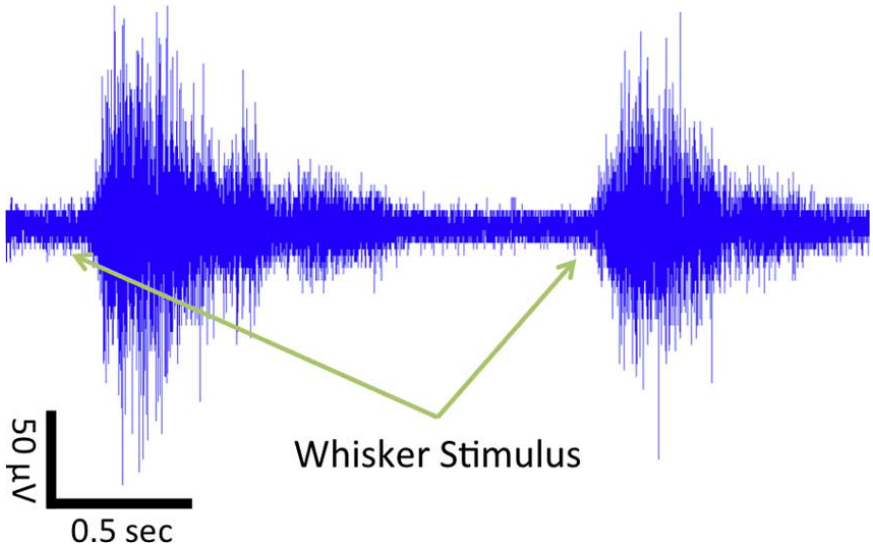

Figure 2.12: Spike recording stimulated in response to whisker deflection in mouse.

of which are shown in Figure 2.12. Using the IR programmer the one electrode of four implanted closest to the cells of interest was exercised post-surgery by cycling through all four channels and recording from channels with active spiking. Likewise, the IR programmer was used to set the gain of this channel to utilize as much of the dynamic range of the ADC as possible without clipping the signal. This method of fine-tuning the recording session would be much more difficult with a wired or near-field communications system since the test subject is freely moving and is not easily held still to keep wires (or inductive coupler, etc.) attached.

With antenna and battery, the entire neural recording system weighed only 612 mg, and continuously streamed neuronal spiking data from freely moving mice for up to 22 hours. Such a system is capable of replacing large and complicated recording equipment, placing the technique of extracellular electrophysiological recordings into a wider variety of laboratories with limited space or resources. Data transmission was recorded at distances over 10 m with a USB-PC receiver interface. Sensory-evoked neural spiking data recorded wirelessly were found to be qualitatively comparable to data recorded in a conventional wire-tethered recording system. At least two individual firing neurons could be identified

from recordings in the somatosensory cortex of a freely moving, awake mouse, when this spike data was processed with sorting software [34]. These two spike waveforms, shown in Figure 2.13, are displayed in a similar heat-map plotting technique to Figure 2.10. Since these two neurons were firing at approximately equivalent intervals their waveforms interact and corrupt a single spike waveform. When we overlay all the spikes in this heat-map format however, the spike shape is clearly visible.

2.5 Conclusion

This work demonstrates a low-power wireless biomedical sensor suitable for large-scale deployment in mainstream as well as experimental medical applications. The system requires minimal human calibration, in the form of a reset switch to start the recording, and operates continuously for 22 hours from a single zinc-air battery. A receiver comprised of off-the-shelf components records the transmitted digitized data from distances of over 20 m. A simple IR wireless programmer allows amplifier settings to be changed during recording if needed to further fine-tune the setup. The entire biomedical wireless sensor consumes 1.07 mW from a 1.2 V supply.

While the system is easy to use outside of a laboratory setting, the device size is limited by the sensor, in this case the microwire electrode array and the crystal for frequency reference as shown in Figure 2.5. The device size grows with the number of sensors and integration of numerous (> 1000) sensors becomes prohibitively difficult to interface with the processing IC in such a system. In the next few chapters, we explore techniques to integrate the sensor for physical variables (mass and pressure) and a frequency reference with the processing IC in a single die.

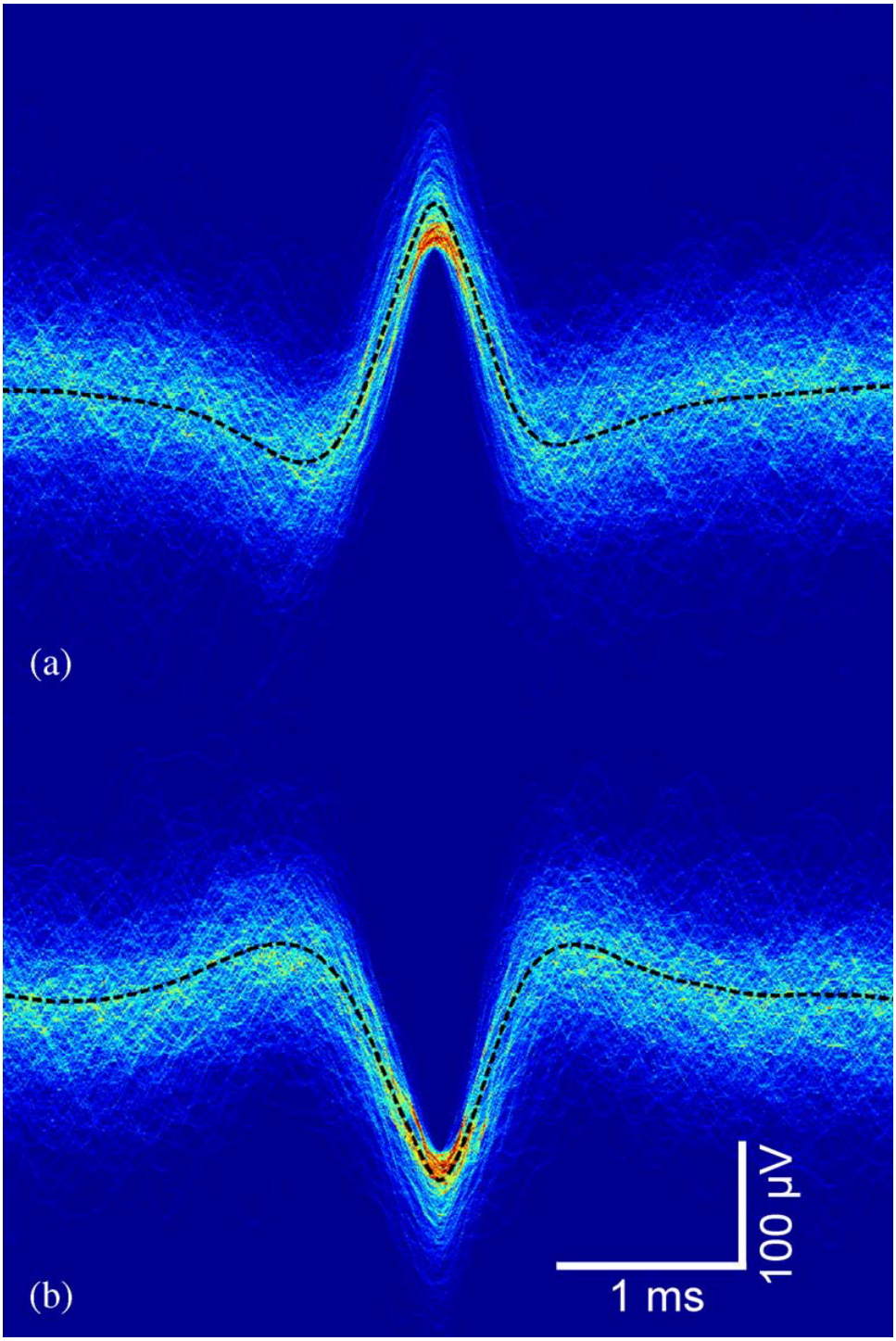

Figure 2.13: (a) and (b) Overlaid spike recordings of at least two firing neurons.

Chapter 3

A sub-mm^3 FULLY INTEGRATED MASS SENSOR

Mass sensitive sensors are increasingly finding applications in chemical and biological applications [4][57]. Quartz Crystal Microbalance (QCM) is the dominant technology currently in the market as a mass sensor. However, quartz crystals present a huge overhead to system miniaturization and cost reduction. Newer applications demand extreme miniaturization ($< 1\text{mm}^3$) and a tighter integration of the sensor and the interface circuitry. In this chapter, we will demonstrate a fully integrated sub-mm^3 mass sensor with an FBAR as the sensing element, processing IC, frequency reference for communication and a wireless interface in a single hermetically sealed die.

3.1 Introduction to FBAR

This section gives a brief overview of FBAR technology. A more detailed tutorial can be found at [41]. FBAR (Film Bulk Acoustic wave Resonator) is a miniaturized acoustic resonator with a metal-piezo-metal structure. It is fabricated in a planar silicon process with a layer of piezoelectric material (AIN) sandwiched between two electrodes (Figure 3.1). The piezoelectric layer converts electrical energy to acoustic energy and vice versa, through the piezoelectric effect. The typical size of an FBAR device is around $100 * 100\mu\text{m}^2$ about 100 times smaller than quartz crystals. Figure 3.2a shows a plot of frequency vs impedance of an FBAR resonator. There are two resonant frequencies: Series (f_s) and Parallel (f_p). Figure 3.2b shows the electrical equivalent model for an FBAR

FBAR's provide a very high quality factors of the order of a few thousand. The communication industry has used the high quality factor and the small footprint (< 1 mm^3) of FBAR's to its advantage, mainly in front-end filters and duplexers. The f-Q product - a resonator performance metric - is 10^{13} which is comparable to quartz crystals. This enables the design of ultra low power oscillators [26], frequency synthesizers [52] and transceivers [29].

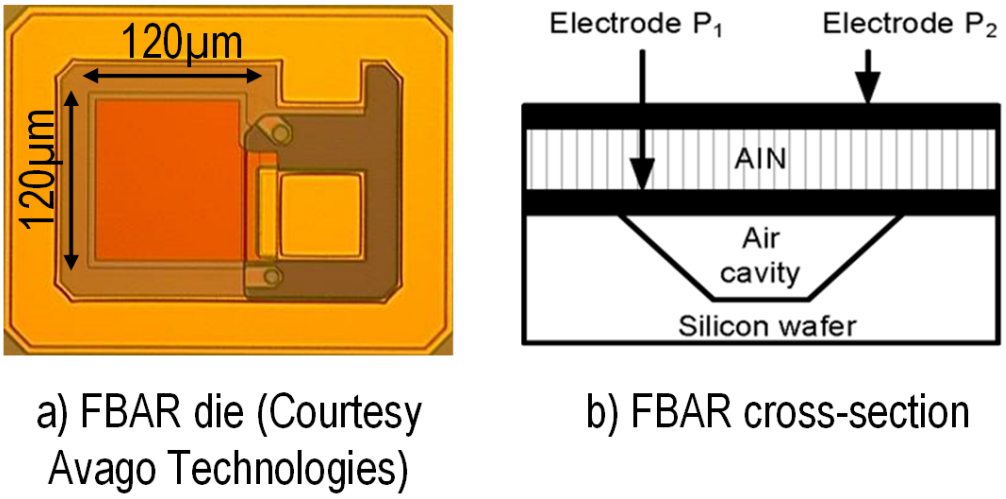

Figure 3.1: FBAR die and cross-section

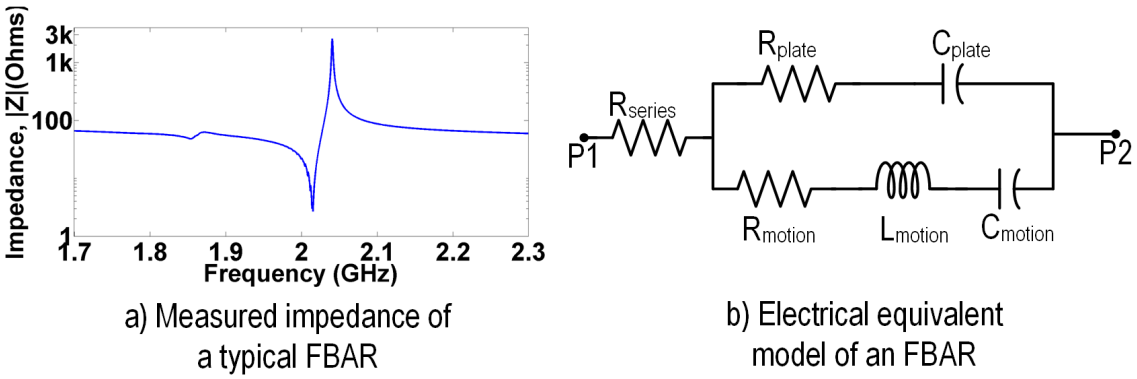

Figure 3.2: Measured Impedance characteristics of a typical FBAR and the electrical equivalent model

New applications in wireless sensor nodes, 'smart dust' can benefit greatly due to a miniaturized, low-power solution for frequency generation using FBAR-based oscillators [30].

3.2 Principle of FBAR Mass Sensor

The resonant frequency of an FBAR is dependent on the thickness of the piezoelectric layer and the acoustic phase velocity. This property could be utilized to sense any added mass or pressure on the FBAR, providing means to further miniaturize the sensing element in a

wireless sensor system. Hence, FBAR's have been explored for their usefulness as a mass sensor due to their high mass sensitivity [56] in a diverse array of fields from healthcare to environmental applications. Some of the medical applications include use in diagnostic tools, detecting protein binding and DNA sequencing [58]. FBAR mass sensors have also shown to be effective in particulate and gas sensing [33]. Recent literature has demonstrated the usefulness of FBAR mass sensors in a multitude of applications, however, none of them demonstrate a miniaturized fully integrated solution using the current manufacturing capabilities of FBAR and circuit fabs available. Additionally, the issue of frequency drift due to the use of the sensor in a real, everyday scenario is not addressed. In this chapter, we report on a miniaturized ($< 1\text{mm}^3$) FBAR-based mass sensor in a commercially viable process suitable for a wide variety of chemical and biological sensing applications. We also propose a temperature and drift compensation scheme to enable operation of FBAR sensors in a real time application.

The operating principle of a FBAR-based Mass Sensor is very similar to that of a Quartz Crystal Microbalance (QCM). Piezoelectric thin films convert electrical energy into acoustic energy and vice versa. A resonance condition occurs if the thickness of piezoelectric thin film (d) is equal to an integer multiple of half the wavelength (λ). Any deposition of a foreign material on the FBAR, adds mass and changes the resonant frequency of the FBAR. The mass sensitivity of a piezoelectric resonator is defined as the ratio of the fractional change in resonant frequency to the added mass as below:

$$S_m = \lim_{\delta m \to 0} \frac{1}{f} \frac{\delta f}{\delta m} \tag{3.1}$$

The mass sensitivity for an FBAR could be derived starting with the equation of the resonant frequency of an FBAR expressed as:

$$f = \frac{v}{2t_p} \tag{3.2}$$

where f is the resonant frequency of the FBAR membrane, v is the acoustic velocity and t_p is the thickness of the FBAR membrane. Additional of a foreign material changes the effective thickness of the FBAR membrane.

$$\frac{df}{dt} = \frac{-v}{2t_p^2} \tag{3.3}$$

$$\frac{df}{f} = -\frac{dt}{t_p} \tag{3.4}$$

$$or\ \frac{\delta f}{f} = -\frac{\delta m}{m} \tag{3.5}$$

where m is the mass per unit area, and ρ is the density of the added material.

This is expressed by the well-known Sauerbrey equation as

$$\delta f = -\frac{2f^2}{NA\rho}\delta m \tag{3.6}$$

The negative sign in the above equations indicate that the resonant frequency of the FBAR resonator reduces with mass deposition. The sensitivity of a single material resonator like a QCM is defined by the Sauerbrey equation (3.6). However, a FBAR resonator cannot be considered a single material resonator as the thickness of the layers other than the piezoelectric membrane, electrodes and the deposited mass, make up a significant portion of the acoustic path. The sensitivity also depends on the surface amplitude normalized to the total acoustic energy in the composite structure. Hence the acoustic properties and the order of the deposited layers influences the sensitivity of the FBAR mass sensor [53]. The elastic properties of the added material itself has a comparable effect as due to mass loading when the thickness of the deposition exceeds roughly 2% of the thickness of the piezoelectric film [56]. However, equation 3.6 could be used to illustrate the first-order behavior of FBAR mass sensors.

3.3 Advantages of FBAR Mass Sensor over QCM

Compared to a QCM, a FBAR-based mass sensor offers some significant advantages. Due to the higher resonant frequency (in the range of a few GHz), the sensitivity of a FBAR-based mass sensor is orders of magnitude higher than a QCM (typical resonant frequencies of a few MHz). Mass sensitivities of FBAR are in the range of 0.37ppm.cm^2/ng [20] while QCM's have a mass sensitivity of 0.018ppm.cm^2/ng [25]. Additionally, FBAR's are smaller in size and the manufacturing process is IC-compatible, which would enable integration of dense sensor arrays enabling low-cost miniaturized sensor systems.

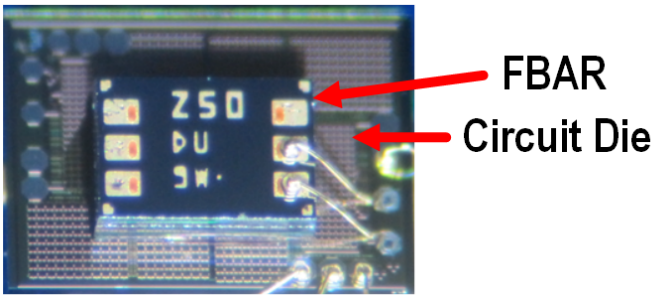

Figure 3.3: FBAR wirebonded to a CMOS oscillator circuit die [26]

3.4 Issues in FBAR-based Sensor

FBAR provides high sensitivity to any added mass, however there are practical limitations in using an FBAR sensor in a everyday environment. The two main issues are integrating the FBAR sensor with the appropriate interface circuitry and isolating the effect of the sensing variable in the output signal from the FBAR sensor.

3.4.1 Integration of FBAR and interface circuitry

Mass sensing based on a FBAR-based mass sensor relies on monitoring the resonant frequency change of the FBAR. Some of the earliest sensors used a Network Analyzer to monitor the frequency changes of the FBAR [56]. Oscillator-based circuits enable monitoring the resonant frequency as well as providing a means of integrating the subsequent interface and signal processing circuitry, enabling the design of a miniaturized sensor system. FBAR-based oscillators have been explored in RF transceiver systems [32] due to their high performance and low power consumption. FBAR oscillators are typically assembled by wirebonding the FBAR to CMOS circuits [36][26]. Figure 3.3 shows a typical arrangement in which an FBAR die is wirebonded to an interface circuit die as demonstrated in [26].

However, such an integration is not feasible for sensor based applications due to the following reasons

- It creates difficult in integrating an array of sensors in close proximity. Applications like DNA sequencing typically require integrating numerous sensors in close proxim-

ity [8].

- Temperature offsets between the sensor and the interface circuitry could result in inaccurate detection.

- Additionally, such an interconnect is open to the environment and monitoring frequency changes due to the sensing variable alone becomes difficult.

Monolithic integration of the MEMS device (FBAR) and the interface circuitry is an active area of research, with attempts to combine the two on a single substrate. The two main approaches for integrating the MEMS device and the interface circuitry depending on the order of integration are

- Pre-CMOS: The MEMS structure is processed first followed by the fabrication of the interface circuitry. The embedded polysilicon structures based on the iMEMS technology proposed by Sandia National Laboratories is such an example [47]

- Post-CMOS: FBAR structures are built on top of the CMOS dice, acting as the substrate [20]. A Bragg reflector type FBAR is built using layers of alternating high and low acoustic impedance. The addition of the Bragg reflector degrades the effective coupling coefficient and the quality factor of the FBAR's

The above methods enable monolithic integration of the FBAR and the interface circuitry reducing the form factor of the sensor system. However, the process requires modification of the existing manufacturing processes for the CMOS circuit or the FBAR fabs. In this work, we propose a monolithic integration technique which utilizes the existing CMOS and FBAR fabs. This greatly reduces the manufacturing cost. Additionally, the FBAR and interface circuitry can be optimized separately depending on the application.

3.4.2 Resonant frequency drift

As we discussed in section 3.3, FBAR is a very good sensor, however this is also a problem in the design of FBAR sensor systems, since FBAR is sensitive to a host of environment

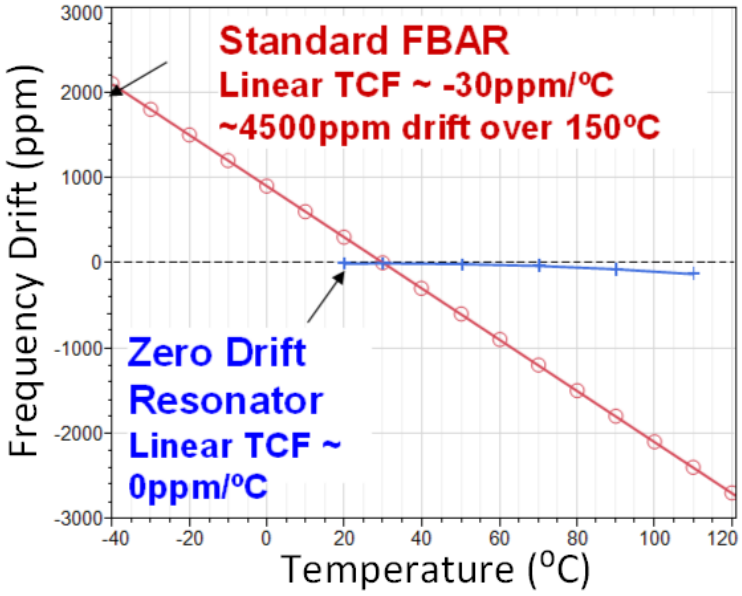

Figure 3.4: Resonant frequency drift of a native FBAR with temperature

variables and isolating the effect of only the required variable is an issue. The resonant frequency of the FBAR is sensitive to environmental variables like humidity, temperature, stress etc. Figure 3.4 shows the dependance of the resonant frequency of the FBAR to temperature. The linear temperature coefficient of a native FBAR is close to -30ppm/°C, degrading the SNR of the sensor. A thin-oxide layer, with an inverse temperature coefficient compared to the piezoelectric membrane, is typically added in the FBAR stack to cancel the first order temperature dependance of the resonant frequency. The thickness of the oxide layer controls the cancellation and turn-over temperature of the resonant frequency drift over temperature. The second order temperature coefficient still results in a resonant frequency drift of close to 200ppm over a temperature range of -20°C to 70°C as shown in Figure 3.5.

The FBAR resonant frequency is also sensitive to environmental variables like humidity, stress and natural aging of the resonator. Highly Accelerated Stress Test (HAST), in which the FBAR is exposed to 110°C and 85% relative humidity for a long time ($>$ 100hours)show frequency drifts of the order of 80ppm [9]. The dependance of the resonant frequency on

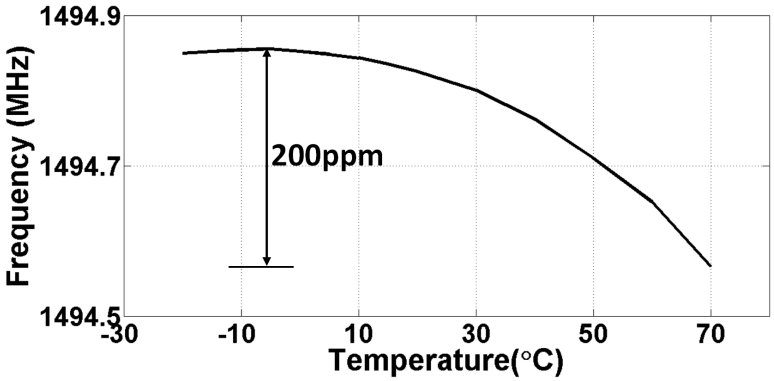

Figure 3.5: Resonant frequency drift of a temperature compensated FBAR with temperature

temperature and enviormental variables severely limits the SNR and the accuracy of FBAR sensors, with the signal being in the range of a few ppm for $<$ 1ng mass detection. In the next couple of sections, we present the design of an FBAR based mass sensor to address the issues highlighted in this section.

3.5 FBAR Mass Sensor Design

A technique for integrating active circuitry into the lid of the wafer-scale hermetic FBAR package was demonstrated in [46]. The process involves fabricating the FBAR and the circuit wafer separately using the conventional process. The cavity under the FBAR is defined and filled with a sacrificial oxide, the resonator is then processed, followed by the patterning of the Au interconnect and sealing material and finally, removing the sacrificial oxide. The circuit wafer is manufactured using standard micromachining process with through-wafer vias, Au pads, sealing structures, and a recessed air cavity above the FBAR. The Si micro-cap lid is then Au-diffusion bonded to the FBAR wafer and pads patterned on top.

A wafer-scale integration process enables use of existing processes for the FBAR and the circuit wafer fabrication, maintaining native device performance and the ability to quickly optimize the sensor depending on the application. Integration of the active circuitry in the lid eliminates external connections between the FBAR and the interface circuitry resulting

in a miniaturized hermetic package. More importantly, it leverages the high-volume manufacturing capability of the existing CMOS and the FBAR fabs, drastically reducing the development cost.

As discussed in the previous section, the FBAR resonant frequency is sensitive to changes in temperature, humidity, stress and other environmental variables. A frequency drift cancellation scheme encompassing the above variables is essential. In this work, we propose to use a second FBAR (reference FBAR) in close proximity to sense the changes in the environmental variables and cancel the frequency drift. The sensing variable (mass) is applied to only the sensor FBAR while the environmental variables affect both the sensor and the reference FBAR and a differential measurement of the frequencies of the two FBAR's provides an accurate representation of the mass.

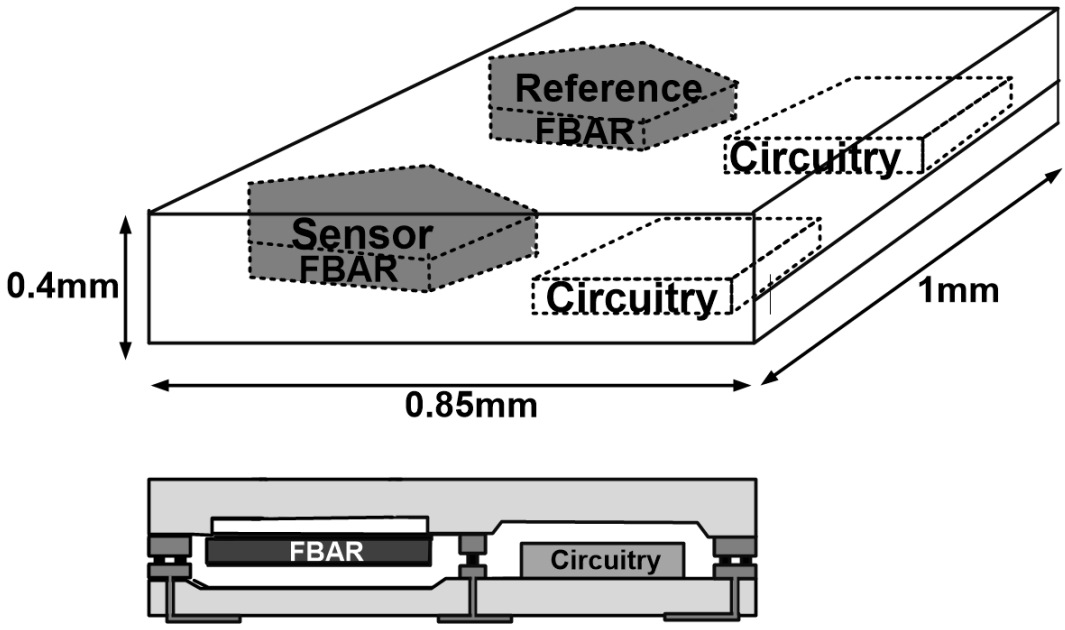

Figure 3.6: Cross-section of the Proposed FBAR/IC process

Figure 3.6 shows a 3D view of the sensor with the interface circuitry in a single hermetic package. Two FBAR dies are integrated within a distance of several microns and the lid houses the active interface circuitry. For this demonstration, a 1.5GHz FBAR stack and the Avago HP25 silicon bipolar process was used for the lid wafer. The total size of the FBAR

sensor together with the sensor interface circuitry is $(0.85 * 1 * 0.4)\text{mm}^3$

3.5.1 DRIE Processing

A wafer-scale integration method provides a hermetically sealed FBAR sensor along-with the interface circuitry and is immune to any sensor inputs. However, the FBAR sensor resonator needs to be exposed to the outside world for mass deposition. A Deep Reactive-Ion Etching (DRIE) process is used to expose the FBAR sensor ensuring the application of the sensor variable (mass) on the sensor FBAR alone. The standard Bosch DRIE process, which incorporates a time-multiplexed etching and passivation layer deposition is adapted to suit our needs. The requirements with regards to the aspect ratio are fairly relaxed in this context.

The 6inch bonded FBAR-CMOS wafers were diced into sections (4cm * 6cm) and then bonded to glass wafers using a temporary water soluble adhesive to allow for back-to-front alignment. A 7μm film of photoresist was spun on the wafer opposite the contact pads and was exposed using a contact aligner. Next, holes were etched using an inductively coupled plasma (ICP) etcher with a time-multiplexed $SF6, C4F8$ process. The bottom electrode for the 1.5GHz stack is typically 200nm thick and due to the absence of a stop layer, frequent monitoring of the etch depth is mandatory. The etch depth was monitored using optical profilometry. This process creates etch holes roughly 80μm in diameter and 250μm deep, allowing access to the FBAR membrane. Figure 3.7 shows the SEM of the etch hole on the sensor and Figure 3.8 shows the final cross-section of the FBAR mass sensor.

3.6 Sensor Interface Circuitry Design

The change in the resonant frequency of the FBAR is monitored by interfacing with an FBAR-based oscillator. The noise performance of the interface circuitry directly impacts the resolution of the sensor. Since we are interested in monitoring frequency changes, the resolution (or minimum detectable frequency change) of the sensor would be set by the frequency change due to the noise sources. We look at understanding and characterizing the noise performance of the oscillator to determine the resolution of a FBAR-mass sensor.

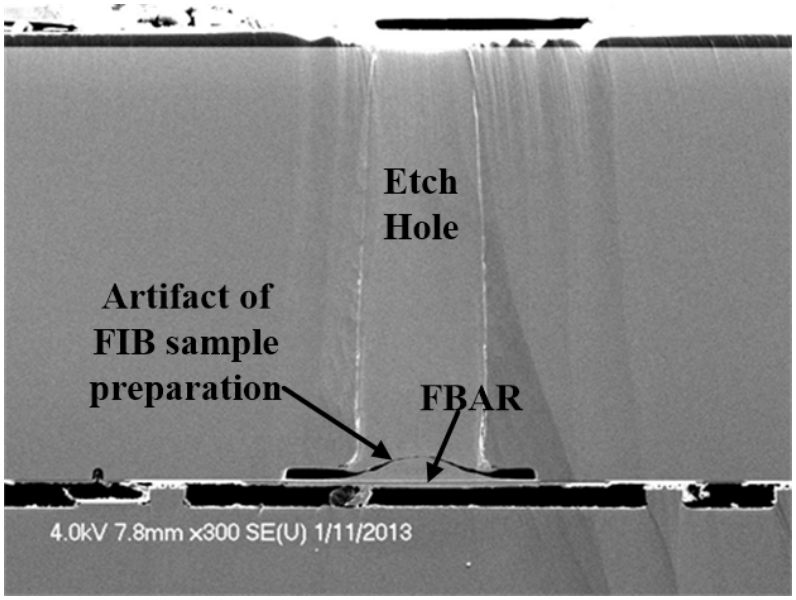

Figure 3.7: SEM of the etch hole to expose the FBAR sensor

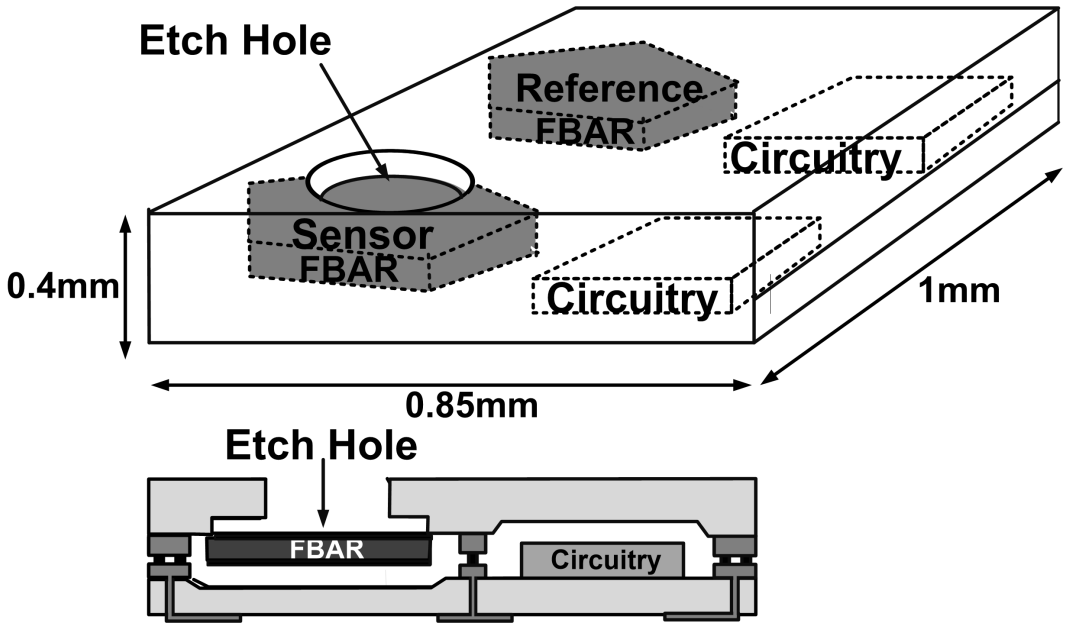

Figure 3.8: Cross-section of the FBAR Mass Sensor

3.6.1 Resolution of the FBAR Mass Sensor

Oscillator performance is typically characterized by the phase noise behavior in wireless communication systems. However, characterizing sensor performance requires the integration of the phase noise over different sampling intervals (depending on the application) and the drift performance of the oscillator. This would require integration of the noise over the sampling time over which the frequency changes of the sensor is monitored. The drift of the oscillator over the sampling time also adds to the uncertainty in the frequency and hence degrades the resolution.

3.6.2 Sensor Interface Circuitry Details

Figure 3.9 shows the system block diagram of the wireless sensor with the oscillator circuitry. A low noise Pierce oscillator monitors the resonant frequency of the FBAR. The resolution of the sensor is limited by the integrated phase noise and the frequency drift. The far-off phase noise in an FBAR oscillator is very low due to the high quality factor of the FBAR and hence does not limit the resolution of the FBAR sensor. A bipolar transistor for the gain transistor helps to reduce the flicker noise to improve the resolution. The sensor oscillator was intentionally pulled by a few ppm to prevent any injection locking of the two oscillators.

The output from the oscillator is AC-coupled to an RF buffer able to drive the antenna. The finite base current in bipolar transistors shunts the R_p of the FBAR and de-Q's the resonator. Loading on the FBAR oscillator tank must be minimized to maintain jitter performance, placing tough design constraints on the bipolar buffer amp. A self-biased Darlington pair (Q4, Q5) is used to reduce de-Qing and load pulling on the FBAR. A resistor, R5 provides a low-impedance discharge path for the charge accumulated on the emitter-base junction, allowing a faster transistor turn-off, suitable for high frequency amplifiers. The two output tones are combined in a tapped capacitor transformer and transmitted wirelessly to a receiver. The bias circuitry is fully integrated and derived internally.

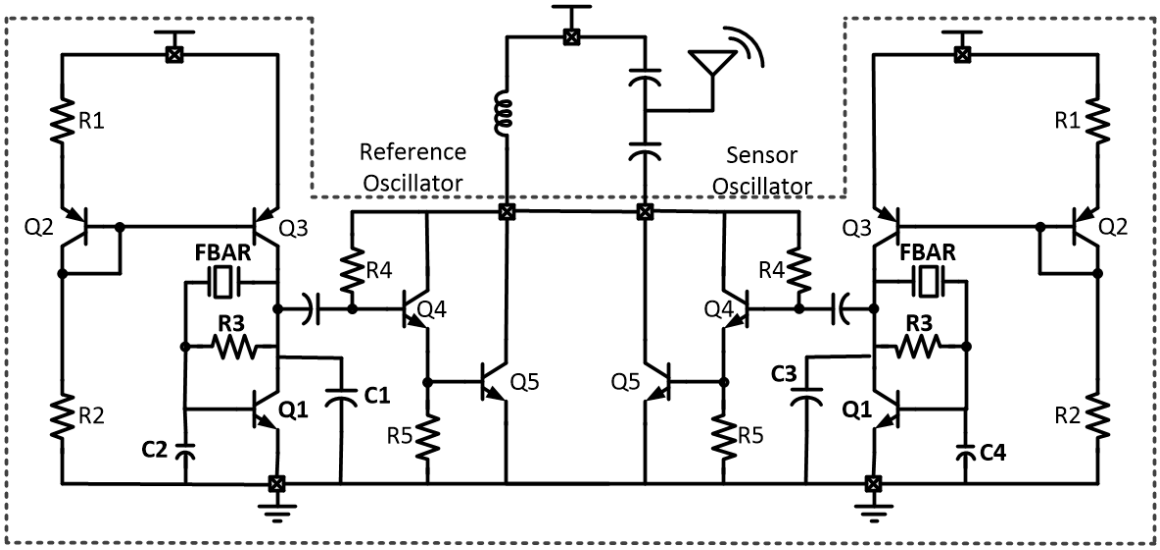

Figure 3.9: FBAR-Mass Sensor Interface Circuit

3.7 Experimental Results

3.7.1 Mass Sensing

A thin film metal deposition experiment was carried out at the wafer level to verify the effectiveness of the chemical etching process. A mixture of gold and palladium (60%Au, 40%Pd) was deposited across the entire wafer. The thickness of the deposition itself was monitored by means of the instrument, using a QCM. The average value of the thickness of the metal deposited was $10 - 40$nm across different samples. A mean frequency shift of 1.3MHz and 2.3MHz were recorded after the first and second deposition accordingly (Figure 3.10). The diced sensors were then flip-chipped on a FR4 2-layer PCB. A thin film SiO_2 sputtering experiment was done to characterize the sensitivity of the sensor. The thickness of the deposition was estimated from the QCM-based instrument and a SEM across multiple dies. Using a conservative estimate of the film thickness and knowing the diameter of the etched hole, the mass of the deposited SiO_2 is 0.29ng. A frequency deviation of 0.75MHz was measured across two sensor oscillators. The sensitivity is calculated to be 2.54 kHz/pg or 0.45 kHz.cm^2/ng (normalizing to the area of the FBAR).

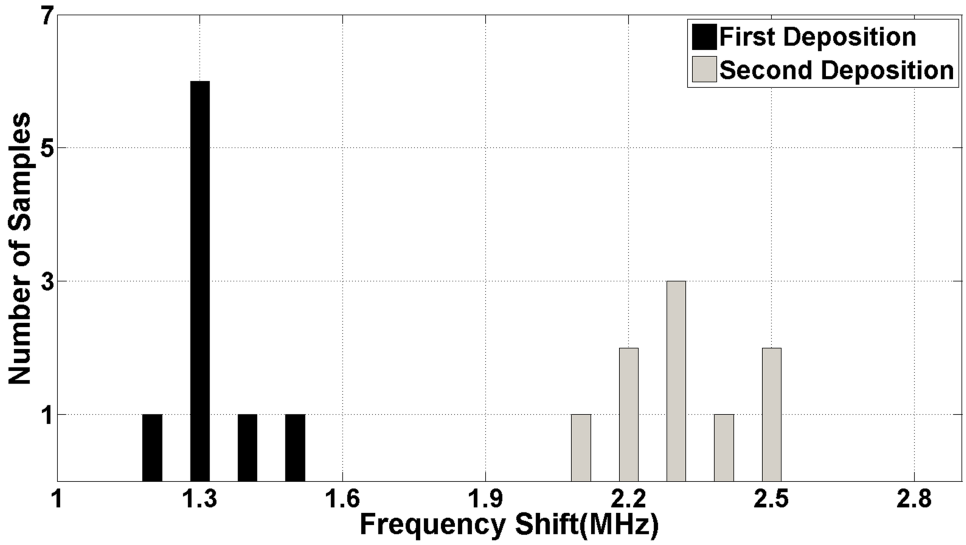

Figure 3.10: Thin-Film metal deposition experiment at the wafer level. A mixture of (60%Au, 40%Pd) was sputtered on the sensor wafer (and then repeated).

3.7.2 Frequency Drift Cancellation/Accuracy

Figure 3.11 shows the change in frequency of the two oscillators over a temperature variation of -20 to $70\,^{\circ}$C. The frequency change due to temperature variation for a single oscillator is 205ppm. The two resonators experience the same temperature drift due to their close proximity. By monitoring the difference frequency, the frequency change due to temperature variation over -20 to $70\,^{\circ}$C is reduced to 19ppm, reducing the inaccuracy from 120.5pg to 11.1pg.

3.7.3 Resolution of the mass sensor

The resolution of the mass sensor is determined by the minimum detectable frequency shift. Averaging the frequency measurement over time improves the resolution since the thermal noise is averaged out. However, flicker noise dominates and increasing the integration time beyond a point degrades the frequency measurement. The minimum frequency drift that can be detected is thus a measure of the stability or the Allan deviation of the FBAR oscillator. Figure 3.12 shows the Allan deviation measurement of the mass sensor. The

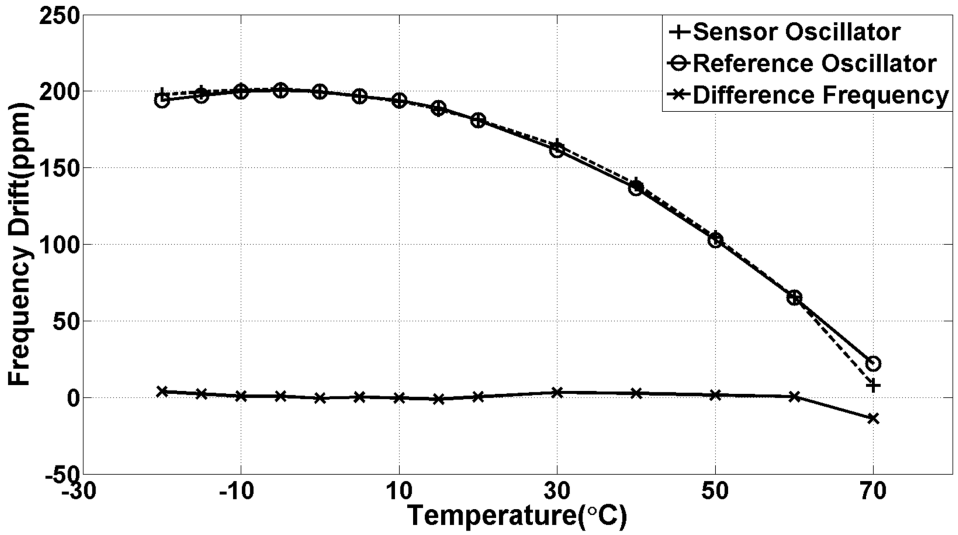

Figure 3.11: Frequency drift cancellation due to temperature variation using a reference oscillator

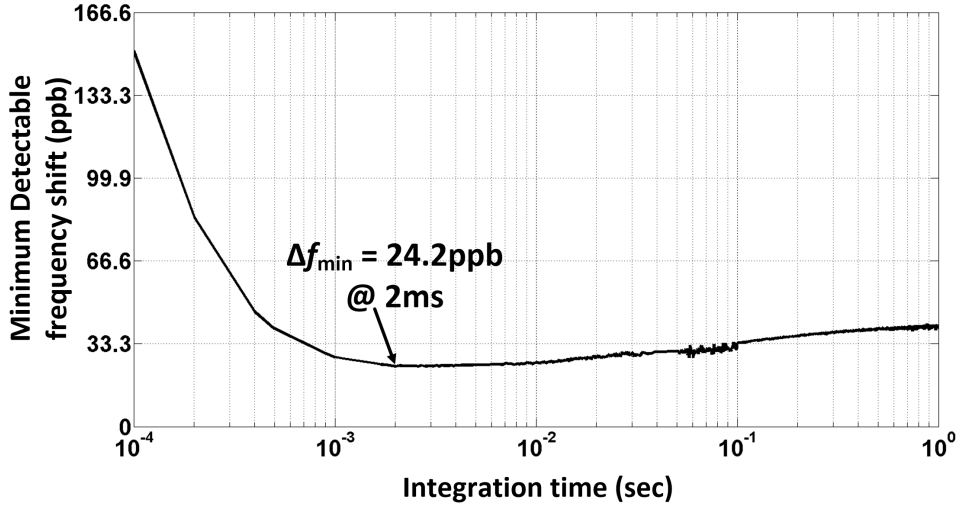

Figure 3.12: Allan Deviation Measurement to characterize the resolution of the mass sensor

minimum detectable frequency shift is 24.2 ppb at an integration time of 12 ms. This translates to a mass sensor resolution of 70 fg.

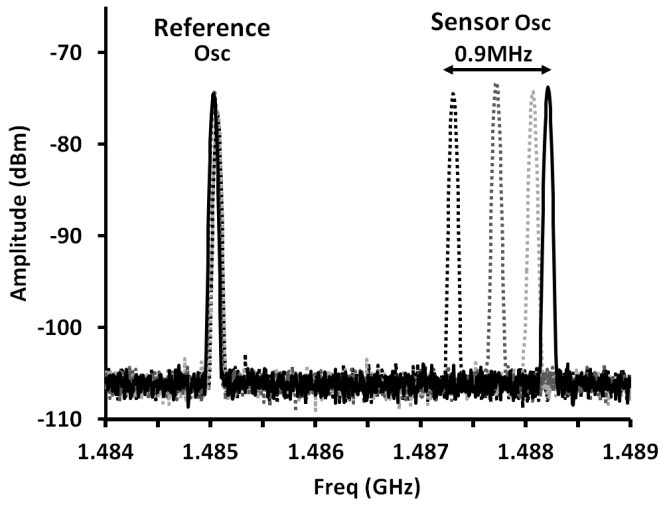

Figure 3.13: Wireless spectrum showing the received signal from the sensor before and after various amounts of mass loading with IPA.

3.7.4 Example Application: Humidity Sensing Experiment

To demonstrate operation in wireless over-the-air scenarios, an example mass sensing experiment was carried out using isopropyl alcohol (IPA). Figure 3.13 shows the received spectrum at a range of 2m. Varying amounts of IPA were pipetted onto the chip, resulting in a frequency shift of the sensor oscillator up to 910 kHz. The frequency of the hermetically-sealed reference oscillator was unchanged.

A subsequent experiment to measure the relative humidity (RH) was carried out. Adsorption of water molecules on the sensor changes the resonant frequency. Figure 3.14 shows the measured data of the sensor over two sweeps of RH from $15 - 70\%$. The hermetically sealed reference shows little variation while the sensor oscillator frequency varies by 0.7MHz. The response time of the sensor for increasing humidity was about 1 minute. However, the reverse process of losing the water molecules from the surface of the sensor has a longer response time of about 15 minutes due to the small dimensions of the etch hole.

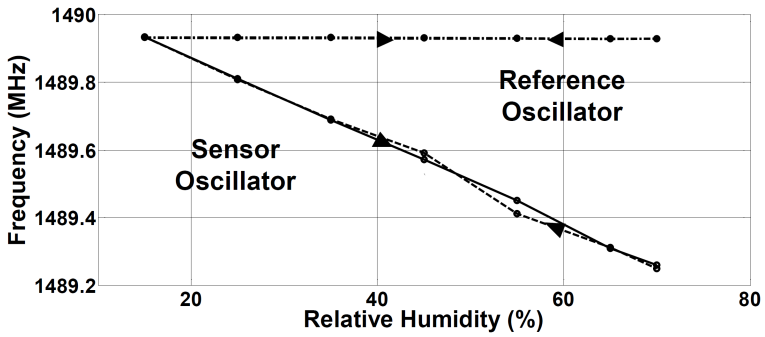

Figure 3.14: Relative humidity (RH) was swept from $15 - 70\%$ and repeated.

3.8 Conclusion

We have taken the first steps towards the design of a fully integrated FBAR-based mass sensor. Table 3.1 compares state of the art FBAR mass sensors with our work. Compared to other FBAR mass sensors, we have for the first time proposed an extremely miniaturized sensor with a reference FBAR that is hermetically sealed to cancel the temperature and drift component. We achieve this in a commercial process which involves sealing the FBAR and the circuit lids together to form a hermetic package. For this experiment, we have used an Avago silicon bipolar process, but the process remains same for any commercial CMOS process.

Table 3.1: Performance Summary and Comparison of Mass Sensors

	This work	[20]	[27]	[21]
Sensor Type	FBAR, mass sensor	FBAR, mass sensor	FBAR, mass sensor	FBAR, mass sensor
Processing Comments	Wafer scale bonding of IC and FBAR	FBAR + processing to build CMOS on top	CMOS + back end processing of FBAR	No circuitry, measures resonant frequency on Network Analyzer
Sensitivity (kHz.cm^2/ng)	0.45	0.328	5.704	3.65
Power Consumption	14.7mW	Not reported	Not reported	Passive
Size	0.02mm^2 (0.34mm^2)	15mm^2(24 sensor array)	100mm^2(64 sensor array)	Bench top
Temperature and Drift compensation	Yes	No	No	No
Wireless Connectivity	Yes	No	No	No

Chapter 4

A sub-mm^3 FULLY INTEGRATED PRESSURE SENSOR

Silicon micro machining has enabled the design of miniaturized sensors useful in a diverse array of fields. We studied the feasibility of one such sensor (mass sensor) in the previous chapter. Another important physical variable to be monitored is pressure. Pressure sensors are increasingly being used in automotive applications (TPMS), smart phones, tablets and wearable technology. Miniaturized fully integrated pressure sensors enable new applications in healthcare, indoor navigation etc and helps to reduce cost in established application scenarios. In this chapter, we explore the feasibility of fully integrated FBAR-based pressure sensor. FBAR-based sensors provide the following advantages compared to traditional voltage-output sensors as listed below:

- The output variable from an FBAR-based sensor is in the form of a frequency value providing a digital ready value without the need for an explicit analog-to-digital converter (ADC).

- The frequency output from an FBAR-based sensor is amenable for wireless transmission, providing a very mobile and convenient sensor. It also offers deployment in tough-to-reach environment.

- The interface circuitry could be designed in modern CMOS technologies and thereby provide a low-cost solution.

In this work, we target a pressure sensor suitable for tire pressure monitoring in automobiles. Tire Pressure Monitoring Systems (TPMS) provide real-time monitoring of tire pressure when the vehicle is in either in motion or stationary. The dynamic behavior and safety of an automobile tire is closely dependent on its inflation pressure and the primary benefits of maintaining the manufacturer-recommended pressure are as follows:

- **Safety:** Under-inflated tires increases the peak stress leading to tread separation and risk of catastrophic tire failure. It also reduces stability of the vehicle, reduces handling and the the vehicle's safe linear stopping distance [49].

- **Fuel Savings:** Under-inflated tires experience more friction and hence a reduction in the fuel efficiency of the vehicle. Statistics indicate, for every 10% of under inflation, the fuel economy of the vehicle reduces by 1%. The Department of Transportation in the USA estimates that under-inflated tires waste 2 billion US gallons of fuel each year.

- **Extended Tire Life:** NHTSA estimates maintaining proper tire pressure as specified by the 25% compliance option required by the Tread-Act, average tread life of the tire increases by 1150 miles [49].

- **Greenhouse gas emission reductions:** Maintaining manufacturer recommended tire pressure helps reduce unnecessary CO_2 emissions and decreases tire waste.

Thus, Tire-Pressure Monitoring Systems (TPMS) have become an essential component in modern vehicles as stipulated by the National Highway Traffic Safety Administration (NHTSA) in 2006 in the United States. The European Union made the adaption of TPMS mandatory for new vehicles in November, 2012. This was followed by other countries like South Korea, Russia, Indonesia, Phillipines, Israel, Malaysia and Turkey. Following the legislation, the global demand for TPMS is expected to be 54.77 million sets in 2017 with an average annual growth rate of 16.83%.

State-of-the-art TPMS systems currently require a pressure sensor, multiple ICs, several external components, and a crystal on a PCB allowing wireless transmission of tire pressure [7] [14]. In this work, we describe a sub-mm^3 fully-integrated wireless pressure sensor including a pressure transducer, interface circuitry, integrated timing reference, and a wireless transmitter integrated into a single die.

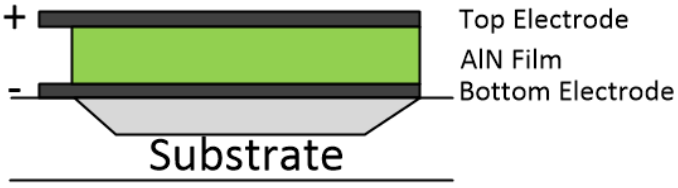

Figure 4.1: Cross-Section of an FBAR

4.1 Principle of FBAR Pressure Sensor

The structure of a FBAR is shown in the Figure 4.1. The piezoelectric thin film converts electrical energy into acoustic energy and vice versa. A resonance condition occurs in the FBAR when the thickness of the piezoelectric thin film (d) is equal to an integer multiple of a half wavelength. The acoustic wave propogation is along the thickness of the film (longitudinal). The fundamental frequency of the FBAR in this case is a function of the phase velocity of the acoustic wave and the thickness of the piezoelectric film and is given by

$$f_{resonant} = \frac{V_a}{2d} \tag{4.1}$$

The phase velocity of the acoustic wave propagating in the piezoelectric membrane is related to the stiffness matrix, c_{eff} and the mass density ρ of the membrane as:

$$V_a = \sqrt{\frac{c_{eff}}{\rho}} \tag{4.2}$$

According to Hooke's law, the deformation/strain (S) of an elastic object/piezoelectric membrane is proportional to the Stress (T) applied to it. Some of the strain also changes the electric field (E) across the membrane. This behavior is summarized in the following equation:

$$T = c^E S - eE \tag{4.3}$$

where $'c'$ is the stiffness co-efficient matrix at constant electric field and $'e'$ is the piezoelectric stiffness. Equation 4.3 provides the first-order behavior of the FBAR. Recent studies

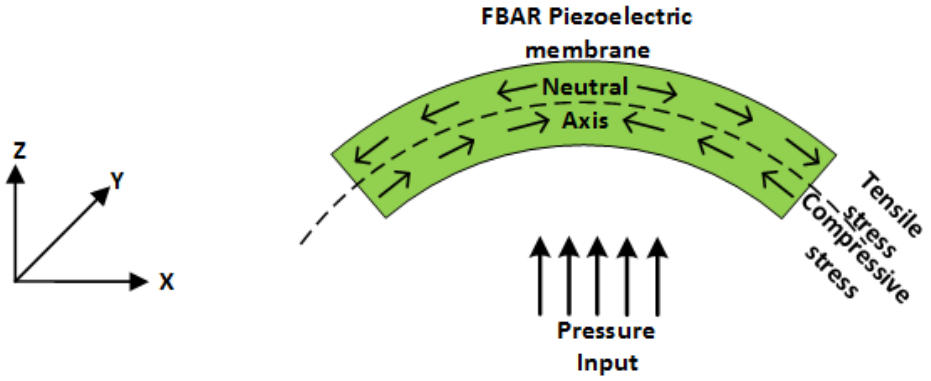

Figure 4.2: Stress diagram of FBAR with pressure input

have proposed a non-linear model to model the second harmonic (H2) and intermodulation distortion (IMD3) data simultaneously [45]

$$T = c^E S - eE + \Delta T \tag{4.4}$$

$$\Delta T = -\delta_1 eSE + \frac{\delta_2 \epsilon^S E^2}{2} + \frac{\delta_3 c^E S^2}{2} \tag{4.5}$$

By providing a sealed cavity on one side of an FBAR, application of pressure on the other side introduces a bending stress on the membrane, as depicted in the figure 4.2. A tensile and a compressive stress appear on either side of the neutral axis, along the z-direction. We now proceed to analyze the effect of the bending stress on the FBAR membrane.

4.1.1 Effect of Stress on the stiffness coefficient, c

We first consider the effect of stress on the stiffness coefficient and confine the effects only up to the 2^{nd} order in the equation defined in 4.5 and simplify equation 4.5 using stiffness coefficient matrices c_1 and c_2 for the first and the second order effects. The equation 4.4 could then be rewritten as below:

$$T = c_1 S - c_2 S^2 \tag{4.6}$$

The piezoelectric membrane has an initial stress, S_{DC}, developed by the manufacturing process. By providing a sealed cavity on one side of an FBAR, application of pressure on the

other side introduces a bending stress on the membrane. We then consider this additional stress, S_{AC} and rewrite the equation 4.6 as

$$T = c_1(S_{DC} + S_{AC}) - c_2(S_{DC} + S_{AC})^2 \tag{4.7}$$

S_{DC} could be thought of as an operating point and S_{AC} as a small signal input on the FBAR membrane. Expanding and rearranging equation 4.7, we get,

$$T = (c_1 + 2c_2S_{AC})S_{DC} + c_2S_{DC}^2 + c_1S_{AC} + c_2S_{AC}^2 \tag{4.8}$$

Considering the first part of the equation 4.8, we see that the effective stiffness matrix is now

$$c_{eff} = c_1 + 2c_2S_{AC} \tag{4.9}$$

From 4.2, the phase velocity of the acoustic wave and hence the resonant frequency of the FBAR is dependent on the effective stiffness coefficient. The effective stiffness coefficient is dependent on the additional stress, S_{AC} for a buckling piezoelectric membrane due to a pressure input. This creates a pressure-to-frequency transducer.

4.1.2 Effect of Stress on the Electric Field, E

A stress along the z-axis of the FBAR, results in a strain in the x and the y direction. Writing the equation for the stress in the z-direction from equation 4.3, we have

$$T_z = c_{zz}S_z + c_{xz}S_x - eE \tag{4.10}$$

The pressure input on the FBAR, produces a buckling stress on the FBAR as illustrated in the Figure 4.2. The piezoelectric material experiences a Tensile and a Compressive stress above and below the neutral axis along the z-axis. Hence we can write,

$$\sum T_z = 0 \tag{4.11}$$

The strain and the electric field are inter-related and we would need two more equations for solving the 3 variables. Instead, we simulate the effect of the pressure input in a computer-aided simulation program (COMSOL) and figure out the strains, S_x and S_z. We assume a

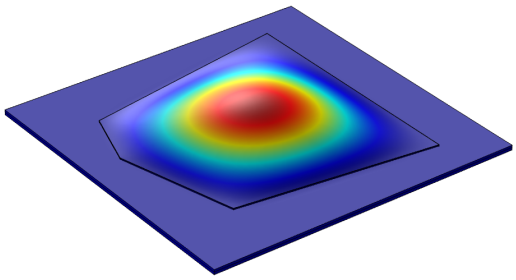

Figure 4.3: COMSOL Simulation of FBAR Pressure Sensor

Aluminium Nitride (AlN) piezoelectric membrane, with a thickness of 1.35μm. Appropriate thickness for the top and the bottom electrodes and the passivation were assumed. Figure 4.3 shows the 3D model of the FBAR with a pressure input of 30psi. A strain in the x-direction, $S_x = 36.4\mu m/_m$ and in the z-direction, $S_z = 31.4\mu m/_m$ was measured with simulation. Knowing the constant c_{zz} and c_{xz} for AlN, we calculate the electric field generated due to the applied pressure is $1.02V/\mu$m. Typical measurements have indicated a frequency shift of close to 26ppm with an electric field of $1V/\mu$m across the AlN FBAR.

4.2 FBAR Pressure Sensor Design

Figure 4.4 describes the process flow for fabricating an FBAR-pressure sensor. A common scheme for fabricating FBAR filter membranes is to deposit a sacrificial oxide under an active FBAR membrane that is later removed using wet chemical etching through small release holes [46]. However, this process cannot be used to create a sealed cavity because the release holes directly connect two sides of the membrane making the differential pressure

zero. Instead, we create a true sealed cavity by forming a hole using an anisotropic silicon etch and then removing the sacrificial oxide via a second wet etch. The closed cavity for pressure sensing is inherently provided by the hermetically-sealed lid which, in our case, houses the active interface circuitry. The FBAR wafer is fabricated with and without release holes for the reference resonator (left FBAR) and the sensor resonator (right FBAR). The FBAR wafer is then bonded to a Si micro-cap lid wafer that consists of the CMOS circuitry to obtain a hermetically-sealed FBAR-CMOS die. Deep-Reactive-Ion-Etching (DRIE) is used to release the right FBAR membrane and provide a channel for the pressure to access the membrane. The channel diameter is $80\mu m$. After DRIE, the entire wafer is placed in $10:1$ deionized water to 49% hydrofluoric acid to remove the sacrificial oxide and release the sensor FBAR (2^{nd} etch). The process flow uses standard micromachining process throughout, making it commercially viable in mass production.

Both FBAR resonator frequencies are also sensitive to temperature, board/package stress, aging etc. To cancel these effects to first order, we use two FBARs (reference and sensor FBAR) in the same die. They are in close proximity ($10s$ of microns), allowing precise matching of frequency drift. The reference FBAR also provides a frequency reference for wireless communication.

4.3 Sensor Interface Circuitry Design

The design goal of the interface circuitry is to monitor the resonant frequency of the FBAR while also maintain a good accuracy in the presence of temperature drift and external stress on the package. The output from the FBAR pressure sensor is an RF frequency which can be transmitted wirelessly to an off-chip receiver. Hence, the raw frequency data is transmitter to an off-chip receiver while doing as little processing as required in the sensor chip to reduce power consumption. Figure 4.5 shows the architecture of the sensor interface.

An oscillator circuit monitors the resonant frequency of the FBAR. A matched FBAR in close proximity acts as a reference to cancel out the frequency drift due to unwanted variables. A differential measurement of the frequencies provides an output proportional to the sensor variable (pressure). The output from the two oscillators are combined in a multiplexer and transmitted wirelessly in a pseudo-FSK modulation scheme. 628 MHz

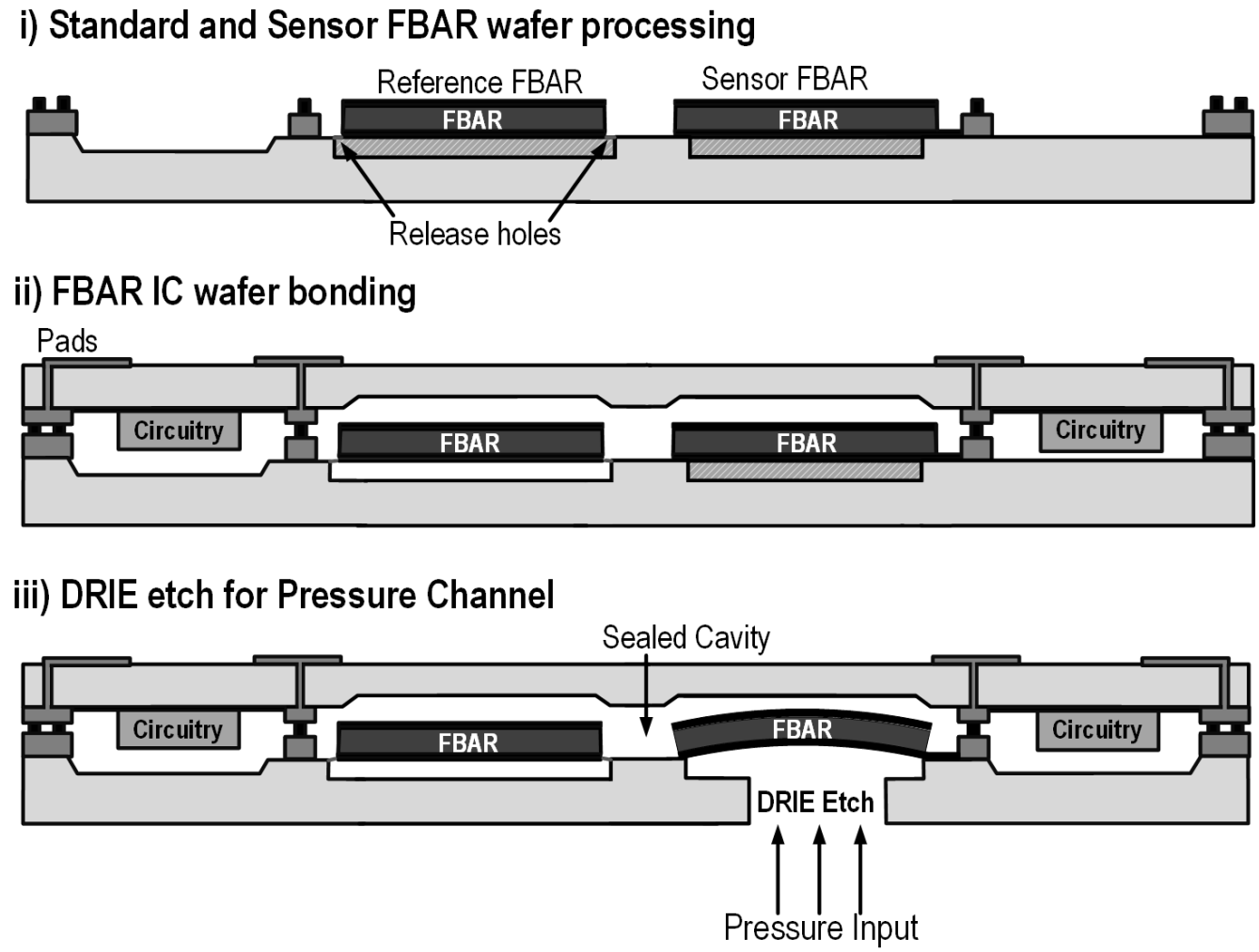

Figure 4.4: Process flow for reference and pressure sensor FBAR and final cross section of the FBAR/IC pressure sensor

FBAR's were chosen to provide a frequency output compatible with the standard for short range wireless links at 314MHz.

The symbol rate for the FSK transmission is a divided down version of the reference frequency, while the frequency deviation provides a measure of the sensor frequency/pressure input. The division ratio dictates the time over which the sensor frequency can be pro-

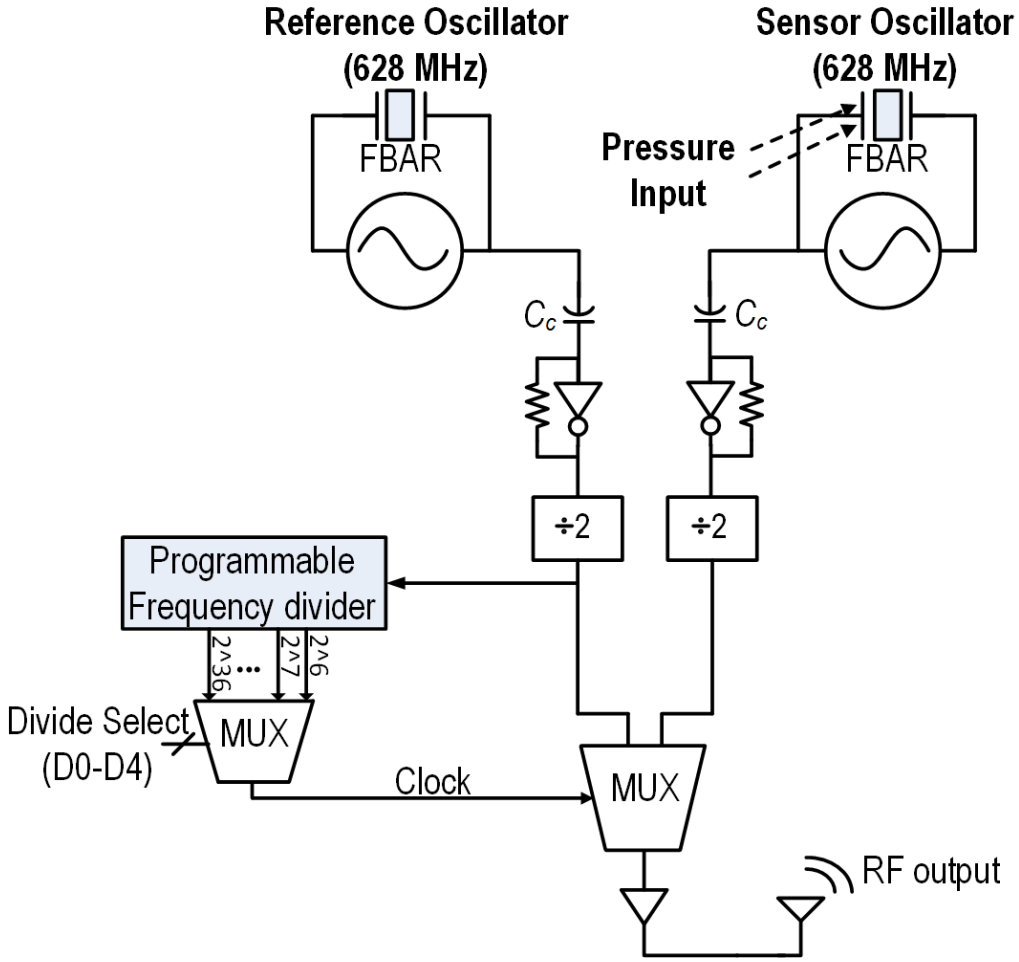

Figure 4.5: Architecture of the Pressure Sensor Interface IC

cessed/integrated at the receiver. This integration time is fully programmable to trade noise for power consumption (active duty cycle). Typically, integration time for minimum Allan deviation is in the range of $10 - 100$ms for FBAR oscillators. The start-up time of a FBAR oscillator ($< 10\mu$s) is negligible compared to the time required for minimum Allan deviation.

An FSK receiver providing the value of frequency deviation could be used to estimate the sensor variable (pressure). More information could be obtained from the received signal by calculating the individual frequencies. The data rate of the transmission is a measure of the

reference frequency and the frequency deviation value then provides the sensor frequency.

Design of the Sensor Interface Oscillator The oscillator interface with the FBAR resonator directly impacts the resolution of the sensor. The FBAR resonant frequency was monitored with a pierce oscillator structure. The design goal of the oscillator design is to reduce the integrated jitter to improve the sensitivity of the sensor. Thermal noise is typically not a concern in sensor systems since the frequency measurement is averaged over a sampling time range of ms to s. The high-Q of the FBAR resonator further helps in the reduction of the thermal/far-off noise. The thermal noise floor is limited by the on-chip buffers following the oscillator. The sizing of the buffers was carefully chosen for minimum integrated jitter.

Flicker/Close-in phase noise is more of a concern in FBAR-based sensor interface. The flicker noise in high-Q oscillators is dominated by the amplitude modulation to phase noise conversion as demonstrated in [44]. A compensation capacitor providing an inverse voltage transfer function compared to the parasitic capacitance at the node was used. The mean value of the compensation capacitor used is $100fF$. Figure 4.6 shows the circuit diagram of one pierce oscillator.

The interface circuitry was fabricated using the Avago 0.6μm CMOS process. The IC wafer was subsequently bonded with the FBAR wafer to obtain a fully integrated wireless pressure sensor. Figure 4.7 shows the die photo of the FBAR die and the circuit die before the wafer scale bonding process. The total size of the die, including the sensor, reference FBAR and the interface circuitry, is (2.20.90.4) mm^3. Figure 4.8 shows the SEM of the die and the etch hole with the FBAR base die (wafer) and the circuit die (wafer) annotated. The sensor FBAR was released (dissolution of the sacrificial oxide) through a wet etch by dipping the entire wafer in HF after the DRIE process.

4.4 Experimental Results

The pressure sensor was soldered on a FR4 PCB measuring $1 * 2$mm^2. The sensor output was monitored on a spectrum analyzer. A custom pressure chamber which could handle pressures upto 300psi was designed to test the pressure sensor. The complete setup is shown in Figure 4.9. The setup consists of a pressure regulator to control the pressure inside the

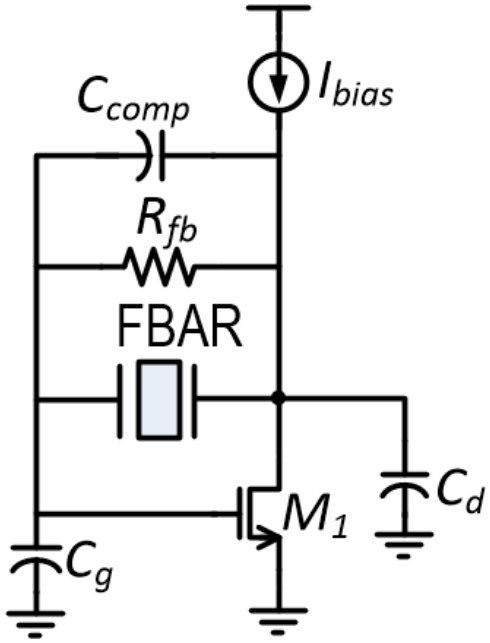

Figure 4.6: Circuit diagram of the Oscillator for the sensor interface

chamber, and hermetically sealed connectors to provide the electrical feed-throughs and maintain the pressure. A safety valve was included and the pressure sensor was mounted inside the chamber. Figure 4.10 shows the output (with the max hold function) at a distance of 2m. The pressure sensor performance was characterized for typical sensor metrics.

Figure 4.11 shows the response of the sensor to a pressure input. The sensor FBAR frequency reduces with increased pressure with a sensitivity of 2.2ppm/psi. The reference FBAR frequency stays constant due to the hermetic seal. The dynamic range of the sensor is $20 - 70$psi. The FBAR sensor can buckle in both directions. Hence there is a crossover point at 0psi for the frequency shift over pressure. The relative frequency shift was mapped to pressure changes using a linear fit. Figure 4.12 shows the final pressure readings from the sensor and the actual pressure values. The performance of the oscillator was observed at different pressure conditions and the noise performance did not show any observable degradation in the phase noise.

The pressure resolution is primarily limited by the minimum detectable frequency shift in the oscillator. The minimum detectable frequency shift is determined by the Allan deviation

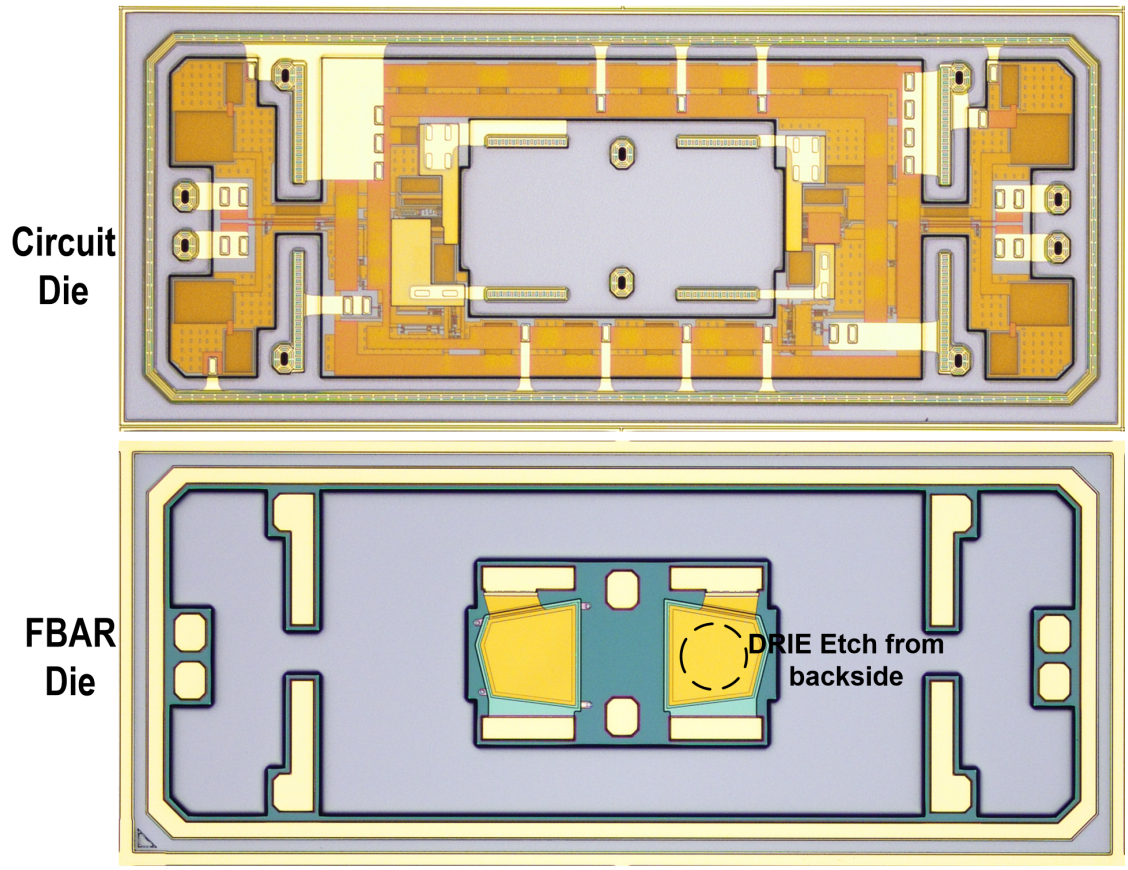

Figure 4.7: Die photo of the IC and FBAR wafers before hermetic bonding and etching

measurement for an oscillator, which characterizes the stability in frequency references. Averaging of the frequency measurements improves the minimum detectable frequency shift. However, at higher sampling intervals, the measurement is limited by the flicker noise of the oscillator. Figure 4.13 shows the Allan deviation measurement of the sensor. The minimum Allan deviation was measured as 1.6 ppb at an integration time of 12 ms. This is equivalent to a pressure resolution of 0.72 mpsi

The sensor system consumes 4.7 mA from a 2.7 V supply. The sensor could be operated either in a duty-cycled mode where the system transmits the pressure (frequency) infor-

mation of the sensor FBAR and the frequency FBAR once in every refresh cycle or in a continuous mode. The duty cycle could be adjusted to get the best resolution for which each of the sensor and the reference frequency should be transmitted for a duration equal to the minimum Allan deviation integration time (12 ms) as illustrated in Figure 4.13. For a refresh rate of transmitting the pressure information every 10 s, the average power consumption is around 30μW. With a battery capacity of 500mAh available from most-common TPMS batteries, this translates to a lifetime of $>$ 5.5 years. Continuous reporting of tire pressure requires instantaneous tracking of the frequency shift of the sensor. A measurement to characterize the time domain response was carried out. The wide bandwidth of the sensor enables tracking of a sudden drop in pressure of 30 psi in the pressure chamber, simulating a tire blowout condition, as illustrated in the Figure 4.14

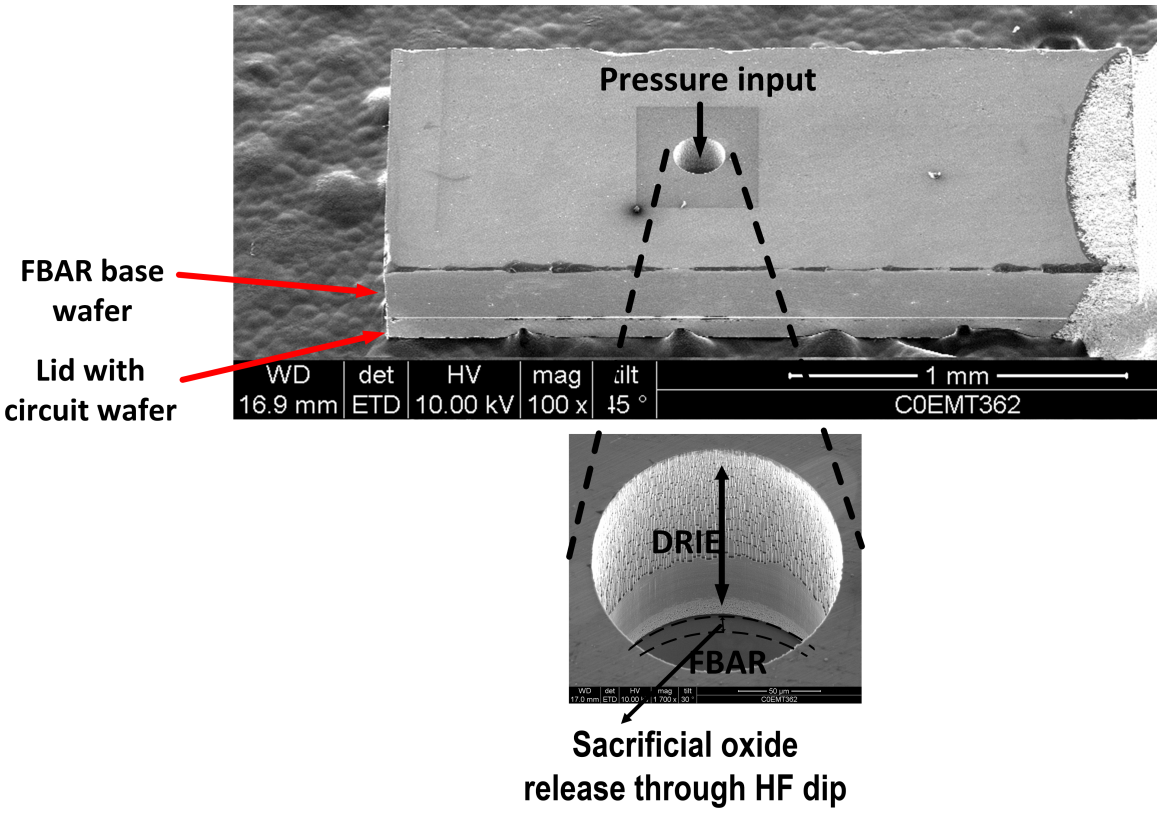

Figure 4.8: SEM image of the Pressure Sensor die showing the channel for pressure input

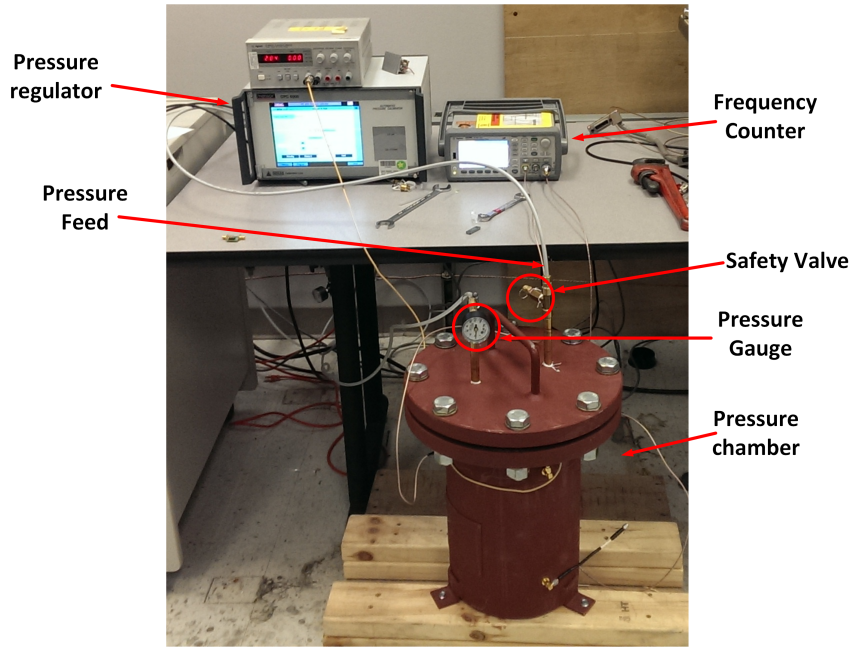

Figure 4.9: Test setup for the pressure sensor characterization

The accuracy of the pressure sensor was characterized over a temperature range of −20 to 70 °C. Figure 4.15 shows the effectiveness of the differential frequency measurement technique. The reference and the sensor FBAR frequency track each other and a differential

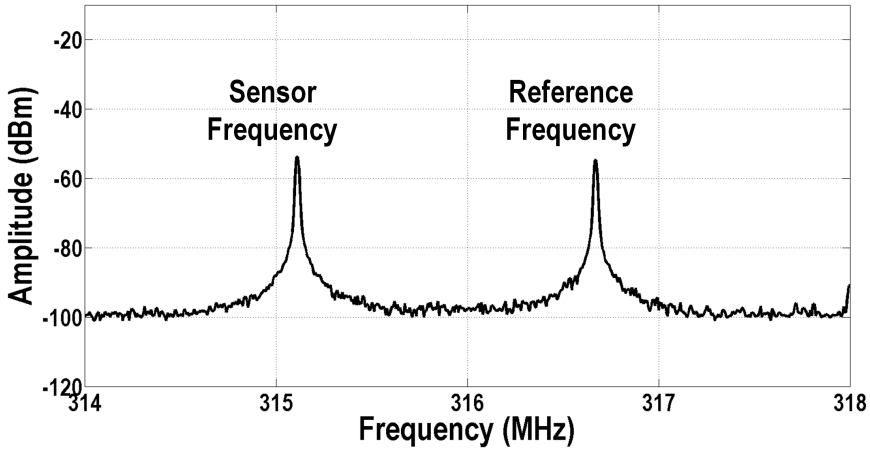

Figure 4.10: Pressure sensor output monitored on Spectrum Analyzer

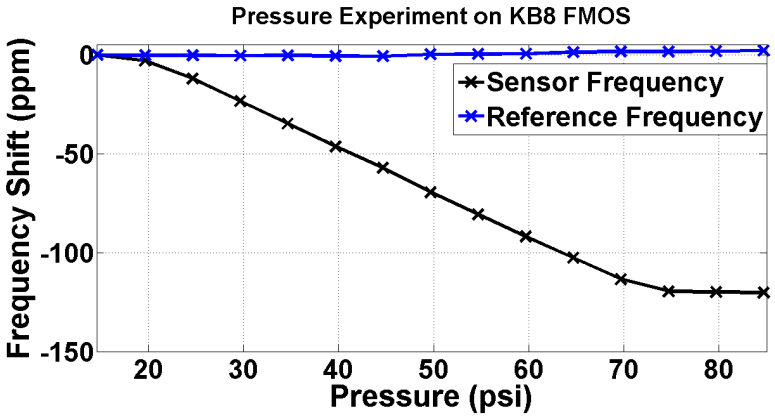

Figure 4.11: FBAR frequency shift with Pressure

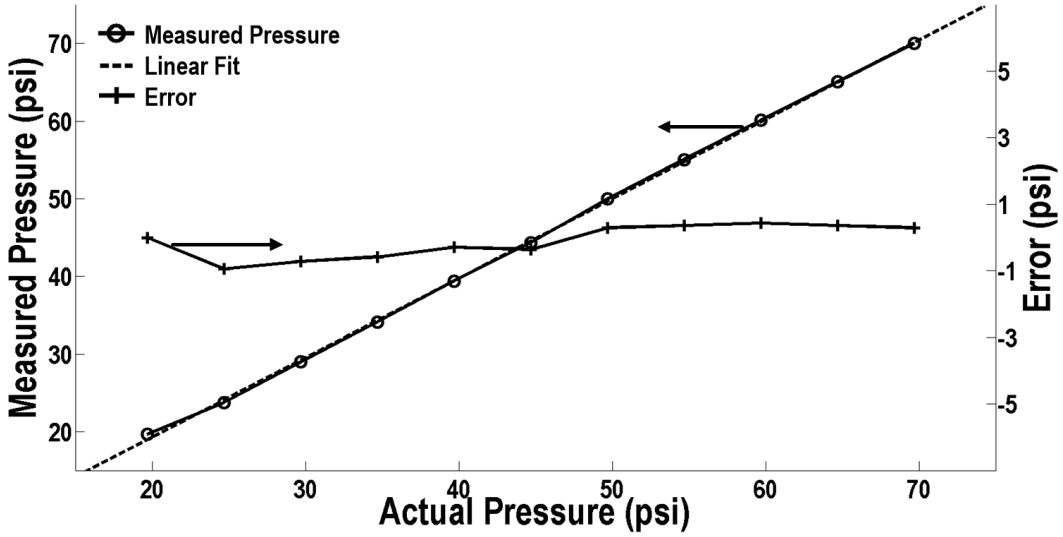

Figure 4.12: FBAR Pressure Sensor characterization

measurement results in a maximum error of 3.1 ppm. This translates to a maximum error over temperature of ±0.7 psi in the sensor output over the total 90 °C range. The effectiveness of the temperature drift cancellation was measured across multiple dies and a worst case cancellation of 5.5 ppm or a pressure uncertainty of ±1.3 psi. Table 4.1 summarizes the performance summary of the pressure sensor

The sensor performance was characterized over multiple dies. The sensitivity of the

Table 4.1: Performance Summary of the FBAR Pressure Sensor

Performance metric	Value
Process Technology	FBAR-CMOS $0.6\mu m$
Processing Comments	Integrates sensor, processing IC, timing reference and transmitter in a single hermetic die using a batch fabrication process
Sensitivity (ppm/psi)	2.2
Resolution (mpsi)	0.72
Temperature stability	$\pm$0.7psi (-20 to 70 °C), $\pm$0.59psi (70 to 125 °C)
Dynamic Range (psi)	20-70
Instantaneous power consumption (mW)	12.69
Duty-cycled power consumption (best resolution at a 10s refresh rate)	$30\mu W$

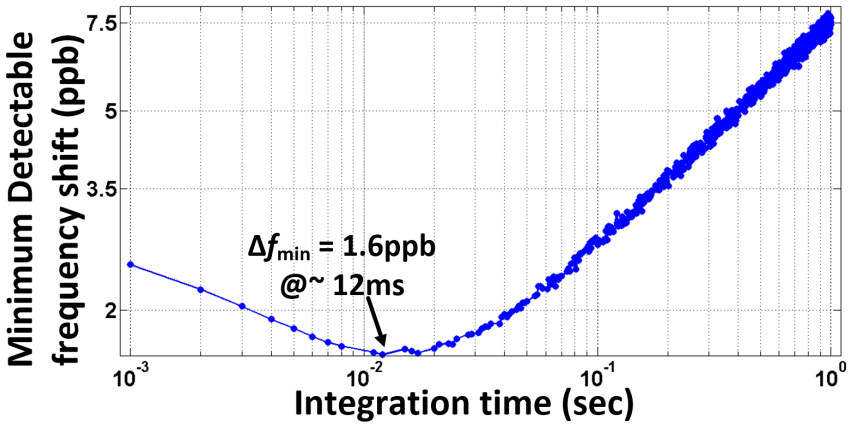

Figure 4.13: Allan Deviation Measurement of the Pressure Sensor

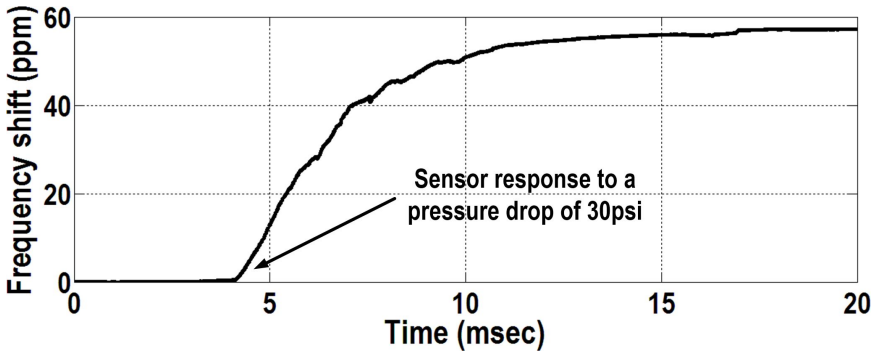

Figure 4.14: Time domain response of sensor simulating a tire blowout (pressure drop of 30 psi).

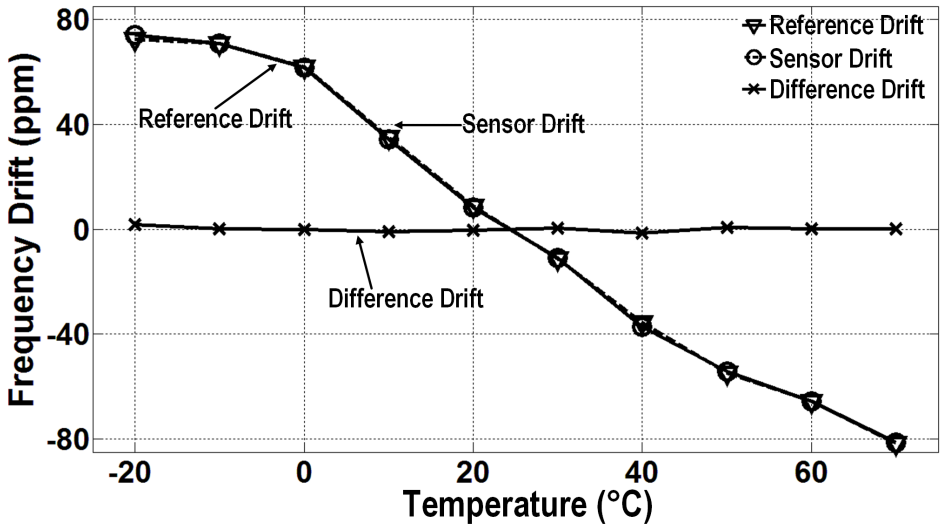

Figure 4.15: Accuracy measurement over temperature variation of 90 °C for the pressure sensor

sensor varied between 2 to 2.2ppm/psi. The common mode frequency drift cancellation depends on the perfect matching of the two FBAR's. Figure 4.16 shows the difference frequency measurement over 4 dies.

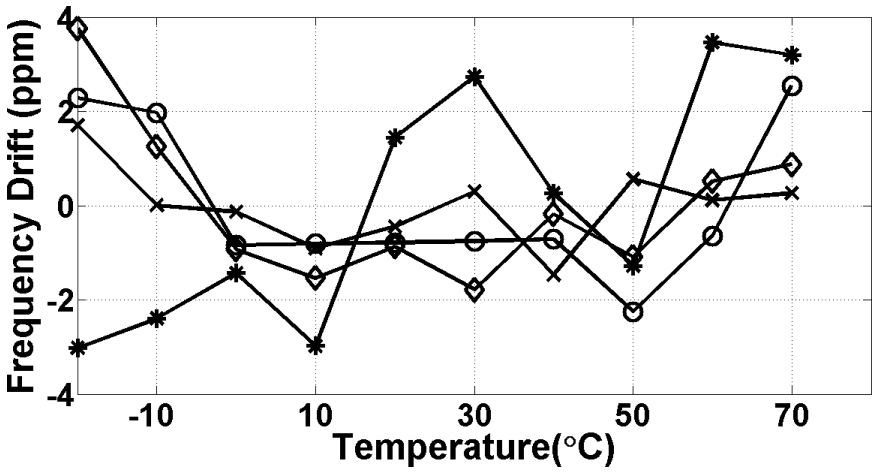

Figure 4.16: Accuracy measurement over multiple dies

4.5 Conclusion

We have demonstrated a fully integrated acoustic wave pressure sensor using FBAR as the sensing element. The sensing information is encoded in a frequency (time) domain and hence is not limited in resolution as compared to voltage output sensors. The resolution of the sensor could be further improved by increasing the native resonant frequency of the FBAR. We also propose and demonstrate a sub-mm^3 fully integrated solution with the sensor, processing IC, a frequency reference and the transmitter in a single hermetically sealed die. Table 4.2 compares the state-of-the-art pressure sensors published and available on the market. Compared to existing solutions, we demonstrate a fully integrated wireless miniaturized pressure sensor chip (for TPMS). The manufacturing process for the sensor is compatible with modern manufacturing fabs. The resolution of the sensor is 10x better compared to voltage output sensors. The system uses a 0.6μm CMOS process, but the process remains the same for any commercial CMOS process. The power consumption of the sensor could be further reduced in an advanced node.

Table 4.2: Comparison of Pressure Sensors (TPMS)

	This work	[7]	Infineon SP37[1]	[51]
Size (mm^3)	0.8	998	257	1.92
Integration Comments	Integrates sensor, processing IC, timing reference and transmitter in a single hermetic die	Sensor, processing IC , transceiver & BAW resonator are integrated through a combination of flip-chip & wire-bonding	Sensor, IC , transceiver & resonator integrated with flip-chip & wire-bonding	Piezoresistive pressure sensor with no interface circuitry
Power Consumption (10s refresh rate)	$30\mu W$	$9\mu W$	N/A	Passive
Resolution (mpsi)	0.72	No Sensor Measurement Reported	9	20
Error/Accuracy (psi)	± 0.7 (-20 to $70\,^{\circ}C$)		± 1.01 (0 to $50\,^{\circ}C$)	N/A
Range (psi)	$20 - 70$		$14.5 - 65.26$	$0 - 108$

Chapter 5

LOW POWER DIGITAL INTERFACE IC FOR FBAR SENSORS

5.1 Introduction

We have demonstrated fully-integrated FBAR-based mass and pressure sensors in the previous chapters. The idea of wafer scale integration of the sensor and interface circuitry was proposed. The sensor information was transmitted wirelessly with minimal on-chip processing to reduce the power consumption of the system. However, the instantaneous power consumption of the interface circuitry, 12.69 mW, is still prohibitively high to be used with standard coin-cell batteries or to operate entirely off harvested energy. The circuit process node used (0.6μm) limited the further reduction of the power consumption and any additional signal processing in the sensor system. Further, the architecture proposed in the previous chapter does not provide a true differential measurement of the frequencies

In this work, we demonstrate a low power digital interface IC for a FBAR based sensor system. The sensor signal is processed on-chip and a digital number representing the sensor information is transmitted out. A digital interface also benefits from scaling to advanced nodes and is easily reconfigurable.

5.2 Architecture of the FBAR Sensor Interface

The following are the design goals for the FBAR Sensor Interface IC

1. **Differential Measurement**: As illustrated in the earlier chapters, the FBAR resonant frequency is sensitive to temperature and package level stress which corrupts the frequency shift due to the sensing variable (mass and pressure). Two FBAR's in close proximity experience similar environmental conditions and a differential frequency measurement cancels the unwanted frequency drift to first order.

2. **Low Power Consumption:** A low power processing interface is desired while ex-

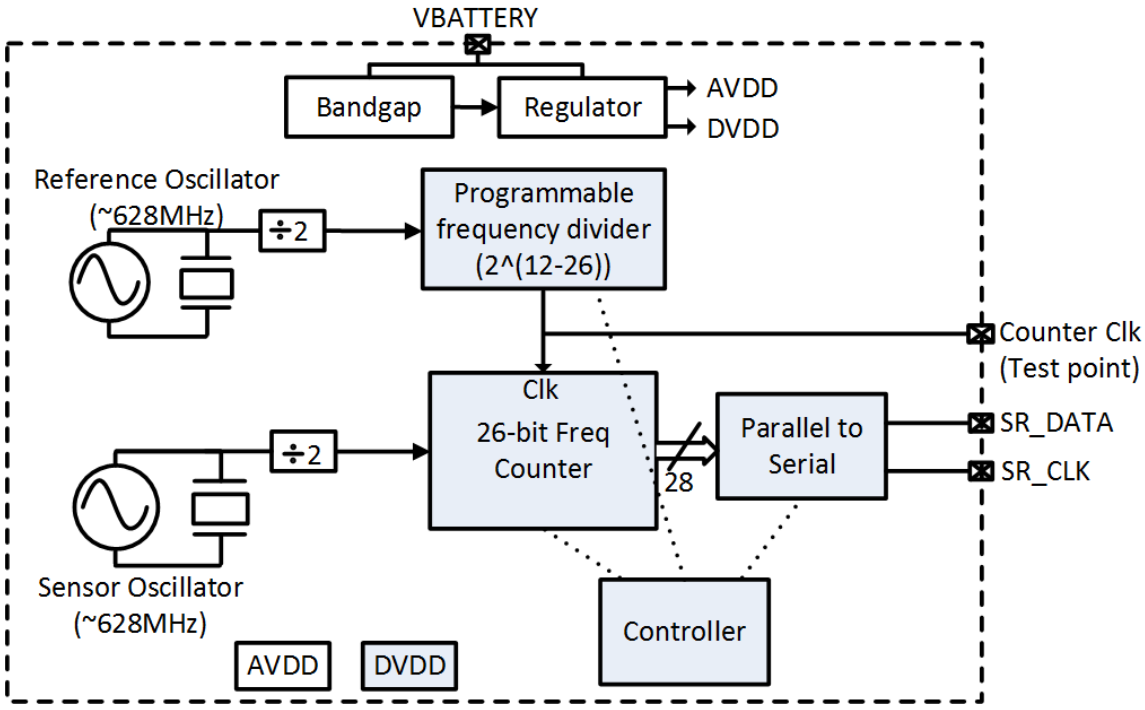

Figure 5.1: Digital Sensor Interface Architecture for FBAR Sensors

tracting the useful information from the sensor.

3. **Communication Interface:** A simple 2-wire communication interface is demonstrated to extract the useful information.

Figure 5.1 shows the architecture of the FBAR sensor interface. At the core of this architecture is the presence of a reference and a sensor FBAR to perform a differential frequency measurement and cancel out any measurement inaccuracies due to temperature, package stress etc. The two FBAR's are chosen to be 628 MHz FBAR's.

The oscillator interface with the FBAR resonator directly impacts the resolution of the sensor. The FBAR resonant frequency is monitored with a pierce oscillator structure as shown in the Figure 4.6. The design goal of the oscillator is to reduce the integrated jitter to improve the sensitivity of the sensor. The far-off phase noise in an FBAR-based sensor is not a concern due to the high-Q of the resonator and the relatively long sampling time

in a sensor measurement of the order of ms. However, close-in phase noise performance dominates the total integrated noise in the system and sets the resolution of the sensor. AM-PM (amplitude modulation to phase modulation) conversion arising from non-linear device parasitic dominates the close-in phase noise generation in an FBAR oscillator. A non-linear compensation capacitor was added to reduce the close-in phase noise [44].

Frequency Estimation: The sensor oscillator frequency is estimated using counter based logic. The number of edges in the sensor oscillator is counted for a fixed duration. This duration is defined by counting a set number of edges from the reference oscillator. Any common mode change results in a drift of both the sensor and the reference oscillator. The output of the counter thus remains constant. However, a differential input resulting from a sensor variable (mass or pressure) change affects only the sensor oscillator and changes the counter output. Thus a change in the output of the counter directly provides the sensor response.

The measurement window for the counting operation is fully programmable through a serial interface. The integration time trades power consumption (active duty cycle) for the minimum noise (hence resolution) in the measurement of the sensor. Typically, integration time for minimum Allan deviation is in the range of $10 - 100$ ms for FBAR oscillators. The start-up time of a FBAR oscillator ($10\mu s$) is negligible compared to the time required for minimum Allan deviation. The counting operation is run for 1/2 cycle of the counter (reference) clock and the counter output is transmitted serially for the other 1/2 cycle of the reference clock. A sync-code (EB90) is used at the beginning of the serial transmission for synchronization at the receiver.

Counting operation: The differential frequency measurement translates to a multiple clock domain operation. A signal crossing a clock domain, appears to the circuitry in the new clock domain as an asynchronous signal. This results in a metastable state in the first storage element (flip-flop) in the new clock domain. Systems with multiple clock domains handle this with specialized synchronization circuits that greatly increases the power consumption of the system [2]. In the proposed sensor system, the total duty-cycled power consumption is of the order of a few μW.

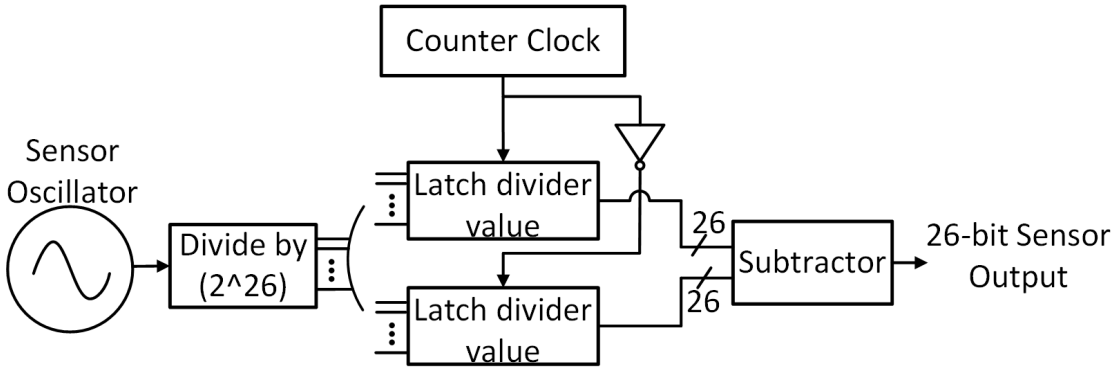

Figure 5.2: Operation of the Digital Counting Scheme

An asynchronous counting scheme is employed to save power without synchronizing the two clocks. The sensor oscillator is followed by a chain of dividers (divide by 2) and the output of the dividers is latched as a count value at the positive and negative edge of the divided reference clock. The difference between the latched counts provides an estimate of the number of edges in the given time period from which the sensor frequency could be estimated. Figure 5.2 shows the block diagram of the counting operation. The design of the first divider is critical since the input frequency is high (628MHz). A True Single Phase Clock (TSPC) flip flop based divider which incorporates high speed and low power consumption is used for the first divider. The power consumption of the subsequent dividers is negligible and standard static CMOS based circuits are used.

Quantization Error: A digital counting scheme inherently results in a quantization error in the frequency measurement. The division ratio or the counting period dictates the quantization error. The minimum quantization error with a modulo-N programmable frequency divider in the current architecture is given by equation 5.1. For a 628MHz FBAR, a divide ratio of 2^{26} translates to a resolution of 0.05ppm with a 53ms interval between successive measurements. The resolution is limited by the divide ratio rather than by the minimum noise (Allan deviation based noise) from the oscillator in the proposed system

$$Q_e = \frac{f_{sensor}}{2^{N-1}} \tag{5.1}$$

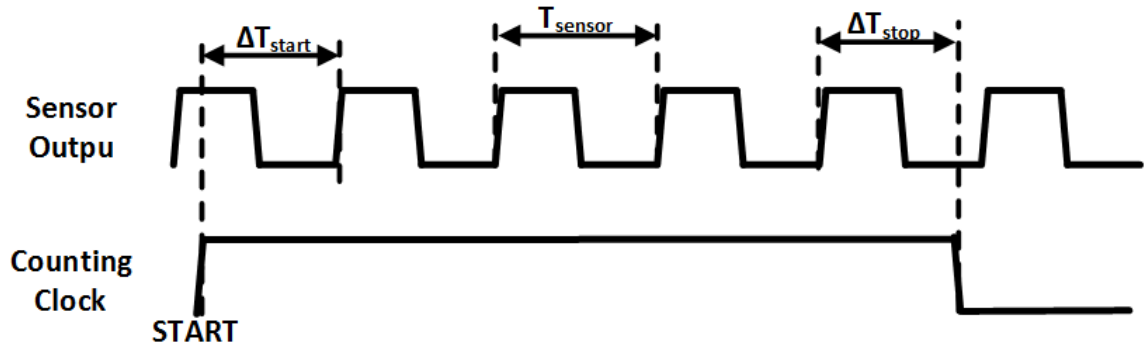

Figure 5.3: Illustration of the quantization error

5.3 Experimental Results

The proposed sensor interface architecture was fabricated in a IBM 130nm CMOS process. A dual FBAR pressure sensor was fabricated and wire bonded to the interface IC. The pressure sensor was processed as outlined in chapter 4 without the lid circuitry. Figure 5.4 shows the CMOS chip wire bonded to the FBAR sensor resonator.

Figure 5.5 shows the serial output from the sensor interface IC. The serial output data consists of a 16-bit frame sync code $EB90$ after which a 29-bit digital value representation of the sensor frequency is transmitted. The clock for the serial transmission is set to 50 times that of the counting clock. The serial data was then processed on a FPGA to extract the digital output code from the sensor. The sensor interface IC consumes $530\mu A$ from a 0.75V supply with the digital processing consuming 120μA. For one cycle of measurement and transmission (100ms), with a duty cycle ratio of 1%, the average power consumption of the IC is 4μW.

Pressure sensor response: The response of the pressure sensor was characterized by mounting the chip on a measurement PCB. The PCB was placed in a pressure chamber controlled by a pressure regulator. Figure 5.6 shows the digital output code as the pressure inside was increased. The programmable divider was programmed for a counting clock frequency of close to 10Hz.

The digital output code was then mapped to pressure values using the slope of the

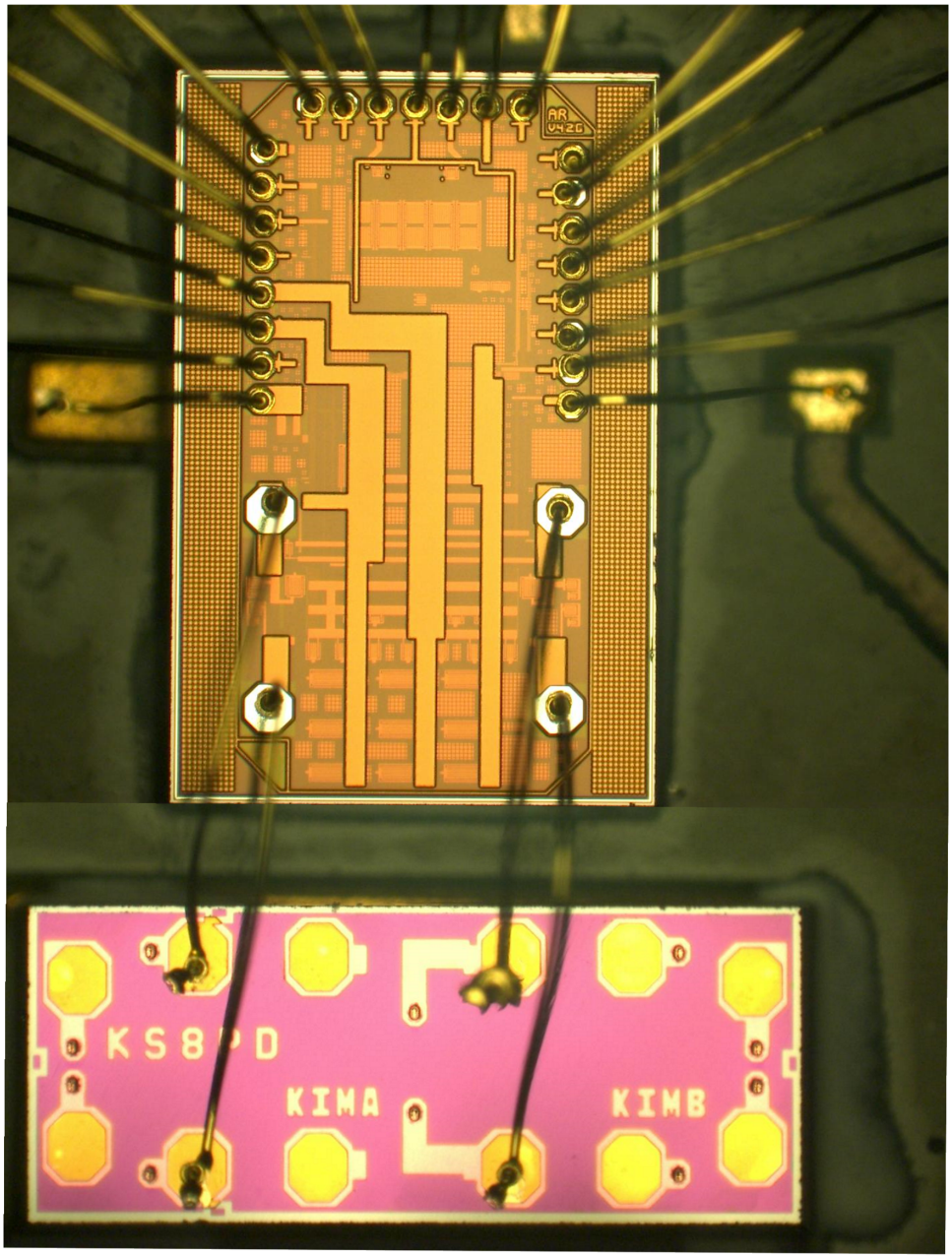

Figure 5.4: Die photo of the digital sensor interface

transfer function. Figure 5.7 shows the measured pressure as a function of the pressure input. The maximum error in the pressure measurement is 1.06 psi.

Resolution: The resolution of a FBAR sensor is determined by the minimum detectable

Figure 5.5: Serial output from the digital sensor interface

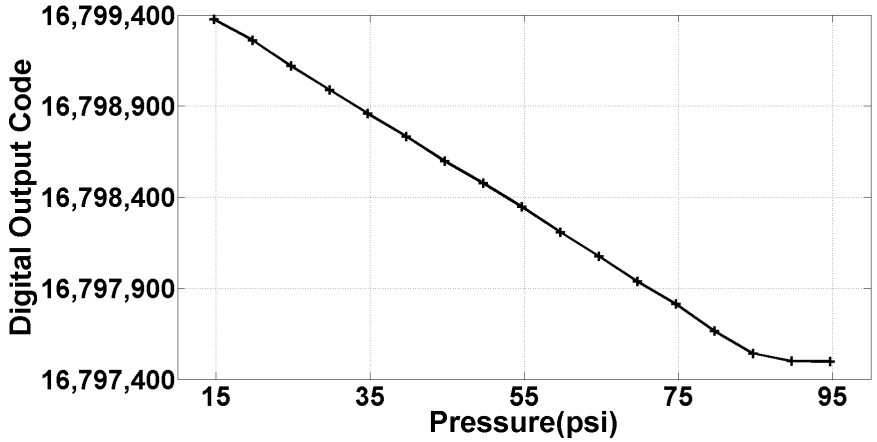

Figure 5.6: Transfer function (digital code vs pressure input) for the sensor interface IC

frequency shift, which is specified by an Allan deviation measurement. Figure 5.8 shows the Allan deviation measurement. The minimum detectable frequency shift is 3.9ppb at an integration time of 100ms. However, the quantization error also limits the resolution in the proposed digital sensor interface. With a maximum divide ratio of 2^{26} and a 628MHz FBAR, the minimum achievable resolution is 60ppb. This translates to a resolution of 0.037psi and sets the minimum resolution in the sensor system.

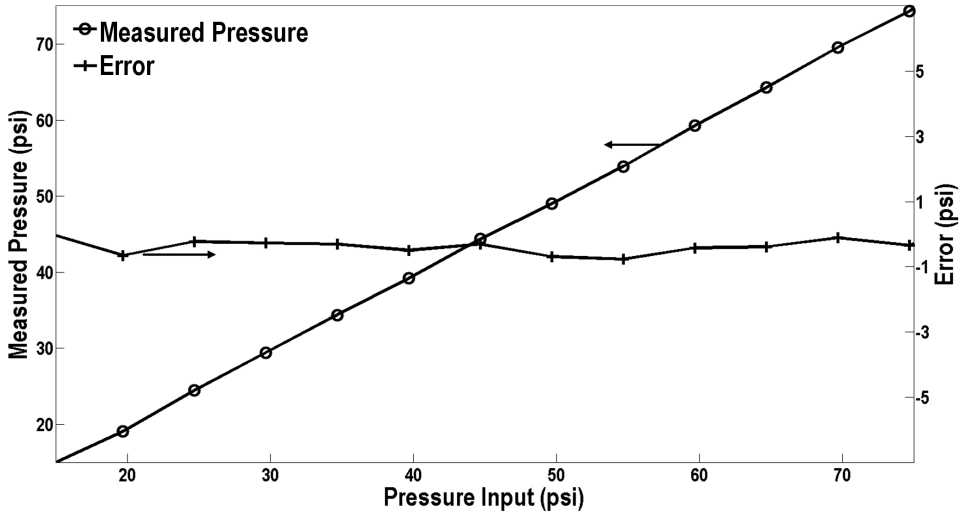

Figure 5.7: Pressure sensor calibration curve from 20 to 80 psi

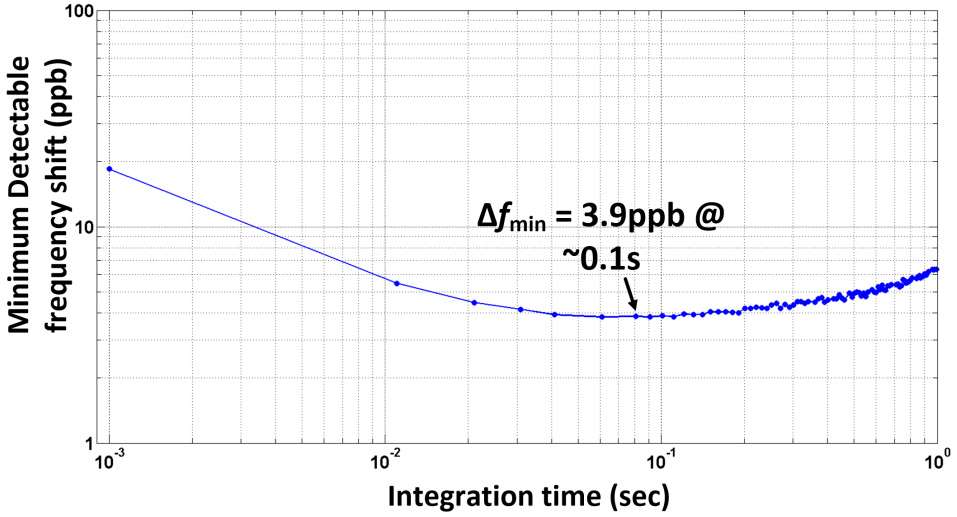

Figure 5.8: Allan Deviation measurement from the 130nm FBAR Sensor interface

Accuracy: The accuracy of the pressure sensor interface IC was characterized over a temperature range of -20 to $80\,^{\circ}$C. Figure 5.9 shows the digital output code as a function of temperature. The reference and the sensor FBAR track each other and hence the resulting change in the output code is a maximum of 160. This translates to a frequency measurement error of 6.5ppm or an accuracy of $\pm$2.08psi for the pressure measurement. Table 5.1

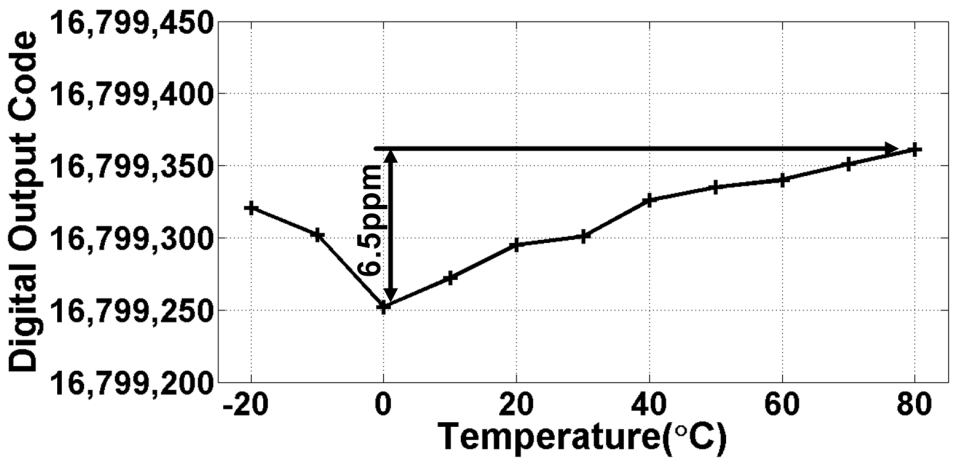

Figure 5.9: Accuracy measurement over temperature variation of -20 to $80\,^{\circ}$C for the pressure sensor

Table 5.1: Performance Summary of the Digital Sensor Interface for a pressure sensor

Performance metric	Value
Process Technology	FBAR-CMOS 130nm
Processing Comments	FBAR wire bonded to a CMOS die
Supply Voltage	0.75V
Power Consumption	$400\mu W$
Power Consumption (best resolution at a 10s refresh rate)	$4\mu W$
Sensitivity (ppm/psi)	1.6
Resolution (psi)	0.037
Temperature stability	$\pm$2.08psi (-20 to $80\,^{\circ}$C)
Dynamic Range (psi)	15-85

summarizes the performance summary of the sensor.

5.4 Conclusion

This chapter demonstrated a low power digital interface circuit for operation with FBAR-based sensors. The instantaneous current consumption of the interface circuit is 530μA and operates off a 0.75V supply. The low supply voltage and the low instantaneous power consumption makes it feasible to operate the system with standard coin-cell batteries. The architecture is scalable to advanced process nodes and will benefit from process scaling. The digital output from the sensor interface IC is compatible for further digital signal processing.

Chapter 6

A 3.75% TUNING RANGE WIDEBAND FBAR OSCILLATOR

FBAR-based oscillators have drawn significant attention since their first demonstration in [32]. They offer a high quality factor in a small form factor providing new applications in wireless sensor nodes [30][7] and offer a compelling alternative to replace quartz as the frequency reference. FBAR-based VCO's have also been attempted to demonstrate low-power and low noise RF frequency synthesizers[18] useful for applications in high performance ADC's, high speed serial data links, and low power radios. Direct-modulation transmitters using FBAR's provide a very attractive solution for low-power, small form factor transmitter in a wireless sensor [6]. However, FBAR oscillators have a notoriously poor tuning range, typically less than 0.7% [17] limiting their use as VCO in wireless and spread spectrum applications.

In contrast, LC oscillators can be tuned over a frequency range in excess of 20%. Hence, LC oscillators are commonly used in commercial applications to cover the entire tuning range of common wireless standards. However, due to the low-Q of LC oscillators, the phase noise is worse compared to FBAR oscillators. Typically, the tuning range required for many government mandated frequency bands is between $3-3.5\%$, necessitating a tradeoff between FBAR and LC oscillators. In this chapter, we propose a wide-tuning range FBAR-based oscillator suitable for VCO applications.

6.1 Understanding tuning range of FBAR

The resonance condition in the FBAR is based on exchange of acoustic and electrical energy. The voltage across the FBAR induces acoustic waves in the bulk of the resonator, which in turn induces an electric field, creating a resonant condition at one frequency. This behavior can be modeled by the Modified Butterworth-Van Dyke (mBVD) model, which is useful in circuit design. Figure 6.1 shows the mBVD model of an FBAR. C_m, L_m and R_m

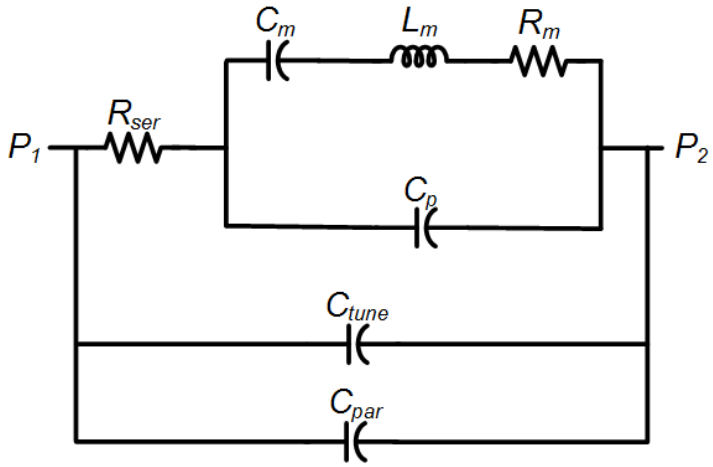

Figure 6.1: mBVD model for the FBAR resonator

represent the motional impedances, C_p represents the parallel plate capacitance between the two electrodes, and R_{ser} represents the serial resistance of the electrodes. The resonant frequency is tuned by a shunt capacitor, C_{tune} across the FBAR. C_{par} represents the parasitic capacitance across the FBAR arising from the interconnect and the oscillator circuit.

The tuning range of an FBAR is limited by the piezoelectric couping coefficient, K_t^2 of the piezoelectric material which defines the frequency separation between the series (f_s) and the parallel (f_p) resonant frequency of the FBAR. The frequency tuning sensitivity of an FBAR is given by equation 6.1, indicating it falls quadratically with C_{tune}. The frequency tuning sensitivity of an FBAR is over 100× less sensitive to capacitive tuning compared to an LC tank. Careful design to minimize the initial capacitive loading maximizes the available tuning range and a 0.7% tuning range has been demonstrated for a FBAR oscillator [17]. Most government mandated frequency bands require a tuning range in excess of 3.5%

$$\frac{\delta f_p}{\delta C_{tune}} = -\frac{f_s}{2}\frac{C_m}{C_p + {C_{tune}}^2} \tag{6.1}$$

Reducing the C_p by the addition of a negative capacitance [50] or indirect phase tuning by adding a series resistance [28], increases the tuning range. However, this degrades the 'Q' of the FBAR, which increases the phase noise and also results in a frequency dependent

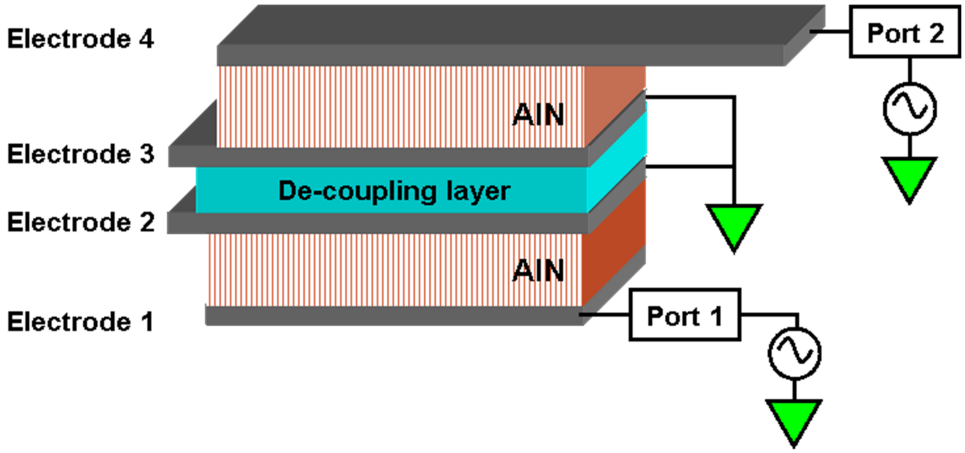

Figure 6.2: Cross-section of the Coupled FBAR Filter

phase noise performance. In this work, we propose to increase the tuning range of FBAR oscillators without significantly reducing the 'Q' of the resonator.

6.2 Coupled FBAR Resonator

Magnetically coupling multiple LC tanks offers large improvements in the tuning range of LC oscillators [43]. In this work, we extend this technique to acoustically couple FBAR resonators to enhance tuning range. Figure 6.2 shows the cross-section of a Coupled FBAR Filter (CRF). The CRF comprises of two stacked FBAR resonators, separated by a low impedance, quarter wave acoustic de-coupling medium. A single layer of the dielectric material, SiOCH, is tailored to exhibit the low acoustic impedance needed. The coupled FBAR filter exhibits a low-loss wide frequency region, enabling the design of a wide tuning range oscillator.

The CRF is suspended above an air cavity etched into the Si substrate, similar to an FBAR. In Figure 6.2, the bottom resonator consists of Electrode 1, the first Aluminum Nitride (AlN) piezoelectric layer, and Electrode 2. The top resonator is nearly identical to the bottom, and is composed of Electrode 3, a second AlN layer, and Electrode 4. Molybdenum (Mo) electrodes are employed throughout. The de-coupling layer is situated directly between Electrodes 2 and 3 and provides the impedance discontinuity needed to

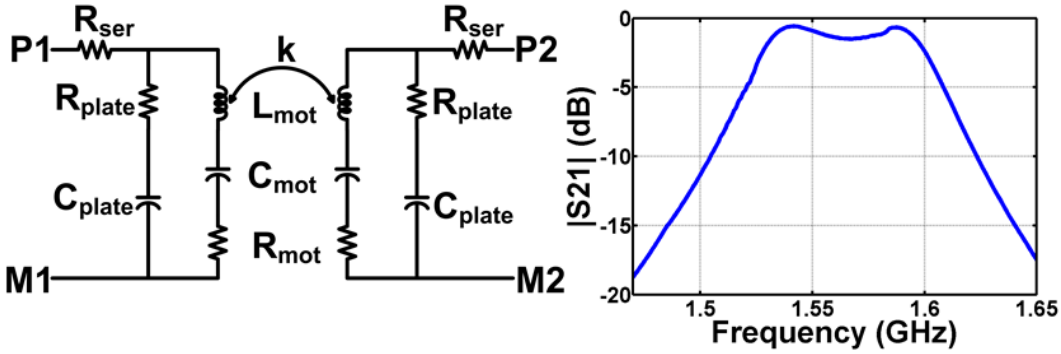

Figure 6.3: mBVD model of the CRF with the $|S21|$ characteristic

tune the coupling between the top and bottom resonators.

The CRF stack used in this work provides a 2dB bandwidth of 3.5%. The 2dB loss in the resonator is compensated by adding a gain element from the circuit. The tuning bandwidth is determined by the separation between the even and odd modes of the CRF. This bandwidth can be increased by changing the strength of the coupling, i.e increasing the impedance of the de-coupling layer. However, this would increase the insertion loss in the center of the pass band. The topology shown represents a single-ended to single-ended two port filter. After hermetically sealing the filter within a wafer level chipscale package, the die has an area of $0.54 * 0.5\text{mm}^2$ and a height of 0.2mm.

6.3 mBVD model of Coupled FBAR Resonator

To facilitate the co-design of the CRF and RFICs, we introduce an electrical equivalent model of the CRF shown in Figure 6.3. Each subsection of the model represents the Modified Butterworth-Van Dyke (MBVD) model of an FBAR proposed in [1]. Additionally, this model utilizes inductive coupling that accurately captures the acoustic coupling of the two FBAR devices. Measured S-parameters from the CRF (Figure 6.3) filter were fit to the model, providing less than 0.4 dB error in $|S21|$ compared to the measured results. The model is highly useful for the design and simulation of CRF-based RFICs.

6.4 Coupled-FBAR Oscillator Design

LC oscillators use the high impedance of a tank circuit as the load for the active element to achieve a greater than unity gain. Hence a parallel oscillator structure is a natural choice for an on-chip LC resonant tank. However, a CRF has a wide bandwidth low-loss $|S21|$ characteristic. This necessitates a series oscillator topology where the resonator is driven with a voltage and a current is sensed. The conceptual block diagram of the proposed series oscillator is shown in Figure 6.4. The coupled FBAR filter (CRF) is matched to a common gate amplifier, which injects RF current from the filter into a high impedance on-chip LC tank (phase shifter). The resulting phase-shifted signal is applied to a source follower driver amplifier (also matched to the filter) thus completing the positive feedback loop. The total gain around the loop is given by:

$$G(s) = \frac{(g_{m1} * Z_l) * S21}{2} \tag{6.2}$$

The wideband characteristic of the CRF device is maintained if it is terminated with the characteristic impedance of the device, in this case 50Ω. A common-gate amplifier is used to match to the 50Ω impedance of the coupled FBAR filter. The input impedance of the common-gate amplifier is given by:

$$Z_{in} = \frac{1}{g_{m1} + g_{mb1}} + \frac{Z_L}{(g_{m1} + g_{mb1}) * (g_{m2} + g_{mb2}) * r_{ds2} r_{ds2}} \tag{6.3}$$

The bias current determines the g_m and hence the input impedance of the common gate amplifier. A cascode structure provides isolation from load and maintains the input impedance at 50Ω. Figure 6.5 shows the schematic of the oscillator.

Tuning of the oscillator is accomplished by changing the phase of the signal around the loop. The CRF provides a 0° phase shift at the center frequency and a finite phase shift at delta values around this frequency (Figure 6.6). A phase shifter which cancels this phase shift enables to satisfy the oscillation condition at the delta frequencies, thus allowing tuning of the oscillation frequency across the passband of the filter. A external phase shifting circuit would result in attenuation of the signal in the loop [3]. However, in the proposed oscillator topology, the on-chip resonant load of the common-gate acts as a

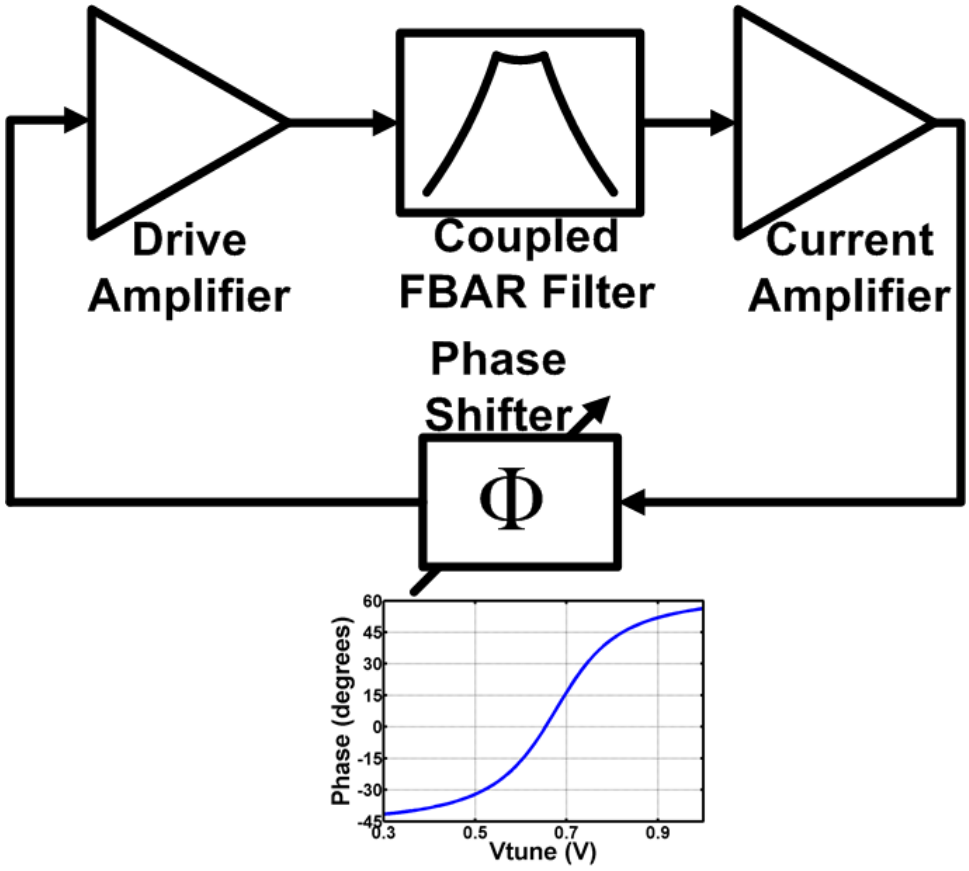

Figure 6.4: Conceptual block diagram of the Series Oscillator.

wide-tuning, fully integrated LC phase shifter and thus eliminates the need for a separate phase shifting circuit. The LC phase shifter allows a ±45° phase shift. By tuning the LC tank, the oscillator is tuned to different frequencies, resulting in simple control of the oscillation frequency. The total phase change ($\frac{d\phi}{d\omega}$) around the loop is now given by

$$\frac{d\phi}{dw} = \frac{d\phi_{crf}}{dw} + \frac{d\phi_{circuit}}{dw} \tag{6.4}$$

$$Q = \frac{w_o}{2}|\frac{d\phi}{dw}| \tag{6.5}$$

The $\frac{d\phi_{crf}}{dw}$ term dominates in equation 6.4 and determines the Q of the oscillator resulting in a good phase noise performance. A source follower is essential to prevent loading of the

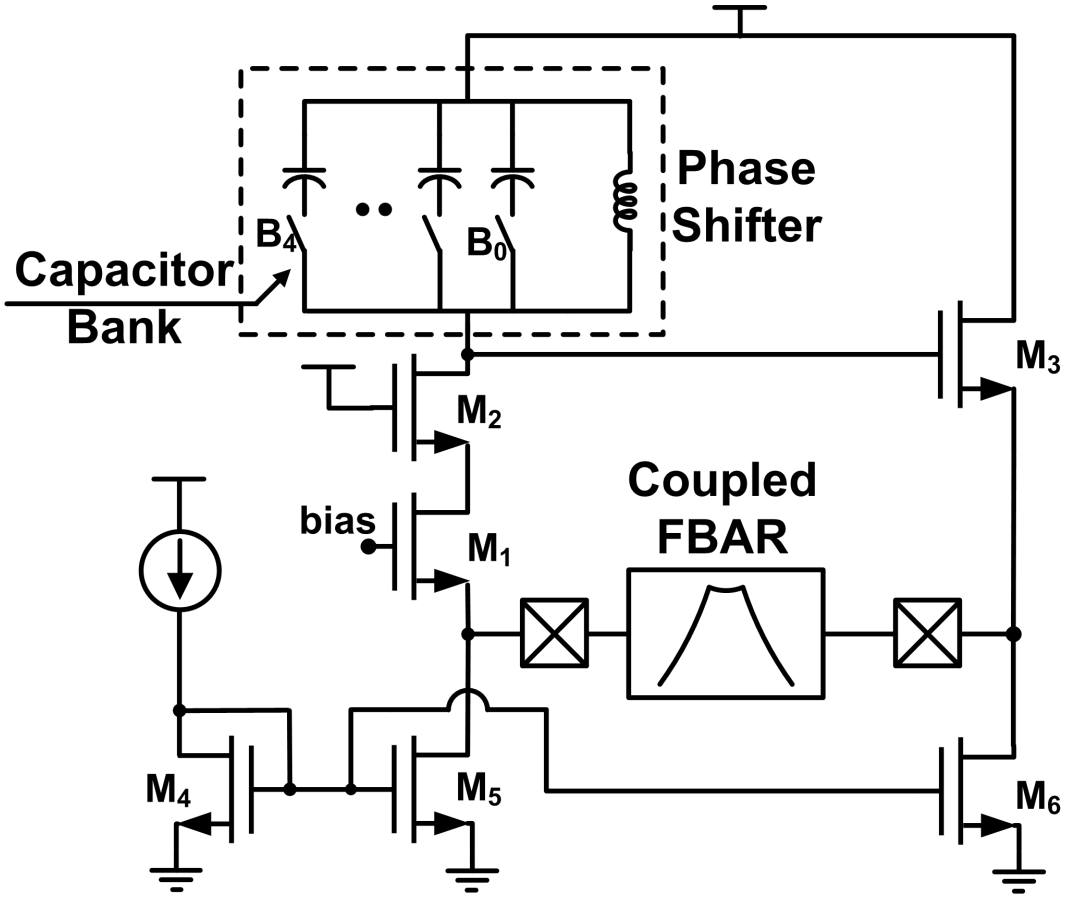

Figure 6.5: Circuit Diagram of the CRF based Oscillator.

tank by the 50Ω input impedance of the CRF.

6.5 Measured Results

The series oscillator circuit was fabricated in a 0.13μm CMOS process. The coupled FBAR filter was wirebonded to the chip (Figure 6.7). As a control experiment, the same circuit was assembled with a DC blocking capacitor in place of the coupled filter, creating an LC oscillator. Both oscillators consume 9.75mA from a 1.1V supply.

Fig. 6.8 shows the output spectrum of the coupled FBAR oscillator overlaid on the spectrum of the LC oscillator, showing a significantly cleaner spectrum. A tuning range of 43.3MHz (1.569 GHz to 1.613 GHz) was achieved in the analog varactor tuned version of

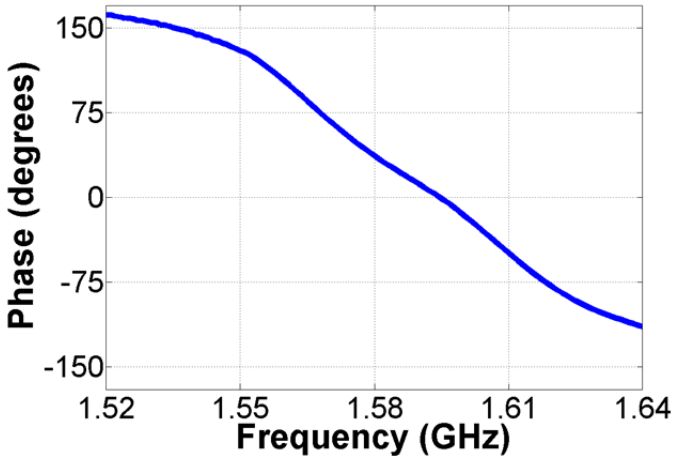

Figure 6.6: Phase characteristics of the CRF.

the oscillator. The digital varactor based version demonstrated a tuning range of 56MHz (1.527 GHz to 1.583 GHz) or 3.75% as illustrated in Figure 6.9.

A best-case phase noise of -144.35dBc/Hz at an offset of 1 MHz is measured as illustrated in Figure 6.10. In comparison, the LC oscillator achieved a phase noise of -110.7dBc/Hz @1MHz offset with the same power consumption. This clearly shows the dominating characteristics of the high Q coupled FBAR in the oscillator loop response. The VCO provides a phase noise between -144.35dBc/Hz and -135.7dBc/Hz across the entire tuning range (at an offset of 1MHz) as illustrated in the phase noise vs frequency curve in Figure 6.11.

In order to compare VCOs, the Figure of Merit (FOM) below is used [37]. Here $L(\Delta f)$ is the phase noise, f_o is the operating frequency, Δf is the offset frequency, and P_{dc} is the power dissipation.

$$FOM = L(\Delta f) - 20 * log(\frac{f_o}{\Delta f}) + 10 * log(\frac{P_{dc}}{1mW}) \tag{6.6}$$

The oscillator achieves an FOM of -197.5dB with a tuning range of $37,500$ ppm. A comparison with recently-published FBAR and LC VCOs [28][50][55][24][13] is given in Table. 6.1. The proposed oscillator achieves the best phase noise over the entire tuning range compared to previously published 'de-Q'ed FBAR VCOs [28][50] and superior tuning

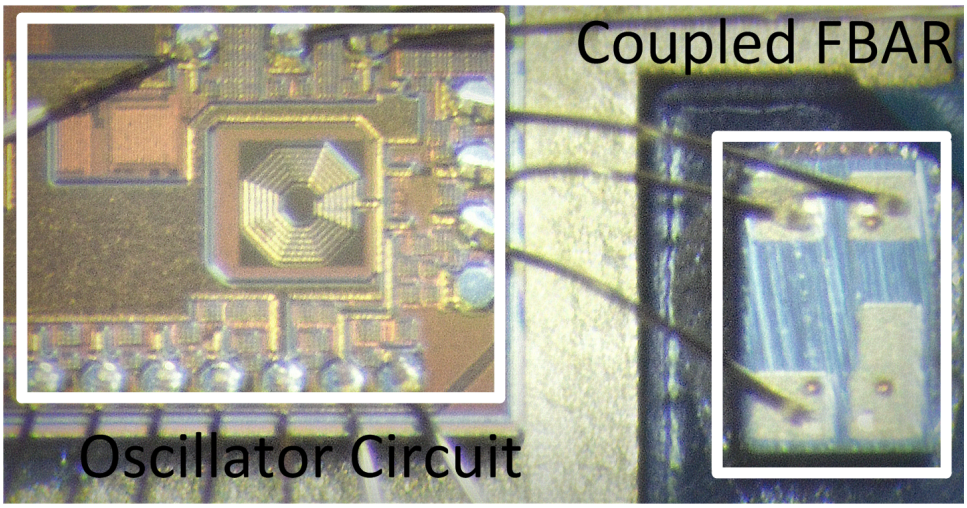

Figure 6.7: Chip micrograph of the coupled FBAR oscillator.

range compared to high performance FBAR VCOs [37][17][55].

6.6 Conclusion

This work presents the first IC oscillator using coupled FBARs. The measured tuning range of 3.75% is sufficient for ISM band applications. The phase noise performance is superior to on-chip LC oscillators and presents a compelling alternative in the design of high-performance VCO's.

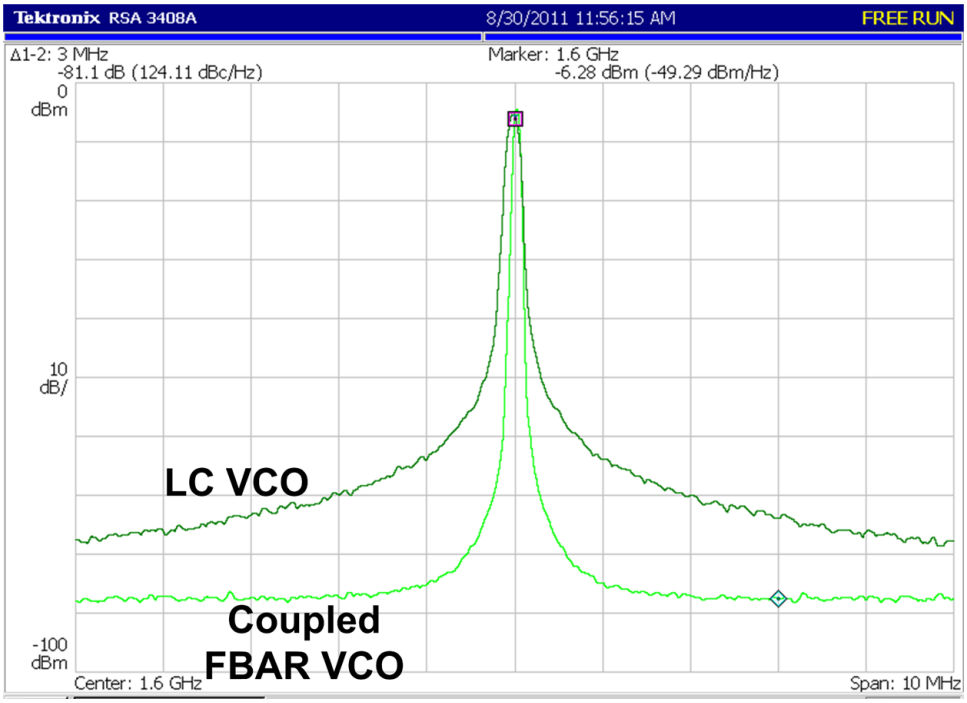

Figure 6.8: Output spectrum of the coupled FBAR and a LC VCO.

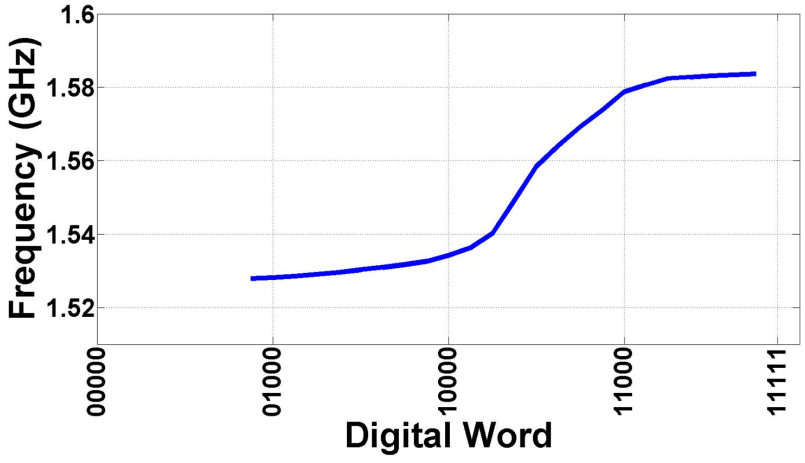

Figure 6.9: Tuning Curve of the coupled FBAR oscillator.

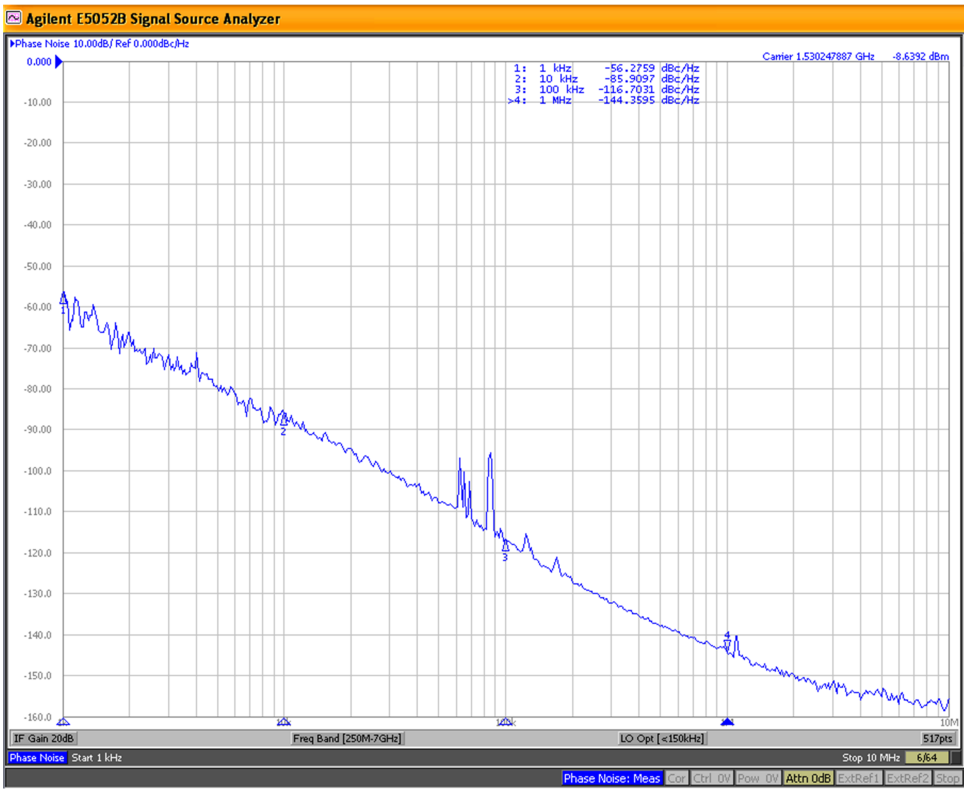

Figure 6.10: Phase noise performance of the coupled FBAR oscillator.

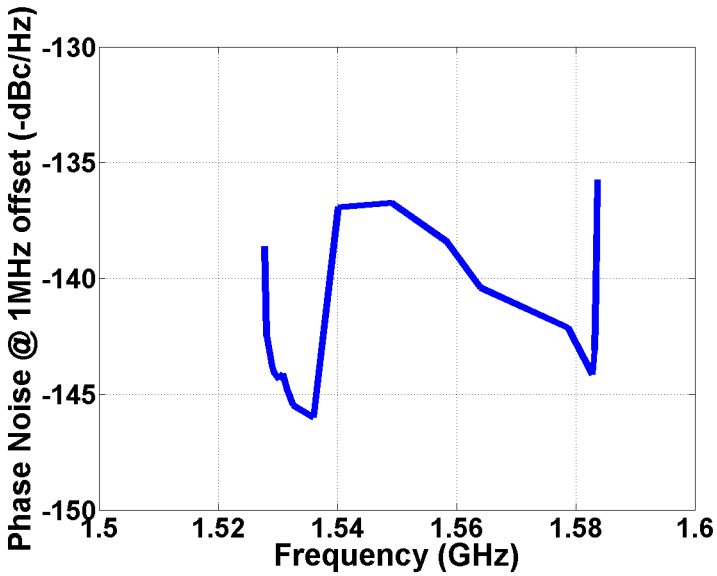

Figure 6.11: Phase noise performance across the entire tuning range of the coupled FBAR oscillator.

Table 6.1: Performance summary and comparison of Wideband Oscillators

	Center freq. (GHz)	Tech. Node	Power (mW)	Tuning Range (ppm)	Best case Phase Noise (1MHz offset) (-dBc/Hz)	Phase Noise (1MHz offset) across the tuning range (-dBc/Hz)	FOM (dB)
[37]	2.1	0.13μm CMOS BAW I/Q VCO	0.6	715	-143.5	constant	-212.1
[28]	2.2	0.25μm BiCMOS BAW VCO	58.32	18000	-144	-122 to -144	-192.7
[50]	2.1	0.13μm CMOS BAW VCO	6	100,000	-135.7	Not reported	-194.7
[55]	1.7	Bipolar BAW VCO	4.95	<1000	-149.9	constant	-207
[17]	1.5	0.18μm CMOS BAW VCO	4	7000	-142	constant	-199.5
[24]	5	0.13μm CMOS LC VCO	1.4	172,000	-130 @ 3MHz	Not reported	-192
[13]	1.86	0.18μm CMOS LC VCO	1.6	81000	-128	Not reported	-191.3
This work	**1.55**	**0.13μm CMOS, Coupled FBAR, analog varactor**	**7.9**	**28,000**	**-140.5**	**-133.64 to -140.5**	**-195.56**
This work	**1.55**	**0.13μm CMOS, Coupled FBAR, digital cap bank**	**11.3**	**37,500**	**-144.35**	**-135.7 to -144.35**	**-197.5**

Chapter 7

CONCLUSION

Sensors have greatly revolutionized human life and are becoming ubiquitous in our everyday life. Miniaturization and cost reduction of sensor systems is an active area of research to enable new applications. This thesis illustrated the integration of the sensing element, processing circuitry, a frequency reference for communication and the communication interface in a single hermetically sealed die. This was enabled by the use of Thin Film Bulk Acoustic Wave Resonators (FBAR) as the sensing element and the frequency reference. Further, fully integrated sub-mm^3 FBAR based wireless mass and pressure sensors were demonstrated. The sensor systems have a 100x smaller form factor compared to existing state-of-the-art solutions.

The manufacturing process involved standard wafer scale fabrication IC process that greatly reduces the manufacturing cost of these sensors. Low-power circuit architectures for extracting the sensing information from a resonant frequency sensor were demonstrated.

The last part of this thesis demonstrated a wide-band FBAR-based oscillator with a tuning range of 3.75%. The phase noise performance was superior to an LC oscillator. A high Q, wide tuning voltage controlled oscillator enables design of high performance, low power transceivers.

In summary, the main contributions of this work are listed below:

1. The idea of fully integrated sub-mm^3 sensors using wafer-scale integration techniques is highlighted.

2. A fully integrated 0.34mm^3 fully integrated mass sensor suitable for a wide variety of chemical and biological applications was demonstrated.

3. An FBAR based pressure sensor was proposed and a 0.8mm^3 fully integrated wireless pressure sensor was demonstrated

4. A low power digital architecture suitable for resonant frequency based sensors was implemented and its usefulness in a FBAR based pressure sensor was illustrated

5. A low-noise 1.5GHz VCO with a 3.75% tuning range using Coupled FBAR filters was illustrated.

Miniaturized low-cost sensors have far reaching implications in solving global issues like reduction of global warming, development of clean water, reduced medical care cost to name a few [48]. Hence there needs to be a concerted effort to meet the growing demand for sensors which is expected to reach trillions in the next decade. Such high demand requires low-cost, mass producible sensing technologies as illustrated in this thesis.

BIBLIOGRAPHY

[1] Infineon Technologies AG. Infineon Technologies, SP37 datasheet. `http://www.infineon.com/cms/en/product/sensor-ics/tire-pressure-sensors/channel.html?channel=ff80808112ab681d0112ab69078700d8`, 2015.

[2] R.W. Apperson, Zhiyi Yu, M.J. Meeuwsen, T. Mohsenin, and B.M. Baas. A Scalable Dual-Clock FIFO for Data Transfers Between Arbitrary and Haltable Clock Domains. *Very Large Scale Integration (VLSI) Systems, IEEE Transactions on*, 15(10):1125–1134, Oct 2007.

[3] Ivan D Avramov, Stephen R Gilbert, and Rich Ruby. 1.5-GHz voltage controlled oscillator with 3% tuning bandwidth using a two-pole DSBAR filter. *Ultrasonics, Ferroelectrics and Frequency Control, IEEE Transactions on*, 58(5):916–923, 2011.

[4] FM Battiston, J-P Ramseyer, HP Lang, MK Baller, Ch Gerber, JK Gimzewski, E Meyer, and H-J Güntherodt. A chemical sensor based on a microfabricated cantilever array with simultaneous resonance-frequency and bending readout. *Sensors and Actuators B: Chemical*, 77(1):122–131, 2001.

[5] Moo Sung Chae, Zhi Yang, Mehmet R Yuce, Linh Hoang, and Wentai Liu. A 128-channel 6 mW wireless neural recording IC with spike feature extraction and UWB transmitter. *Neural Systems and Rehabilitation Engineering, IEEE Transactions on*, 17(4):312–321, 2009.

[6] Yuen Hui Chee, Ali M Niknejad, and J Rabaey. A 46% efficient 0.8 dBm transmitter for wireless sensor networks. In *VLSI Circuits, 2006. Digest of Technical Papers. 2006 Symposium on*, pages 43–44. IEEE, 2006.

[7] M. Flatscher, M. Dielacher, T. Herndl, T. Lentsch, R. Matischek, J. Prainsack, W. Pribyl, H. Theuss, and W. Weber. A Bulk Acoustic Wave (BAW) Based Transceiver

for an In-Tire-Pressure Monitoring Sensor Node. *Solid-State Circuits, IEEE Journal of*, 45(1):167–177, Jan 2010.

[8] Stephen PA Fodor. DNA sequencing: Massively parallel genomics. *Science*, 277(5324):393–395, 1997.

[9] Stephen R Gilbert, Martha Small, Reed Parker, Lori Callaghan, Steve Ortiz, Frank Bi, Lexie Kekoa, Jackie Tan, Norashaz Bin Alias, Gerald Ong, et al. Manufacturing and reliability of chip-scale packaged FBAR oscillators. In *Ultrasonics Symposium (IUS), 2014 IEEE International*, pages 89–92. IEEE, 2014.

[10] Reid R Harrison and Cameron Charles. A low-power low-noise CMOS amplifier for neural recording applications. *Solid-State Circuits, IEEE Journal of*, 38(6):958–965, 2003.

[11] Reid R Harrison, Haleh Fotowat, Raymond Chan, Ryan J Kier, Robert Olberg, Anthony Leonardo, and Fabrizio Gabbiani. Wireless neural/EMG telemetry systems for small freely moving animals. *Biomedical Circuits and Systems, IEEE Transactions on*, 5(2):103–111, 2011.

[12] Jeremy Holleman and Brian Otis. A sub-microwatt low-noise amplifier for neural recording. *IEEE engineering in medicine and biology magazine*, 1:3930, 2007.

[13] Jong-Phil Hong and Sang-Gug Lee. Low Phase Noise G $_m$-Boosted Differential Gate-to-Source Feedback Colpitts CMOS VCO. *Solid-State Circuits, IEEE Journal of*, 44(11):3079–3091, 2009.

[14] http://www.infineon.com/cms/en/product/sensor-ics/tire-pressure sensors/channel.html?channel=ff80808112ab681d0112ab69078700d8. Infineon Technologies.

[15] Changhui Hu, Rahul Khanna, Jay Nejedlo, Kangmin Hu, Huaping Liu, and Patrick Y Chiang. A 90 nm-CMOS, 500 Mbps, 3–5 GHz fully-integrated IR-UWB transceiver with multipath equalization using pulse injection-locking for receiver phase synchronization. *Solid-State Circuits, IEEE Journal of*, 46(5):1076–1088, 2011.

[16] J.R. Hu, R.C. Ruby, and B.P. Otis. A 1.5GHz 0.2psRMS jitter 1.5mW divider-less FBAR ADPLL in 65nm CMOS. In *Custom Integrated Circuits Conference (CICC), 2012 IEEE*, pages 1–4, Sept 2012.

[17] Julie Hu, R Parkery, Rich Ruby, and Brian Otis. A wide-tuning digitally controlled FBAR-based oscillator for frequency synthesis. In *Frequency Control Symposium (FCS), 2010 IEEE International*, pages 608–612. IEEE, 2010.

[18] Julie R Hu, Richard C Ruby, and Brian P Otis. A 1.5 GHz 0.2 ps RMS jitter 1.5 mW divider-less FBAR ADPLL in 65nm CMOS. In *Custom Integrated Circuits Conference (CICC), 2012 IEEE*, pages 1–4. IEEE, 2012.

[19] Farzad Inanlou, Mehdi Kiani, and Maysam Ghovanloo. A 10.2 Mbps pulse harmonic modulation based transceiver for implantable medical devices. *Solid-State Circuits, IEEE Journal of*, 46(6):1296–1306, 2011.

[20] Matthew L Johnston, Ioannis Kymissis, and Kenneth L Shepard. FBAR-CMOS oscillator array for mass-sensing applications. *Sensors Journal, IEEE*, 10(6):1042–1047, 2010.

[21] Re-Ching Lin, Ying-Chung Chen, Wei-Tsai Chang, Chien-Chuan Cheng, and Kuo-Sheng Kao. Highly sensitive mass sensor using film bulk acoustic resonator. *Sensors and Actuators A: Physical*, 147(2):425–429, 2008.

[22] Joachim Lübke and Dirk Feldmeyer. Excitatory signal flow and connectivity in a cortical column: focus on barrel cortex. *Brain Structure and Function*, 212(1):3–17, 2007.

[23] J. Marek. MEMS for automotive and consumer electronics. In *Solid-State Circuits Conference Digest of Technical Papers (ISSCC), 2010 IEEE International*, pages 9–17, San Francisco, USA, February 2010.

[24] Andrea Mazzanti and Pietro Andreani. Class-C harmonic CMOS VCOs, with a general result on phase noise. *Solid-State Circuits, IEEE Journal of*, 43(12):2716–2729, 2008.

[25] Makoto Muratsugu, Fumihiko Ohta, Yoshihiro Miya, Toshiaki Hosokawa, Shigeru Kurosawa, Naoki Kamo, and Hisami Ikeda. Quartz crystal microbalance for the detection of microgram quantities of human serum albumin: relationship between the frequency change and the mass of protein adsorbed. *Analytical chemistry*, 65(20):2933–2937, 1993.

[26] Andrew Nelson, Julie Hu, Jyrki Kaitila, Richard Ruby, and Brian Otis. A 22μW, 2.0 GHz FBAR oscillator. In *Radio Frequency Integrated Circuits Symposium (RFIC), 2011 IEEE*, pages 1–4. IEEE, 2011.

[27] Martin Nirschl, Arto Rantala, Kari Tukkiniemi, Sanna Auer, Ann-Charlotte Hellgren, Dana Pitzer, Matthias Schreiter, and Inger Vikholm-Lundin. CMOS-integrated film bulk acoustic resonators for label-free biosensing. *Sensors*, 10(5):4180–4193, 2010.

[28] Kim B Ostman, Sami T Sipila, Ivan S Uzunov, and Nikolay T Tchamov. Novel VCO architecture using series above-IC FBAR and parallel LC resonance. *Solid-State Circuits, IEEE Journal of*, 41(10):2248–2256, 2006.

[29] B. Otis, Y.H. Chee, and J. Rabaey. A 400 μW-RX, 1.6mW-TX super-regenerative transceiver for wireless sensor networks. In *Solid-State Circuits Conference, 2005. Digest of Technical Papers. ISSCC. 2005 IEEE International*, pages 396–606 Vol. 1, Feb 2005.

[30] B.P. Otis, Y.H. Chee, R. Lu, N.M. Pletcher, and J.M. Rabaey. An ultra-low power MEMS-based two-channel transceiver for wireless sensor networks. In *VLSI Circuits, 2004. Digest of Technical Papers. 2004 Symposium on*, pages 20–23, June 2004.

[31] B.P. Otis and J.M. Rabaey. A 300-μW 1.9-GHz CMOS oscillator utilizing micromachined resonators. *Solid-State Circuits, IEEE Journal of*, 38(7):1271–1274, July 2003.

[32] Brian P Otis and Jan M Rabaey. A 300-μW 1.9-GHz CMOS oscillator utilizing micromachined resonators. *Solid-State Circuits, IEEE Journal of*, 38(7):1271–1274, 2003.

[33] I. Paprotny, F. Doering, and R.M. White. MEMS Particulate Matter (PM) monitor for cellular deployment. In *Sensors, 2010 IEEE*, pages 2435–2440, Nov 2010.

[34] Rodrigo Quiroga, Zoltan Nadasdy, and Yoram Ben-Shaul. Unsupervised spike detection and sorting with wavelets and superparamagnetic clustering. *Neural computation*, 16(8):1661–1687, 2004.

[35] Shailesh Rai, Jeremy Holleman, Jagdish Nayayan Pandey, Fan Zhang, and B Otis. A 500μW neural tag with 2μV rms AFE and frequency-multiplying MICS/ISM FSK transmitter. In *Solid-State Circuits Conference-Digest of Technical Papers, 2009. ISSCC 2009. IEEE International*, pages 212–213. IEEE, 2009.

[36] Shailesh Rai and Brian Otis. A 1V 600μW 2.1 GHz Quadrature VCO Using BAW Resonators. In *Solid-State Circuits Conference, 2007. ISSCC 2007. Digest of Technical Papers. IEEE International*, pages 576–623. IEEE, 2007.

[37] Shailesh S Rai and Brian P Otis. A 600 μ W BAW-Tuned Quadrature VCO Using Source Degenerated Coupling. *Solid-State Circuits, IEEE Journal of*, 43(1):300–305, 2008.

[38] RL Rennaker, J Miller, H Tang, and DA Wilson. Minocycline increases quality and longevity of chronic neural recordings. *Journal of neural engineering*, 4(2):L1, 2007.

[39] RL Rennaker, S Street, AM Ruyle, and AM Sloan. A comparison of chronic multichannel cortical implantation techniques: manual versus mechanical insertion. *Journal of neuroscience methods*, 142(2):169–176, 2005.

[40] R.C. Ruby, A. Barfknecht, C. Han, Y. Desai, F. Geefay, G. Gan, M. Gat, and T. Verhoeven. High-Q FBAR filters in a wafer-level chip-scale package. In *Solid-State Circuits Conference, 2002. Digest of Technical Papers. ISSCC. 2002 IEEE International*, volume 2, pages 142–440, Feb 2002.

[41] Rich Ruby, Martha Small, Frank Bi, Don Lee, Lori Callaghan, Reed Parker, and Steve Ortiz. Positioning FBAR technology in the frequency and timing domain. *Ultrasonics, Ferroelectrics, and Frequency Control, IEEE Transactions on*, 59(3):334–345, 2012.

[42] Alexander Rush and Philip R Troyk. Power and data for a wireless implanted neural

recording system. In *Neural Engineering (NER), 2011 5th International IEEE/EMBS Conference on*, pages 507–510. IEEE, 2011.

[43] Zahra Safarian and Hossein Hashemi. Wideband multi-mode CMOS VCO design using coupled inductors. *Circuits and Systems I: Regular Papers, IEEE Transactions on*, 56(8):1830–1843, 2009.

[44] Kannan Sankaragomathi, Lori Callaghan, Richard Ruby, and Brian Otis. A 220dB FOM, 1.9 GHz oscillator using a phase noise reduction technique for high-Q oscillators. In *Radio Frequency Integrated Circuits Symposium (RFIC), 2013 IEEE*, pages 31–34. IEEE, 2013.

[45] Dong S Shim and David A Feld. A general nonlinear mason model of arbitrary nonlinearities in a piezoelectric film. In *Ultrasonics Symposium (IUS), 2010 IEEE*, pages 295–300. IEEE, 2010.

[46] Martha Small, Rich Ruby, Steven Ortiz, Reed Parker, Fan Zhang, Jianlei Shi, and Brian Otis. Wafer-scale packaging for FBAR-based oscillators. In *Frequency Control and the European Frequency and Time Forum (FCS), 2011 Joint Conference of the IEEE International*, pages 1–4. IEEE, 2011.

[47] JH Smith, S Montague, JJ Sniegowski, JR Murray, and PJ McWhorter. Embedded micromechanical devices for the monolithic integration of MEMS with CMOS. In *Electron Devices Meeting, 1995. IEDM'95., International*, pages 609–612. Ieee, 1995.

[48] TSensorS Summit. Sensors Summit: For Trillion Sensor Roadmap. `http://www.tsensorssummit.org/Resources/Why%20TSensors%20Roadmap.pdf`, October 2013.

[49] 49 CFR Part 571 Docket No. NHTSA 2000-8572 US Department of Transportation, National Highway Traffic Safety Administration. Federal Motor Vehicle Safety Standards; Tire Pressure Monitoring Systems; Controls and Displays.

[50] Pierre Vincent, Jean-Baptiste David, Ioan Burciu, Jérôme Prouvée, Christophe Billard, Christine Fuchs, Guy Parat, Emeric Defoucaud, and Alexandre Reinhardt. A 1V

220MHz-Tuning-Range 2.2 GHz VCO Using a BAW Resonator. In *Solid-State Circuits Conference, 2008. ISSCC 2008. Digest of Technical Papers. IEEE International*, pages 478–629. IEEE, 2008.

[51] Jiachou Wang, Xiaoyuan Xia, and Xinxin Li. Monolithic integration of pressure plus acceleration composite TPMS sensors with a single-sided micromachining technology. *Microelectromechanical Systems, Journal of*, 21(2):284–293, 2012.

[52] Keping Wang, Jabeom Koo, Richard Ruby, and Brian Otis. A 1.8 mW PLL-free channelized 2.4 GHz ZigBee receiver utilizing fixed-LO temperature-compensated FBAR resonator. In *Solid-State Circuits Conference Digest of Technical Papers (ISSCC), 2014 IEEE International*, pages 372–373. IEEE, 2014.

[53] Gunilla Wingqvist, Ventsislav Yantchev, and Ilia Katardjiev. Mass sensitivity of multilayer thin film resonant BAW sensors. *Sensors and Actuators A: Physical*, 148(1):88–95, 2008.

[54] Jiren Yuan and Christer Svensson. High-speed CMOS circuit technique. *Solid-State Circuits, IEEE Journal of*, 24(1):62–70, 1989.

[55] Fan Zhang, SR Gilbert, F Bi, S Ortiz, B Otis, and RC Ruby. A 2.6 GHz, 25 fs jitter, differential chip scale oscillator that is ¡1 mm^2 in area and 0.25 mm tall. In *Frequency Control Symposium (FCS), 2012 IEEE International*, pages 1–4. IEEE, 2012.

[56] Hao Zhang and Eun Sok Kim. Micromachined acoustic resonant mass sensor. *Microelectromechanical Systems, Journal of*, 14(4):699–706, 2005.

[57] Hao Zhang, Mong S Marma, Sanat Kamal Bahl, Eun Sok Kim, and Charles E McKenna. Sequence specific label-free DNA sensing using film-bulk-acoustic-resonators. *Sensors Journal, IEEE*, 7(12):1587–1588, 2007.

[58] Hao Zhang, Mong S. Marma, S.K. Bahl, Eun-Sok Kim, and Charles E. McKenna. Sequence Specific Label-Free DNA Sensing Using Film-Bulk-Acoustic-Resonators. *Sensors Journal, IEEE*, 7(12):1587–1588, Dec 2007.